Stanford Geothermal Program
Interdisciplinary Research in
Engineering and Earth Sciences
STANFORD UNIVERSITY
Stanford, California

SGP-TR-85

ANALYSIS OF THE STANFORD GEOTHERMAL RESERVOIR MODEL EXPERIMENTS USING THE LBL RESERVOIR SIMULATOR

By

S. T. Lam
A. Hunsbedt
P. Kruger

April, 1985

Financial support was provided through the Stanford Geothermal Program under Department of Energy Contract No. DE-AT03-80SF11459 and by the Department of Civil Engineering, Stanford University.

TABLE OF CONTENTS

		Page
Acknowledgment		iii
Abstract		iv
List of Figures		vii
List of Tables		ix
1. Introduction		1
2. Description of Experimental System		3
2.1	Pressure Vessel	5
2.2	Rock Matrix	7
2.3	Instrumentation	9
2.4	Model Operation and Experimental Results	12
3. Description of LBL Reservoir Simulator		16
3.1	Governing Equations	16
3.2	Solution Method	18
3.3	Discretization of the Flow System	19
4. Experimental System Model		24
4.1	Nodal Representations	25
4.2	Material Properties	29
4.2.1	Water	29
4.2.2	Rock	30
4.2.3	Aluminum	33
4.2.4	Steel and Insulation	33
5. Modeling Results		35
5.1	Summary of Cases Run	35
5.2	Cooldown Experiment Modeling	36
5.3	Production Experiment Modeling	43
5.3.1	Heat Loss Characteristics	44
5.3.2	Inlet Region Modeling	46,
5.3.3	Modeling Results with Constant Rock Thermophysical Properties	48
5.3.4	Rock-center to Water Temperature Difference Comparison	53
5.3.5	Effects of Rock Thermal Conductivity	55
5.3.6	Final Modeling Results	58
5.4	Parametric Evaluation Summary	64

Page

6. Discussion 67

6.1 Possible Sources of Errors 68
6.2 Implications from Modeling Results 71
6.3 Possible Improvements to Experimental System and Simulator . . . 74
6.4 Recommendations for Future Studies 75

7. References 77

Appendices

A. MULKOM Input Listing For Experiment 5-2 79
B. Analysis of the Physical Model Experiment 5-2 Under Simulated Adiabatic Boundary Condition 90

ACKNOWLEDGMENT

The authors acknowledge with much gratitude the assistance of Karsten Pruess of the Lawrence Berkeley Laboratory, California, for his able guidance and personal dedication to the numerical modeling effort in this report. The authors also acknowledge with thanks the assistance of R. J. Munroe of the United States Geological Survey, Menlo Park, and W. M. Somerton of the University of California, Berkeley, in providing the many rock thermal conductivity measurements. This work was carried out under contract with the Department of Energy, whose support is gratefully acknowledged.

ABSTRACT

This report describes the results of an analysis of the data obtained from a series of heat-sweep experiments performed in the Stanford Geothermal Reservoir Model using the Lawrence Berkeley Laboratory reservoir simulator. The physical reservoir model is an experimental system consisting of a pressure vessel which contains a granite rock matrix with production and recharge; capabilities to simulate the heat-sweep process in a hydrothermal reservoir under liquid-phase conditions. Initial analysis of the experimental data was made with the SGP (Stanford Geothermal Program) 1-D Linear Heat Sweep Model designed to estimate potential heat extraction from a fractured hydrothermal reservoir based on estimated reservoir geologic and rock thermal properties. The results of the 1-D model for the physical model data were in reasonable agreement with the observed results. However, the 1-D model could not adequately account for the effect of the steel vessel and associated heat loss to the surroundings.

Arrangements were made with the Lawrence Berkeley Laboratory to test their geothermal reservoir simulator on the physical model data. The objectives were to provide insight into the detailed physical processes occurring in the relatively complex physical system and to provide feedback to LBL on the capability and possible improvements to the LBL reservoir simulator to model a complex physical system.

Results of the efforts were attained in several stages. Initial results using the available physical model input data indicated satisfactory agreement with experimental results. However it was evident that considerable room for improvement was possible. It was also evident that more detailed material property data and external heat loss characteristics were required to improve

the simulation. As a result, the scope of the modeling task was significantly increased. The second stage of cooperation involved performing additional experiments in the physical model to determine system heat loss characteristics. Measurements were made to obtain values of the rock thermal conductivity. The LBL numerical model was refined, and a number of parametric studies involving physical and numerical model parameters were carried out. During the course of the increased study, more than *40* complete and partial computer model runs were made to evaluate the influence of the many system parameters.

Results of the second stage of study indicated that the two parameters having the greatest influence on numerical model results were the system boundary conditions and the material properties, particularly the rock thermal conductivity. The boundary conditions involve specification of the heat loss parameter including the complex steel pressure vessel walls. A good match between simulation and measurements for the heat loss experiment was achieved. The modeling and parameter uncertainties associated with the boundary were substantially resolved. However, adequate modeling of the inlet region could not be achieved for all flow conditions. This was not unexpected since the LBL simulator was not designed to include the necessary natural convection and thermal mixing processes. Consequently, a third stage in the cooperative study was the successful modeling runs using specified rock matrix inlet temperatures based on measurement.

The magnitude of rock thermal conductivity was also shown to have significant influence on the simulated temperature results. Based on initial conductivity measurements at the University of California, Berkeley, and more refined measurements conducted at the U.S. Geological Survey, Menlo Park, an adequate thermal conductivity relationship with temperature was obtained. With this relationship, simulated and measured rock center temperatures were

adequately matched, indicating that the numerical formulation for rock heat transfer under steep temperature gradient conditions is sound. It was also observed that the predicted water and rock axial temperature gradients matched the measured steep temperature gradients near the rock matrix inlet. The combined steep axial and lateral rock temperature gradients in the physical model are extreme conditions that will not usually be found in geothermal reservoirs.

The overall conclusion of this work is that the LBL simulator does an excellent job of predicting the physical processes in the Stanford Geothermal Reservoir Model experiments for extreme thermal gradient conditions and for a system with very complex boundary conditions. The analysis demonstrates the importance of specifying relevant parameters accurately to provide adequate modeling for the important physical processes.

The present work has provided significant understanding of the physical processes and their numerical modeling and additional modeling for these conditions is not recommended. However, it is recommended that serious consideration be given to analyzing the boiling experiments already performed in the physical model. This should provide additional opportunity to test the LBL simulator for two-phase reservoir conditions using physical model parameters established during the current modeling effort.

LIST OF FIGURES

Figure		Page
2-1	Stanford Geothermal Reservoir Model Schematic	4
2-2	Stanford Geothermal Reservoir Model Pressure Vessel	6
2-3	Experimental Rock Matrix Configuration	8
2-4	Lateral and Axial Rock Spacer Details	10
2-5	Experimental Rock Matrix Configuration and Thermocouple Locations	11
2-6	Water-Temperature Thermocouple Holder Details	13
3-1	Idealized Model of a Fractured Porous Medium	21
3-2	Basic Computational Mesh for a Fractured Porous Medium	23
4-1	Basic Computational Mesh of the Experimental System	26
4-2	Conceptual Illustration of the Computational Mesh Used for the Stanford Geothermal Reservoir Model	28
4-3	Effect of Temperature on Rock Thermal Conductivity	32
5-1	Comparison of Measured and Predicted Vessel System Temperatures for Cooldown Experiment 5-4 (constant rock conductivity)	37
5-2	Comparison of Measured and Predicted Vessel System Temperatures for Cooldown Experiment 5-4 (temperature-dependent rock conductivity)	42
5-3	Comparison of Measured and Predicted Water and Rock Temperatures for Heat Extraction Experiment 5-1 (constant rock conductivity)	50
5-4	Comparison of Measured and Predicted Water and Rock Temperatures for Heat Extraction Experiment 5-2 (constant rock conductivity)	51
5-5	Comparison of Measured and Predicted Water and Rock Temperatures for Heat Extraction Experiment 5-3 (constant rock conductivity)	52
5-6	Comparison of Measured and Predicted Rock-center to Water Temperature Differences for Heat Extraction Experiment 5-1 (constant rock conductivity)	54
5-7	Comparison of Measured and Predicted Water and Rock Temperatures for Heat Extraction Experiment 5-2 (temperature-dependent rock conductivity)	57
5-8	Comparison of Measured and Predicted Water Temperature for Heat Extraction Experiment 5-1 (constant rock conductivity)	59

Figure		Page
5–9	Comparison of Measured and Predicted Water and Rock-center Temperatures for Heat Extraction Experiment 5–2 (temperature-dependent rock conductivity)	60
5–10	Comparison of Measured and Predicted Water and Rock-center Temperatures for Heat Extraction Experiment 5–1 (temperature-dependent rock conductivity)	62
5–11	Comparison of Measured and Predicted Water and Rock-center Temperatures for Heat Extraction Experiment 5–3 (temperature-dependent rock conductivity)	63
6–1	Effect of Recharge Rate on Rock-center to Water Temperature Differences for Heat Extraction Experiments	72
B–1	Comparison of Measured and Predicted Water and Rock-center Temperatures for Heat Extraction Experiment 5–2 (temperature-dependent rock conductivity and adiabatic boundary condition) . . .	91

LIST OF TABLES

Table		Page
2-1	Summary of Steel Types Used in the Pressure Vessel	7
2-2	Time-Temperature Data for Stanford Geothermal Reservoir Model Experiment 5-2	15
3-1	Conduction Effects as Water Sweeps One Layer of Rock Blocks	24
5-1	Masses and Average Specific Heats of System Elements	39
5-2	Heat Loss Parameter Calculated from Cooldown Experiment 5-4	39
5-3	Heat Extraction Experimental Data and Parameters	43
5-4	Time-Temperature Data for Stanford Geothermal Reservoir Model Experiment 5-2	45
5-5	MULKOM Modeling Sensitivity Study Summary	66
A-1	MULKOM Input Listing for Experiment 5-2	80
B-1	Changes in Predicted Temperatures for the Adiabatic Boundary Condition Run	92

1. INTRODUCTION

One of the continuous objectives of the Stanford Geothermal Program is the development of methods to evaluate the potential for thermal energy extraction from fractured hydrothermal reservoirs. Successful, long-term commercial development of geothermal resources will depend significantly on the ability to extract sufficient thermal energy from the geothermal rock formation since the quantity of energy stored in the rock is usually much larger than in the hot geothermal fluid. The ability to estimate heat extraction potential from hydrogeologic information and rock thermal properties is especially important in the early reservoir assessment of a prospective field. The effort in the Stanford Geothermal Program has been a combination of physical and mathematical modeling of heat extraction from fractured geothermal reservoirs. Experiments have involved several rock loadings in the Stanford Geothermal Reservoir Model of a rechargeable hydrothermal reservoir with comparative testing of alternate modes of heat and fluid production. The mathematical modeling effort has been concentrated on the development of a simple one-dimensional heat extraction model based on the type of data expected during early development to evaluate the potential for recharge-sweep production of geothermal reservoirs (Iregui et al., 1979; Hunsbedt et al., 1979; Hunsbedt, Lam, and Kruger, 1983).

Calibration of the model was achieved with experimental efforts focused on heat extraction in the physical model using a rock matrix with known geometric shape and the fluid recharge-sweep process. The rock matrix consisted of a combination of granite rock blocks having square and triangular cross-sections to fit inside the circular physical model pressure vessel. Energy extraction experiments were completed for a range of three different recharge-sweep flow rates. Results of these experiments were reported by Hunsbedt et

al. (1982) and by Ramey et al. (1982). The experiments were analyzed using the one-dimensional heat sweep model. Although output of the analysis compared reasonably well with the experimental results from the physical model, it became clear that the mathematical model was not able to account for all phenomena observed in the experimental system. For example, the one-dimensional model could not adequately represent the effect of the pressure vessel steel wall, fluid natural convection in the fractures, and the axial heat conduction on the heat extraction. It became apparent during this effort that more detailed numerical modeling efforts were required to complete the analysis of the experiments and to provide a basis for improvements to the one-dimensional model for reliable assessment of prospective geothermal resources using early reservoir production data.

The improved analysis of the experimental data was achieved with the numerical reservoir simulator developed at the Lawrence Berkeley Laboratory (Pruess and Schroeder, 1980; Pruess and Karasaki, 1982; Pruess and Narasimhan, 1982; Pruess, 1983). The jointly-run analysis not only provided detailed analytical results for the experiments, but it also served as a test of the capabilities of the LBL simulator to analyze results from a physical system. Arrangements were made with Karsten Pruess of LBL to obtain assistance and guidance in the application of the LBL simulator to this problem. Early results of the analysis, reported by Hunsbedt et al. (1982) and Ramey et al. (1982), indicated that considerably more data of the physical system were required, particularly in the areas of system heat loss and rock thermal conductivity. Accordingly, additional experiments were conducted in the physical model to obtain experimental data on the overall heat loss parameter. Measurements were also made of the thermal conductivity of the rock blocks. Initially, this effort was performed by the University of

California, Berkeley and LBL for a rock specimen that had not been thermally stressed in the physical model. Thermal conductivity measurements of both thermally stressed and unstressed specimens were then performed by Robert Munroe of the U.S.Geological Survey, Menlo Park, CA, using his sensitive system.

This report presents the results of the analysis of the physical model data using the LBL reservoir simulator. A summary description of the physical model, experimental measurements, model operation, and experimental results is presented in section 2. A description of the simulator and the numerical model of the physical system is presented in sections 3 and 4, and results of the analysis are presented in section 5. Conclusions and recommendations for further numerical modeling efforts are given in section 6.

2. DESCRIPTION OF EXPERIMENTAL SYSTEM

The energy extraction experiments analyzed in this report were conducted in the Stanford Geothermal Reservoir Model. A diagram of the model, associated piping loops and controls, and sensors is given in Figure 2-1. Detailed descriptions of the experimental system and operation were given by Hunsbedt, Kruger, and London (1975a, 1975b). A description of the particular rock matrix used in these experiments and details of the pressure vessel construction required for the modeling effort are presented in the following. Also, a summary of the experimental results required for comparison to the numerical model results are presented for one of the production experiments.

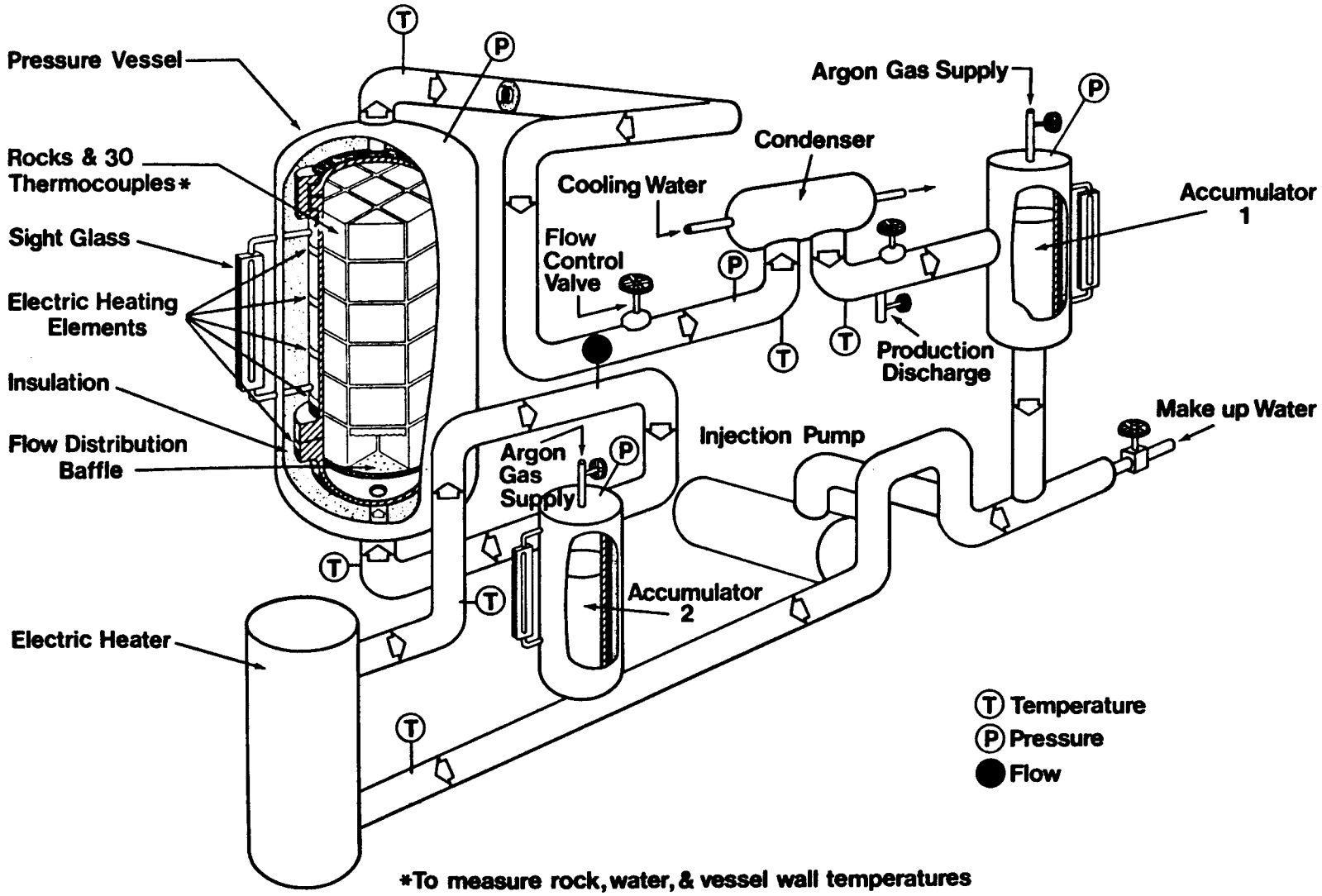

Fig. 2-1: Stanford Geothermal Reservoir Model Schematic

2.1 Pressure Vessel

A carbon steel pressure vessel rated at *800* psia (5.52 MPa) at 500°F (260°C) is used to contain the granite rock matrix. The vessel is approximately 7 feet (213 cm) high by 30 inches (76.2 cm) in diameter overall. A diagram of the vessel is given in Figure 2-2. The inside height available for the rock matrix is 60.75 inches (154.3 cm) from the flow baffle location at the bottom to the flange at the top. The inside diameter of the vessel is 24.5 inches (62.2 cm).

The vessel has a quick opening, hinged closure (Tube-Turns) at the top. The slightly conical head is 1.25 inches (3.18 cm) thick. The bottom of the pressure boundary is formed by an elliptical head bolted (20 1.5-inch (3.8-cm) diameter bolts) to the cylindrical shell through heavy flanges as indicated in Figure 2-2. Sealing of the joint between the two flanges is accomplished by a 1/8-inch (0.3175-cm) thick soft steel, double-jacketed, asbestos-filled gasket. The vessel and elliptical head steel thickness is 0.75 inch (1.91 cm).

A 1-inch (2.54-cm) thick aluminum flow baffle plate is supported by the elliptical head. The plate contains a number of 3/16 inch (0.476 cm) diameter holes to assure that water entering the rock matrix via the inlet pipe at the bottom is distributed uniformly. A number of penetrations are provided in the shell wall for the thermocouples used to measure water and rock temperatures. The pressure vessel is made primarily from medium carbon steels. The particular steel types (ASME classifications) used are summarized in Table 2-1.

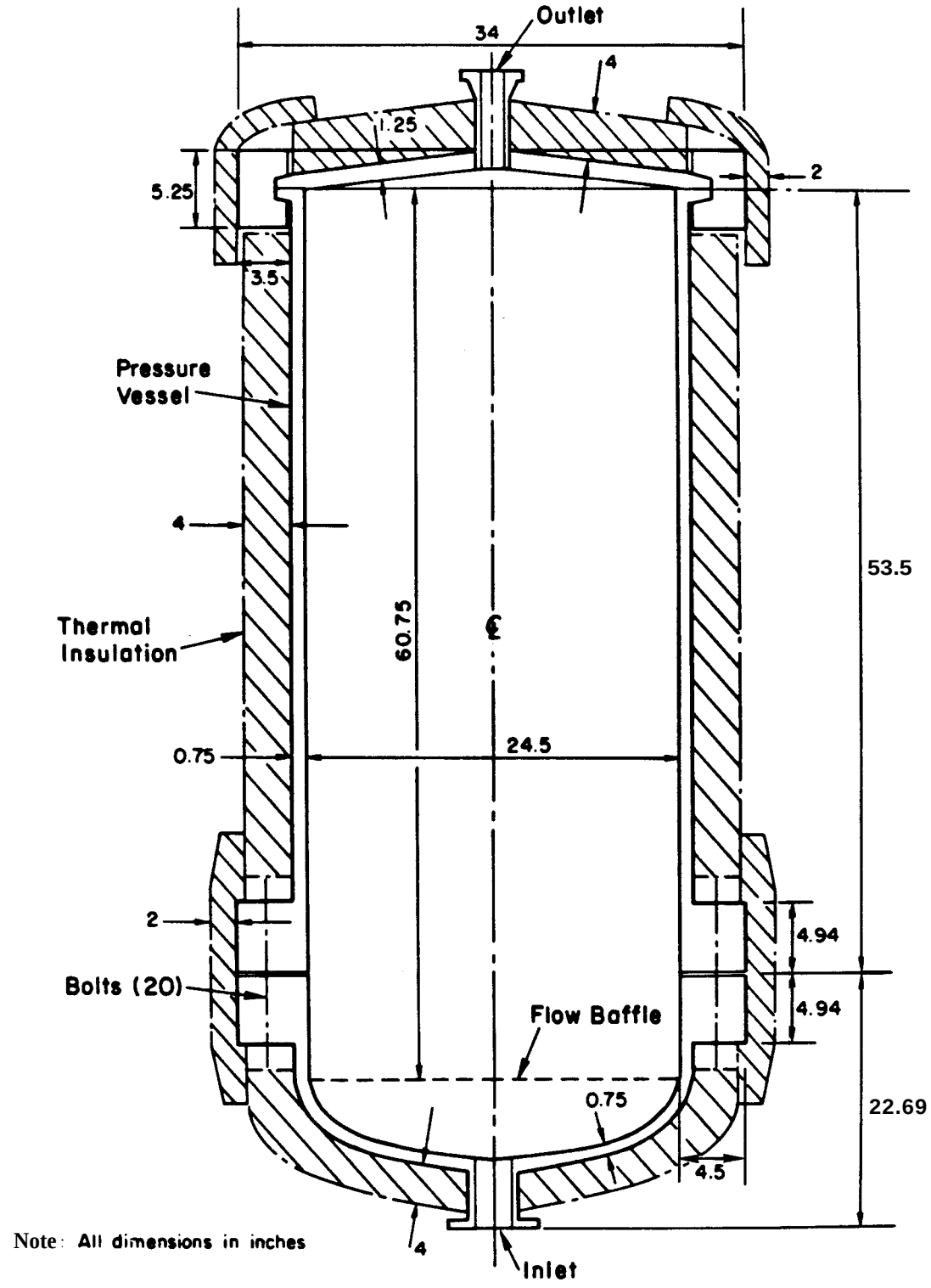

Fig. 2–2: Stanford Geothermal Reservoir Model Pressure Vessel

Table 2–1

SUMMARY OF STEEL TYPES USED IN THE PRESSURE VESSEL

Part	Steel Type
Heads	SA–516 Gr. 70
Shell	SA–516 Gr. 70
Flanges	SA–105 Gr. II
Bolts	SA–193 Gr. B7

The outside of the pressure vessel is insulated to reduce heat losses as indicated in Figure 2–2. The thermal insulation thickness is nominally 4 inches (10.2 cm) for the shell and head, while the removable insulation blankets covering the flanges are nominally 2 inches (5.1 cm) thick. The actual heat loss from the vessel system was determined by cooldown experiments as described in section 5.

2.2 Rock Matrix

The rock matrix used in the present experiments consisted of 30 granite rock blocks having square cross-sections and 24 blocks with triangular cross-sections. The rock block geometries and the spacing between the blocks and the matrix configuration are indicated schematically in Figure 2–3 (with 6 of the 9 blocks total in the cross-section shown). The average height of the blocks is 10.37 inches (26.34 cm) except for the top layer where the average height is 8.0 inches (20.3 cm). The square blocks have 7.51 inch x 7.51 inch (19.08 cm) cross-sections while the sides of the triangular blocks are 7.51 inch x 7.51 inch x 10.62 inch (26.97 cm).

Rock Mosses: Squore ehope 56.5 Ibm
Triangular shope 28.5 Ibm

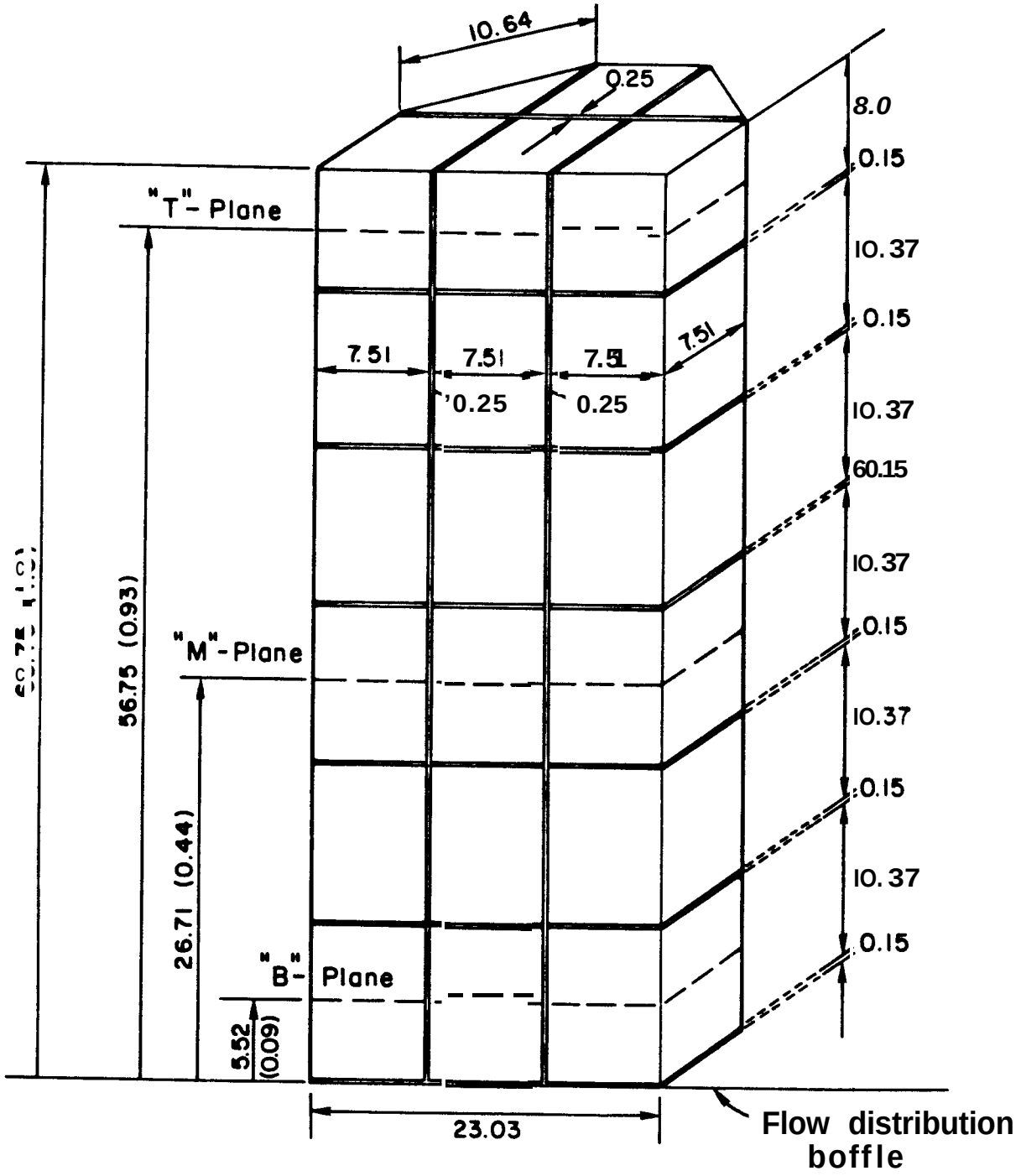

Note: All dimensions in inches

Fig. 2-3: Experimental Rock Matrix Configuration

Axial spacing between individual blocks was *0.15* inch *(0.38* cm) and was determined by the combined thickness of the rock lateral spacer and brass nut heights used for this purpose as indicated in Figure *2-4.* The lateral block spacing was approximately *0.25* inch *(0.64* cm) average and was controlled by lateral rock spacers made from stainless steel sheet metal. Each gap between individual blocks had one spacer centered midway between rock corners and located at the top of each rock layer. The rock matrix cross-sectional configuration was designed to occupy the cylindrical pressure vessel to the maximum extent possible without employing too small blocks. The adapted configurations resulted in considerably larger spaces between the vessel wall and blocks, particularly along the diagonal face of the triangular blocks, relative to the spaces between individual blocks. It was judged that the objectives of the experiments could be met with the selected arrangement.

2.3 Instrumentation

Water and rock temperatures were measured at a number of locations within the vessel as indicated in Figure *2-5.* Thermocouples are located at the inlet to the vessel, at the I-plane just below the flow distribution baffle, at the B-plane half-way up the first rock layer, at the M-plane half-way up the third rock layer, at the T-plane near the top of the rock matrix, and at the vessel outlet. Rock temperatures are also measured at the center of four rock blocks as indicated in Figure *2-5* and at two additional locations in the bottom central rock to obtain temperature gradient data at the locations of severe thermal stress.

The *1/16* inch *(0.0625* cm) stainless steel sheathed thermocouples used to measure the water temperature distribution in each of the three planes within the rock matrix were held in place using the thermocouple holders indicated in

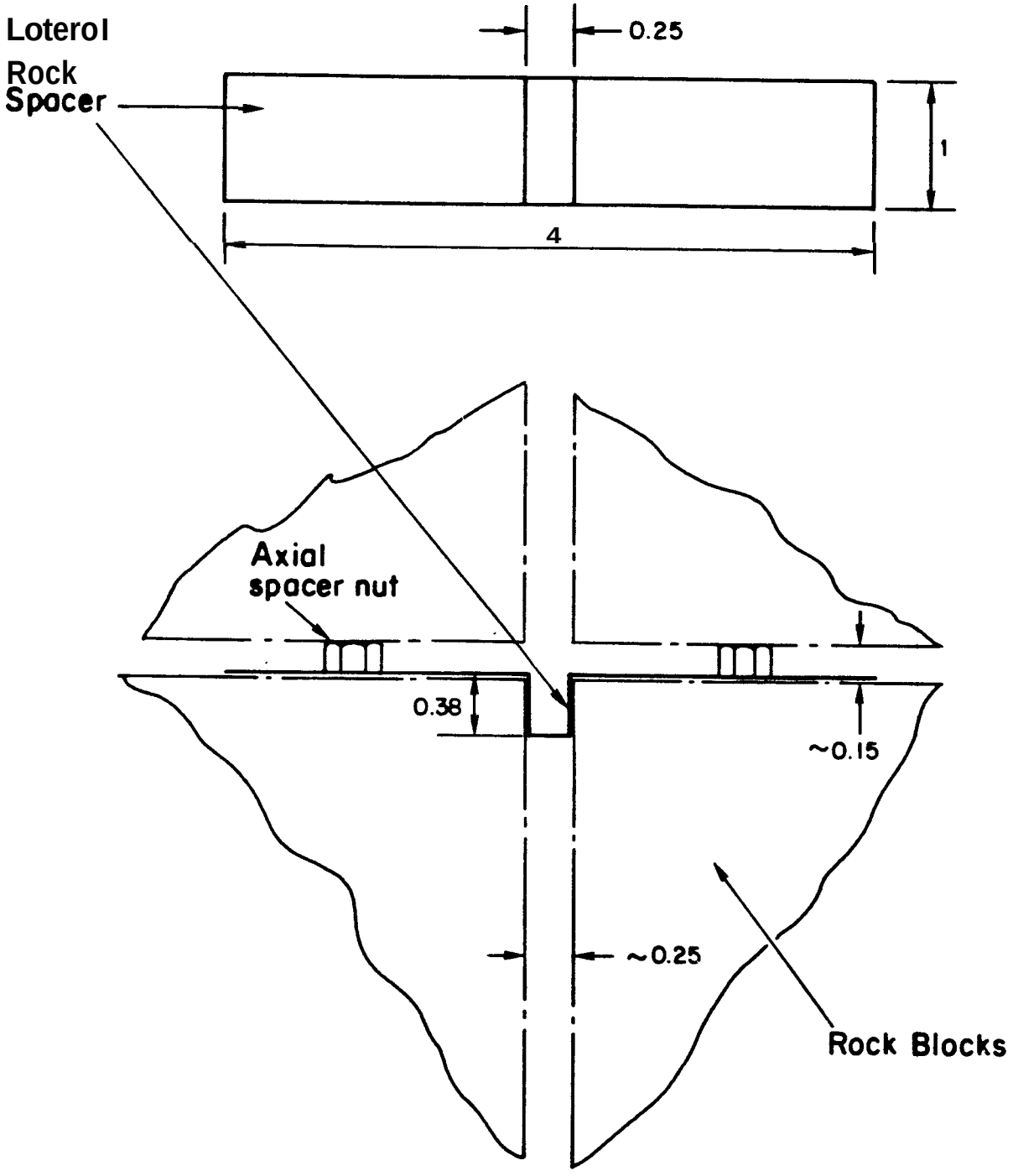

Note: All dimensions in inches

Fig. *2-4:* Lateral and Axial Rock Spacer Details

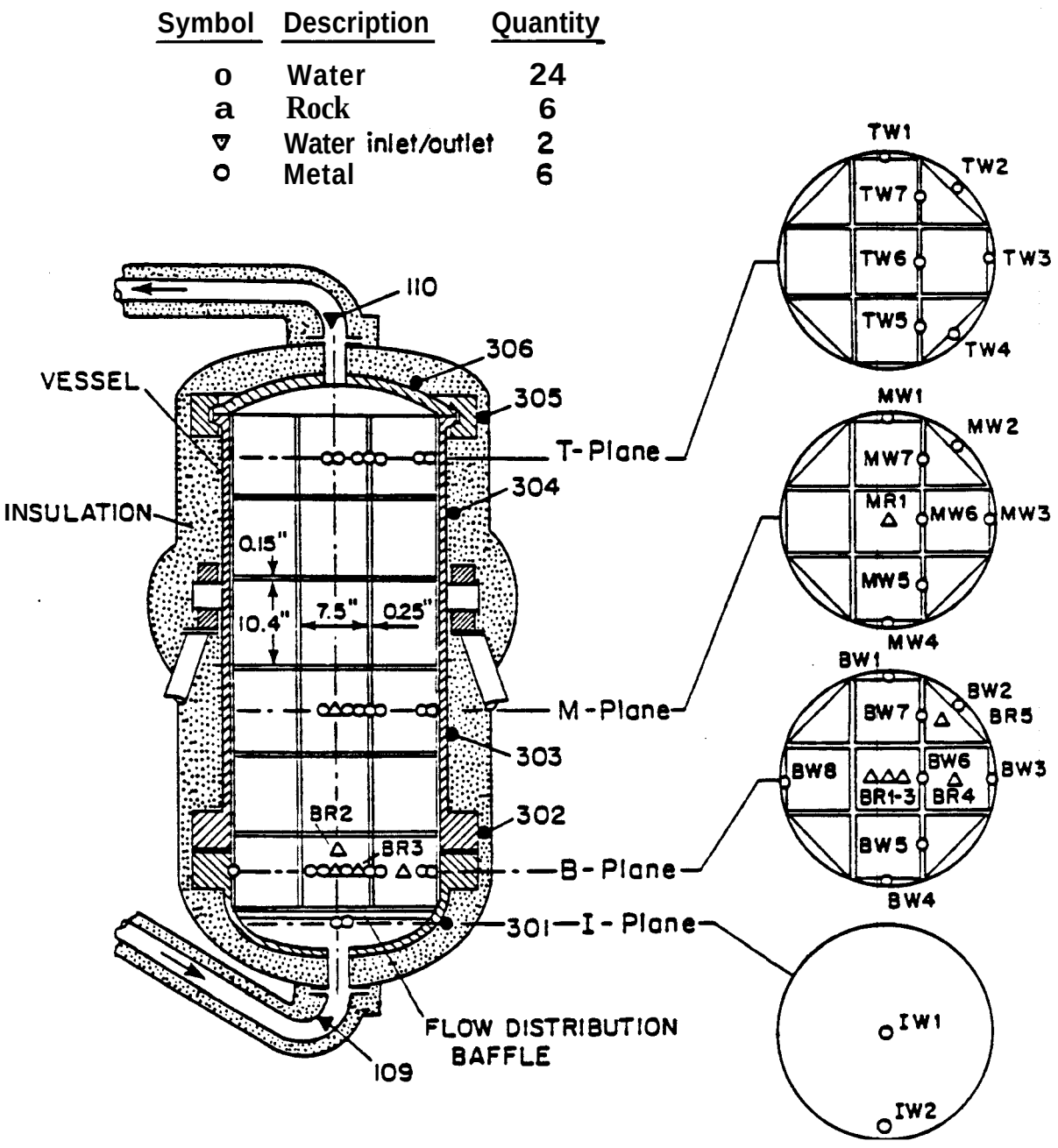

Fig. 2-5: Experimental Rock Matrix Configuration and Thermocouple Locations

Figure 2-6. The holders were held firmly in place on top of two adjacent blocks by the weight of blocks located above (Figure 2-6). The thermocouple stems were held positioned at exactly measured distance (one-half block height ≅ 5 3/16 inch (13.18 cm)) below the block top faces by tightening the set screw provided in the holder. The arrangement in the top layer was similar except that the thermocouple holders were positioned between the top and next to top rock layers and the thermocouples extended upward 4 inches (10.16 cm) from the lower block face.

The thermocouples used to measure rock temperatures were inserted and cemented into 1/8 inch (0.3175 cm) diameter holes drilled in the rock blocks. All thermocouples were routed through several vessel penetrations to the multipoint temperature recorders. The uncertainty in the water temperature measurements was estimated to be ±3°C. The uncertainty in the rock temperature measurement was estimated to be ±6°C.

2.4 Model Operation and Experimental Results

The experimental procedure and operation of the model for the cold water injection heat extraction experiments were explained earlier by Hunsbedt, Kruger, and London (1975a, 1975b). Basically, the system was heated to uniform initial temperature by electric strap heaters located outside of the pressure vessel. The experiment was initiated by starting the injection pump (Figure 2-1) and opening the flow control valve. The injection rate was held constant during the experiment. In the cooldown experiments conducted to determine external heat losses, there was no injection or production.

A total of 4 experiments will be discussed in this report; three of these were heat extraction experiments and one was a cooldown experiment. The three heat extraction experiments were conducted with intermediate, high, and low

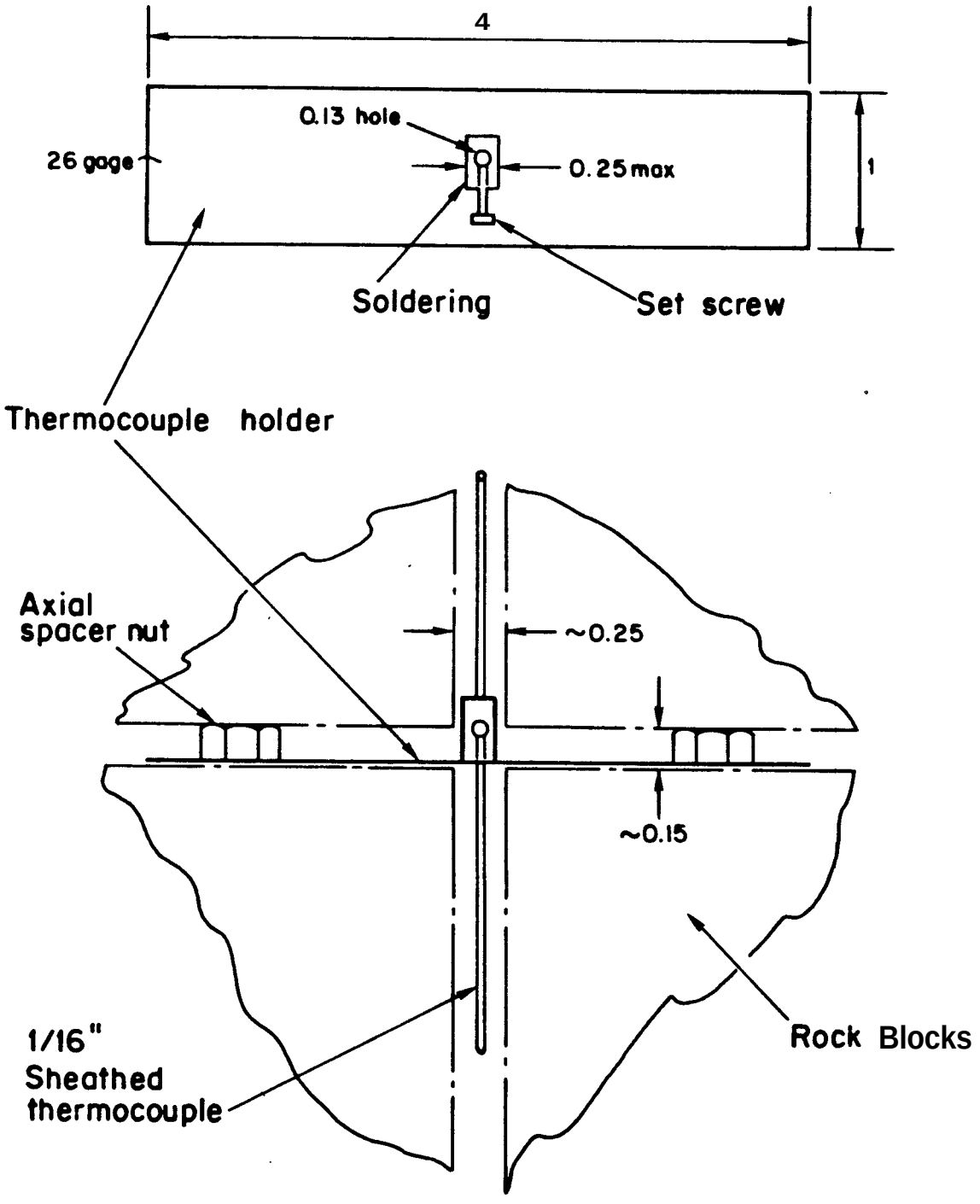

Note: All dimensions in inches

Fig. 2-6: Water-Temperature Thermocouple Holder Details

injection/production rates, respectively. Values of the experimental parameters and results of the time-dependent history using the production run with high injection rate (Experiment 5–2) are summarized in Tables 5–3 and 2–2, respectively. The bars (e.g., $\overline{BW}$) represent the average value of the several water temperature measurements in each plane. The maximum difference between individual water temperature measurements in each plane was generally of the same order as the temperature measurement uncertainty of ±3°C. However, this variance depended on the injection/production rate, being larger for the highest production rate.

Table 2–2

TIME–TEMPERATURE DATA FOR SG RESERVOIR MODEL EXPERIMENT 5–2

Time (hr)	Temperature (°C) at Thermocouple Location											
	109	110	IW1	IW2	$\overline{BW}$	BR1	BR2	BR4	BR5	$\overline{MW}$	MR1	$\overline{TW}$
0.	41	222	207	207	220	218	219	218	220	220	221	221
0.083	28	222	102	124	207	218	219	218	219	220	220	220
0.167	24	221	37	47	146	218	219	218	216	219	219	219
0.250	23	221	24	30	96	218	219	218	199	218	219	219
0.333	23	220	24	25	71	213	216	214	168	213	219	218
0.417	20	219	21	24	57	204	206	204	137	198	219	218
0.500	19	218	20	21	47	188	189	189	109	182	218	217
0.667	18	216	19	18	36	147	150	148	71	149	214	213
0.833	17	212	18	17	30	110	114	110	50	120	206	206
1.000	17	203	17	17	25	81	84	81	37	94	188	189
1.167	17	189	17	16	23	59	64	59	29	74	166	169
1.333	16	172	17	16	21	45	49	45	25	59	142	147
1.500	16	152	17	16	20	36	39	36	22	47	117	125

T_∞ = 24.3°C

3. DESCRIPTION OF LBL RESERVOIR SIMULATOR*

The simulations reported in section 5 were carried out on Lawrence Berkeley Laboratory's CDC-7600 computer, using the multi-purpose simulator "MULKOM". MULKOM was developed at LBL for simulating the flow of multi-component, multiphase fluids and heat in porous or naturally fractured media (Pruess, 1983a). The flow equations solved and the mathematical and numerical methods used in MULKOM are similar to the geothermal reservoir simulator SHAFT79 (Pruess and Schroeder, 1980).

Here we will briefly summarize the equations solved by the simulator, emphasizing the main assumptions and approximations made. Subsequently we shall outline the solution method, and discuss the discretization procedure employed for representing the various components of the Stanford Geothermal Reservoir Model. The nodal representation will be further discussed in section 4.

3.1 Governing Equations

The version of MULKOM used in the present study solves two coupled equations for each volume element of the flow domain, which express a mass balance for water, and a heat balance. In space- and time-discretized form the equations for volume element n are:

$$(\Phi_n^{k+1}\rho_n^{k+1} - \Phi_n^k\rho_n^k) - \frac{\Delta t}{V_n}\{\sum_m F_{nm}^{k+1}A_{nm} + V_n q_n^{k+1}\} = 0 \qquad (3\text{-}1)$$

*This chapter was written by K. Pruess, LBL.

$$(U_n^{k+1} - U_n^k) - \frac{\Delta t}{V_n} \{\sum_m G_{nm}^{k+1} A_{nm} - V_n Q_n^{k+1}\} = 0 \qquad (3\text{-}2)$$

Here n and m label the volume elements (n,m = 1, ..., N), and k is a time step counter. Φ_n^{k+1} is (average) porosity of volume element n at time level t^{k+1}, ρ is density, $\Delta t = t^{k+1} - t^k$ is time step size, V_n is the volume of element n, F_{nm}^{k+1} is the mass flux between elements n and m at time t^{k+1} (defined below), A_{nm} is the interface area between elements n and m, q_n^{k+1} is a mass sink or source term, U_n is the internal energy of volume element n (defined below), G_{nm}^{k+1} is the heat flux between elements n and m at time t^{k+1} (defined below), and Q_n^{k+1} is a heat sink or source term. The sums in equations (3-1) and (3-2) extend over all elements m which share a surface segment with the element n. To assure unconditional stability, we have used a fully implicit formulation, with all fluxes and variable sources evaluated at the new time level, t^{k+1}.

We assume that mass flux is given by Darcy's law

$$F_{nm} = \sum_\beta \left(\frac{k k_\beta}{\mu_\beta}\right)_{nm} (\rho_\beta)_{nm} \left[\frac{P_m - P_n}{d_{nm}} - (\rho_\beta)_{nm} g_{nm}\right] \qquad (3\text{-}3)$$

The summation here extends over the phases present (β = liquid, vapor). k is absolute permeability, k_β is relative permeability to phase β ($0 \leq k_\beta \leq 1$), μ is viscosity, P is pressure, d_{nm} is the nodal distance between elements n and m, and g_{nm} is the normal component of gravitational acceleration between volume elements n and m. The subscripts (nm) indicate that the respective quantities are to be evaluated at the interface between elements n and m. Different weighting procedures can be selected for this, e.g., harmonic weighting, spatial interpolation, or upstream weighting.

The heat flux G_{nm} has a conductive and an advective component:

$$G_{nm} = K_{nm} \frac{T_m - T_n}{d_{nm}} + \sum_{\beta} (h_{\beta})_{nm} (F_{\beta})_{nm} \qquad (3\text{-}4)$$

K_{nm} is thermal conductivity at the interface between elements n and m, T is temperature, and h_{β} is the specific enthalpy of phase β.

Finally, the volumetric internal energy of the rock/fluid mixture is written as

$$U_n = \phi_n \rho_n u_n + (1 - \phi_n) \rho_R C_R T_n \qquad (3\text{-}5)$$

Here ρ_n is the (average) fluid density in element n, u is specific internal energy, ρ_R is rock grain density and C_R is rock specific heat.

The main assumptions made in the above formulation are as follows: (1) Liquid, vapor, and rock are locally in thermodynamic equilibrium (i.e., at the same temperature and pressure at all times). (2) Kinetic energy and inertial force terms are neglected. (3) Capillary pressure and phase adsorption effects are neglected. The above equations need to be complemented with a description of the thermophysical properties of water in its liquid and vapor phases. In MULKOM the steam table equations as given by the International Formulation Committee are used (1967), which represent the needed parameters within experimental accuracy.

3.2 Solution Method

The governing equations as given above are in general highly non-linear, because of non-linear material properties and parameter changes during phase transitions. Furthermore, mass and energy balance equations are strongly

coupled, as in most geothermal applications mass flow is the dominant heat transfer mechanism. The flux terms also strongly couple the balance equations for different volume elements.

Because of these features of the equation system, MULKOM performs a completely simultaneous solution, taking all coupling terms into account. Newton-Raphson iteration is performed to handle the non-linearities. The linear equations arising at each iteration step are solved directly, using Gaussian elimination and sparse storage techniques. The linear algebra is performed with the Harwell subroutine package "MA28", which efficiently handles non-symmetric matrices with random sparsity structure (Duff, 1977). This feature is essential for the particular discretization technique used to represent the Stanford Geothermal Reservoir Model (see below).

3.3 Discretization of the Flow System

In porous media, the variables of thermodynamic state are usually slowly varying functions of position. Under these conditions it is appropriate to discretize the flow domain for purpose of calculation into a number of "sufficiently" small simply-connected volume elements. Conceptually, this approach is straightforward, and it could also be applied to the Stanford Geothermal Reservoir Model. However, this is not very practical, as it would lead to a prohibitively large number of volume elements. The physfcal model contains 30 rectangular and 24 triangular rock blocks, in which three-dimensional heat flow patterns evolve during heat extraction. Discretization needs to be rather fine near the block surfaces, so that the steep temperature gradients at early times of the cold sweep can be adequately represented. A rather coarse discretization would probably require of the order of 100 or more volume elements per rock block, and many additional elements to represent

the water channels between the blocks, and the steel vessel. Clearly approximate methods are needed which permit a drastic reduction of geometric complexity.

The simulations performed in the present study used the method of "multiple interacting continua" ("MINC") Pruess and Narasimhan, 1982). The MINC method was developed as a simplified approach to calculating fluid and heat flow in fractured geothermal reservoirs. Part of the approximations made in this method had already been tested and validated against analytical solutions by C. H. Lai (personal communication, 1982). However, a more complete evaluation of the MINC method by comparison with fluid flow and heat transfer experiments was considered desirable. The present simulation studies were in fact motivated by the hope to accomplish an experimental test of the MINC-method.

Before presenting specific details of the MINC-discretization employed in our simulations, it is appropriate to briefly review the basic ideas behind the methodology. A more complete discussion was given by Pruess and Narasimhan (1982) and Pruess (1983b).

The MINC method is an extension of the familiar double-porosity concept for fractured reservoirs. A fractured reservoir is idealized as consisting of rock blocks separated by void spaces (see Figure 3-1). If such a system of hot rocks is swept by cold water, the water will flow rapidly through the fracture system, while heat will be conducted from the blocks to the water on a much slower time scale. The MINC method makes the approximation that the rock blocks are engulfed by cold water virtually instantaneously, so that heat flow within the blocks will occur in an essentially one-dimensional pattern, namely, outward towards the block faces. With this approximation, it is then possible to discretize the rock blocks into a one-dimensional string of nested

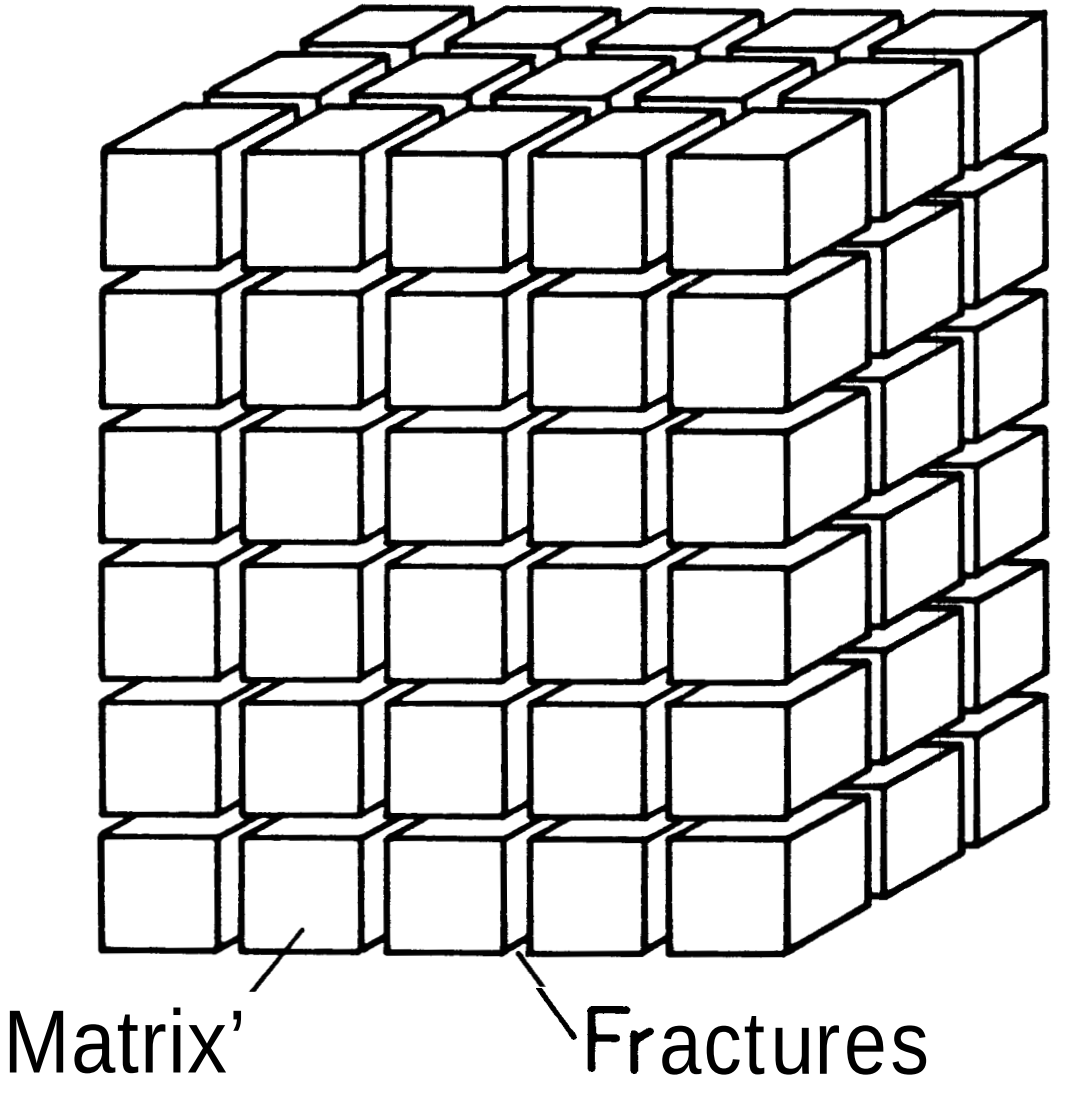

Fig. 3-1: Idealized Model of a Fractured Porous Medium

volume elements, defined on the basis of distance from the block faces. This discretization is shown schematically in Figure 3-2 for a two-dimensional case. Note that this discretization correlates only approximately with the temperature distribution in the blocks, even if the assumption of an instantaneous temperature change at the block faces is valid, because near the block corners conduction effects of several block faces interfere. A more accurate discretization would employ curved interfaces, coinciding with the isotherms for the heat flow problem (e.g., Carslaw and Jaeger, 1959). However, for the problem of heat transfer between rock blocks and surrounding fluid, the detailed temperature distribution within the blocks is irrelevant, as long as the total rates of heat flow across the block faces are accurately predicted. Numerical and analytical studies by C. H. Lai for regularly shaped blocks have shown that the MINC approximation yields total heat flow rates at the block surface which are accurate to within a fraction of a percent (C. H. Lai, personal communication, 1982).

The other important approximation made in the MINC method, namely, that temperature change at the block faces is sudden and instantaneous in comparison to the time needed for significant heat transfer from the blocks to the surrounding water, is not well justified for the conditions of the physical model experiment. This is because of the small scale of the rock blocks and the large void spaces, which cause flow velocities to be rather small. The thermal diffusivity for the granite rocks is approximately $K = 10^{-6}$ m^2/s, so that the diffusion lengths $L_d = \sqrt{Kt_1/2}$ corresponding to the time t_1 it takes to sweep past one layer of rock blocks are significant. Table 3-1 lists diffusion lengths and percentage of volume of the rectangular blocks affected by heat conduction for the times required to sweep one layer in the different experiments.

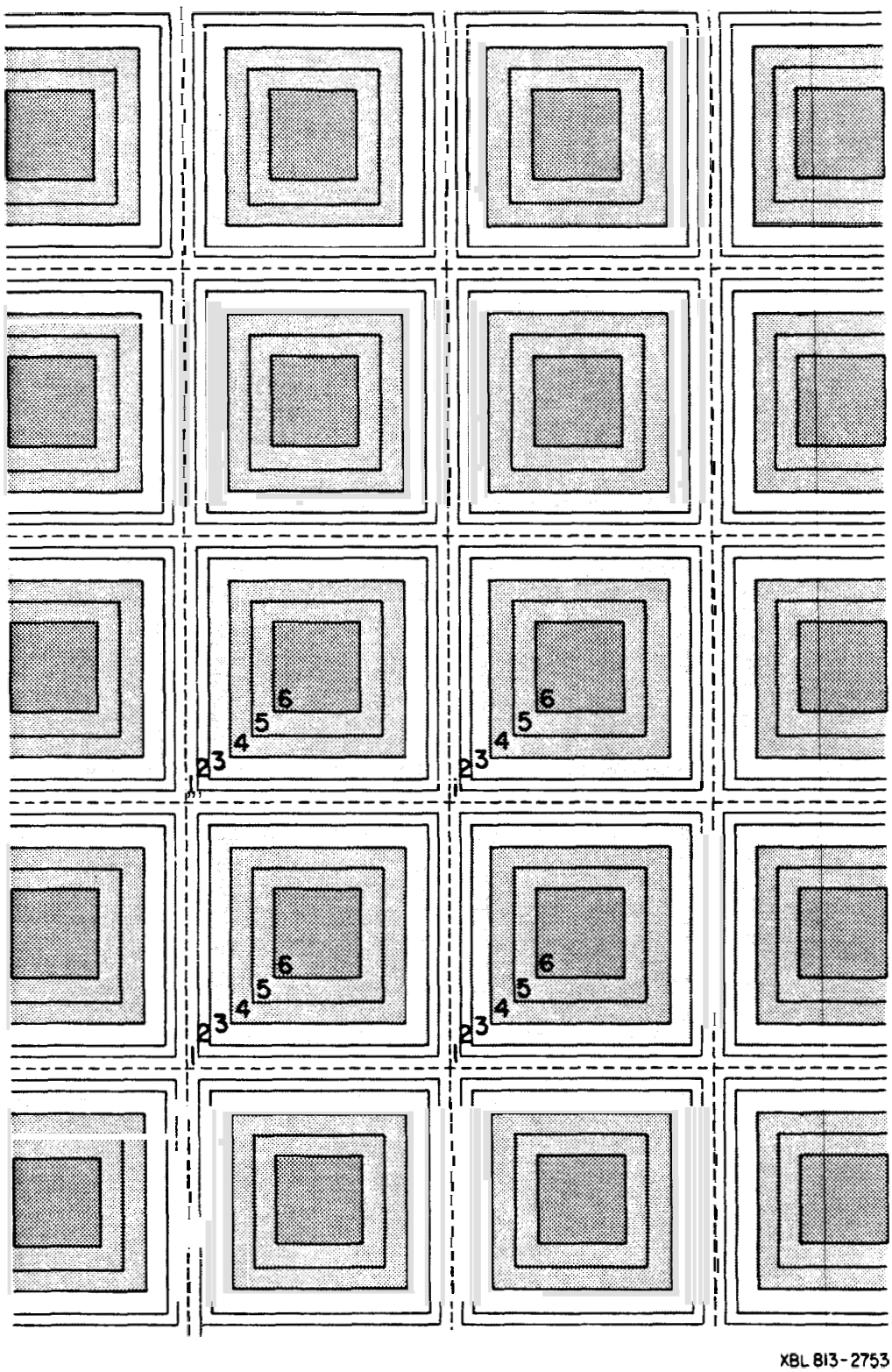

Fig. 3-2: Basic Computational Mesh for a Fractured Porous Medium

Table 3-1

CONDUCTION EFFECTS AS WATER !SWEEPS ONE LAYER OF ROCK BLOCKS

Experimental Run	t_1	L_d	Percentage of Affected Block Volume
1.5 hours	900s	1.5 cm	37.2%
5 hours	3000s	2.7 cm	60.6%
10 hours	6000s	3.9 cm	75.7%

It should be noted that the "instantaneous sweep" assumption is sufficient to justify the discretization made in the MINC method, but it may not be a necessary condition for its validity.

The basic MINC-discretization concept as illustrated in Figure 3-2 can be readily extended to rock blocks of arbitrary shape. In the general case it is convenient to define a "proximity function" PROX(x), which represents the total fraction of rock volume contained within a distance x from the block faces. The proximity function provides all the geometric information which is needed for obtaining a discretization of rock blocks into nested volume elements. Proximity functions for the rectangular and triangular blocks of the physical model, as well as average proximity functions for the individual layers, have been given by Pruess and Karasaki (1982). The computational grids for the simulations of the experiment were obtained from these proximity functions, using a preprocessor computer program "GMINC" (Pruess, 1983b).

4. EXPERIMENTAL SYSTEM MODEL

In this section modeling of the physical model experiments using the LBL reservoir simulator MULKOM is discussed. Descriptions of the major steel

vessel structural components affecting the thermal response of the rock matrix and of material properties used in the numerical modeling are also presented. Results of the model simulation and model/data comparisons are covered in section 5.

4.1 Nodal Representations

MULKOM is a distributed-parameter code capable of simulating complex thermal systems consisting of multiple components, each having different material properties as described in section 3. The code was applied to simulate the thermal response of the experimental system described in section 2. The model includes representations of several major components representing different structural materials and configuations.

In the computer model a one-dimensional column of 30 to 60 disk-shaped elements is used to represent the pressure vessel interior i.e., the rock blocks and water in the fracture spacings, or a total of five to ten elements for each of the six rock block layers. Figure 4-1 shows the mesh used in preliminary modeling with five elements representing each rock block layer. This column is surrounded by two concentric rings of elements which model the steel vessel wall structures and the ambient surroundings as indicated in Figure 4-1.

Each of the 30 to 60 interior elements is further partitioned into a one-dimensional string of 4 to 11 shell elements such that each inside shell is completely enclosed by another shell of the element (see Fig. 3-2). The subpartitioning was based on the MINC method discussed in section 3.

The discretization of the physical system into the computational mesh and the interrelationships between the discretized nodes are illustrated

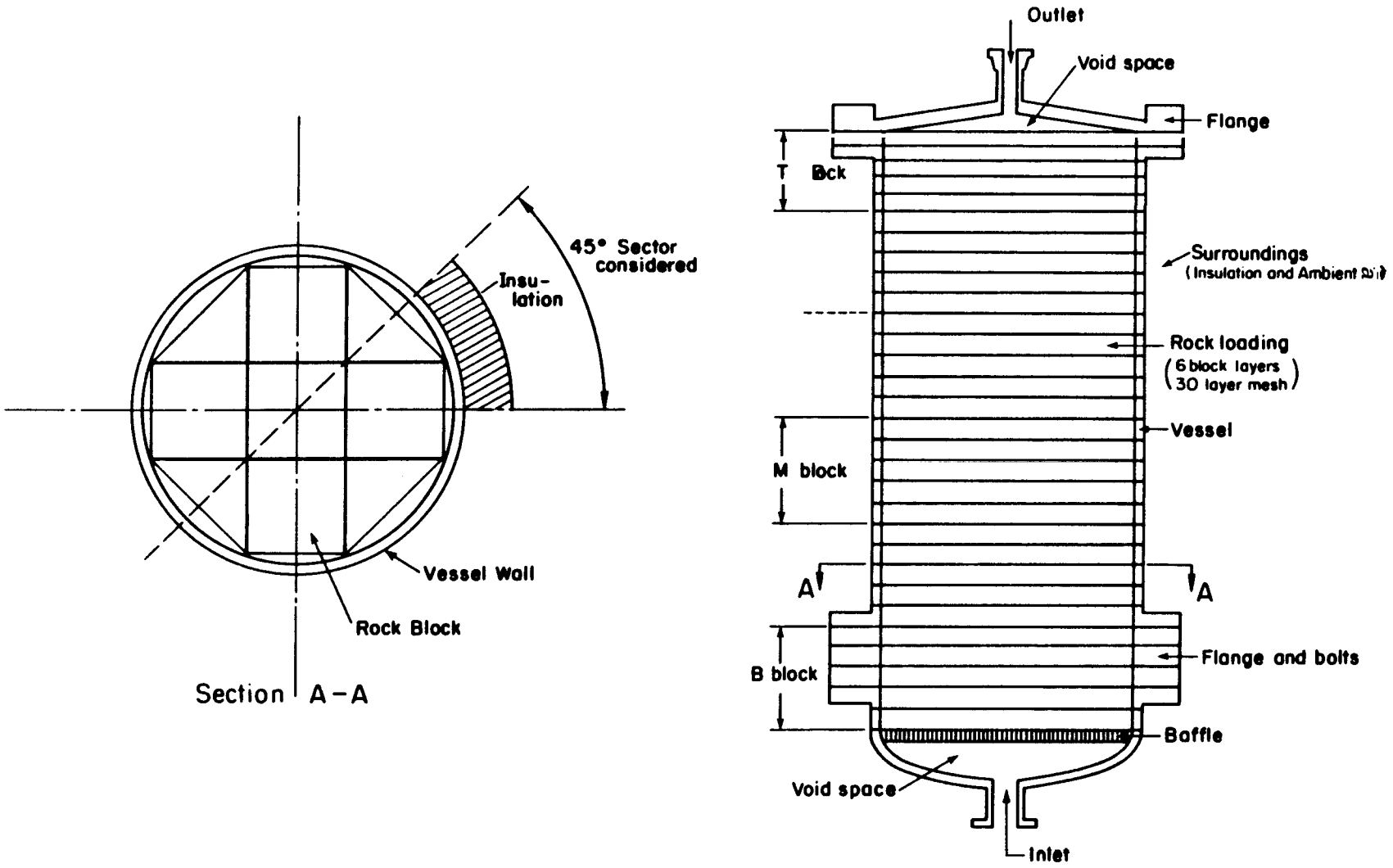

Fig. 4-1: Basic Computational Mesh of the Experimental System

conceptually in Figure 4-2. The water flow path from bottom to top is discretized into 30 to 60 :Layers. Each water volume element is represented by a solid circle in Figure 4-2. The water elements are connected to each other and to elements representing the vessel walls, which in turn are connected among each other, as well as with "infinite" volume elements representing the constant temperature ambient conditions ("surroundings"). Each water element is also connected to the one-dimensional string of nested volume elements in the rock blocks. For the experimental runs, 4 to 11 nested rock volume elements were used.

For proper heat loss modeling, additional irregularly-shaped elements are used for the top and bottom portions of the vessel to represent the two large void space regions, the flow distribution baffle, the inlet and outlet piping and the steel head structures. To optimize the use of computer time, the apparent physical and thermal model symmetry geometry is utilized to reduce the computation mesh to 1/8 of the actual vessel system cross section (or a 45-degree sector) as indicated in Figure 4-1. This simplification is also consistent with the relatively uniform cross-sectional water temperatures observed in the experiments. The entire mesh makes it possible to represent the following processes: (1) water flow up the void channels, (2) heat exchange between steel vessel and water, (3) heat loss from the vessel to the surroundings, (4) heat transfer from the rock blocks to the water, (5) heat conduction within the rock blocks, and (6) axial and radial heat conduction in the vessel steel.

Conductive heat transports between the rock blocks, the water, the steel vessel, and the surrounding air heat sink are assumed to occur between the elements and shell interfaces. Thermal radiation heat loss is negligible compared to convection at the insulation/air interface. The thermal insula-

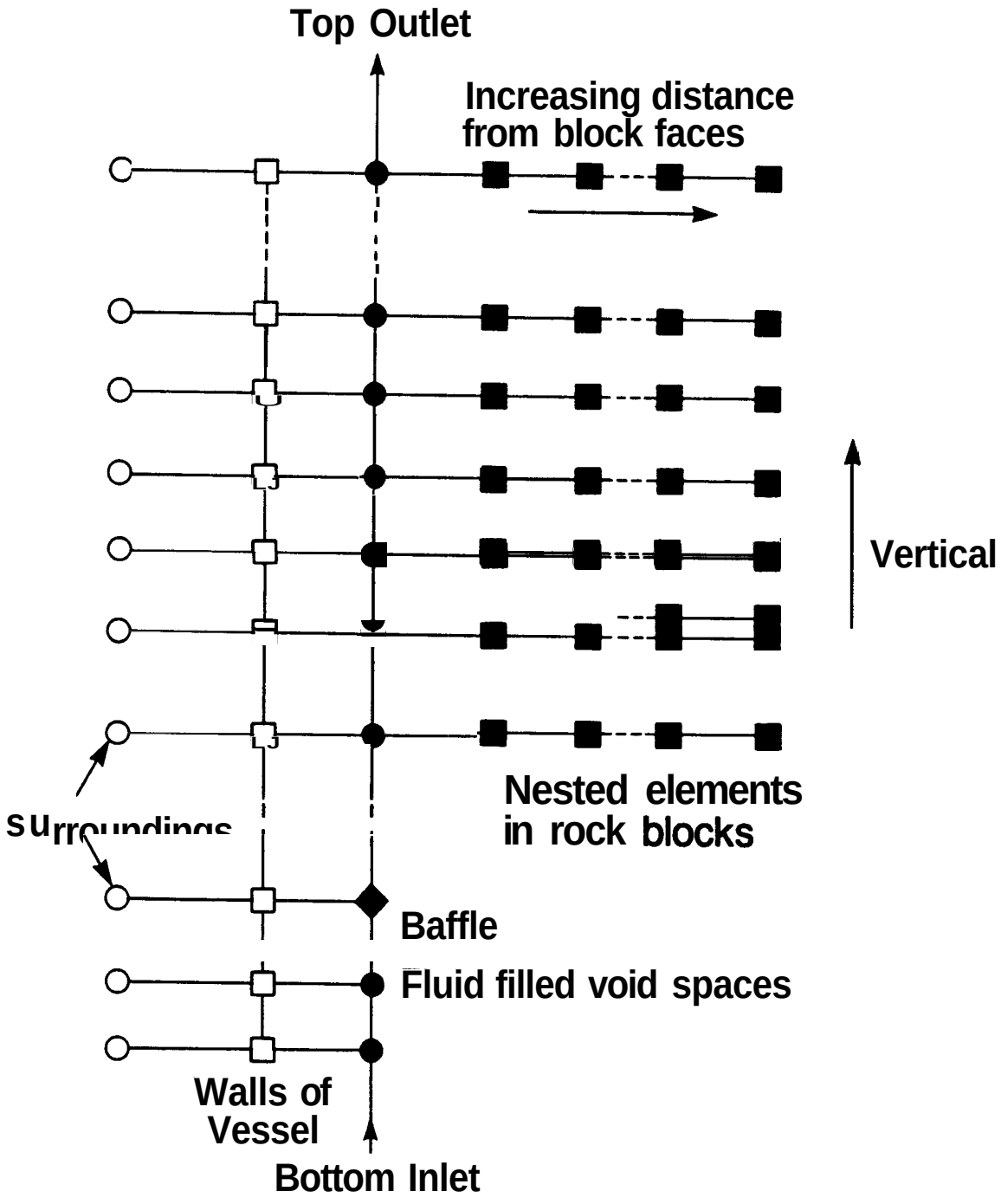

Fig. 4-2: Conceptual Illustration of the Computational Mesh used for the Stanford Geothermal Reservoir Model

tion blanket is modeled as part of the constant temperature surrounding heat sink by using appropriate heat loss parameters empirically determined from cooldown experiments (section 5). This approximate heat loss model reduces the difficulties encountered in modeling the nonuniform and unsteady heat loss across the insulation layer and over its exposed surfaces. Detailed discussion of the heat loss calculation is included in subsections 5.2 and 5.3.

A computer listing of the model elements and shells input data specifying the individual node volume, interface area, characteristic separation distance between two adjacent nodes (or shells), their respective orientation, and their physical properties, together with simulator controlling parameters, is given in Appendix A. The physical properties of the elements are described in subsection 4.2.

4.2 Material Properties

Successful modeling of a physical phenomenon depends significantly on the accuracy of the material property values used in the model. Four materials were used in the present computational model: water, granite rock, steel, and aluminum. The surrounding elements were also assigned artificial material properties to facilitate calculations. Their mass density, bulk porosity, anisotropic permeabilities, thermal conductivity, and specific heat must be specified for the average test temperature or as a function of temperature. Each material is considered separately in the following subsections.

4.2.1 Water

The thermophysical properties of water substance, such as density, viscosity, and enthalpy, are specified as functions of temperature in the form of equations obtained from the International Formulation Committee (1967). The

water properties used in the simulation are believed to be accurate and reliable for the ranges of the test temperature and pressure (see also subsection 3.1). Any variations in the water properties due to chemicals added (to avoid corrosion) or chemicals released from the rock blocks during the experiments are expected to be negligible.

4.2.2 Rock

Granite rock thermophysical properties vary appreciably with temperature and with the source of the rock samples, especially the thermal conductivity. The thermal conductivity of granite decreases with increasing temperature, and its input value was changed several times during the course of this study as a result of thermal conductivity measurement results becoming available. The rock mass density was also updated as measurements were performed. In general, rock properties used in the computer model were typical of granite at 121°C, with mass density = 2675 kg/m3, bulk porosity = 1 percent, thermal conductivity = 2.94 W/mK, and specific heat = 913 J/kgK.

For this modeling study, the granite blocks can be considered impermeable, i.e., anisotropic permeability = 0. Any thermal effects due to filtration of fluid through the blocks should be negligible compared to the rock thermal diffusion, an assumption also validated in experiments conducted by Kuo, Kruger, and Brigham (1975).

The initial value of granite thermal conductivity used was a standard handbook average value of 2.42 W/mK for typical granite. This conductivity value was subsequently updated in the numerical model input following measurement of the conductivity for a spare rock block.

This initial conductivity measurement was performed at the University of California, Berkeley and LBL by Somerton (1982). It used a cylindrical rock

specimen taken from one of the spare triangular granite blocks, and gave a value of 3.29 W/mK at 65.5°C. Based on a study of the variation of granite thermal conductivity with temperature (Somerton, 1982), the measured data point was extrapolated to the average vessel system interior temperature (121°C) during test conditions to obtain the value of 2.94 W/mK subsequently used in the modeling effort. It should be noted that the extrapolation was nonlinear and followed mainly the conductivity-temperature relationship of Rockport granite as presented in Figure 4-3, and that the single sample measurement was assumed to be representative of the entire rock loading. It should also be noted that the family of dashed curves shown in Figure 4-3 is based on thermal conductivity-temperature correlations of most sedimentary sandstones (Anand, Somerton, and Gomaa, 1973). These curves are not directly applicable to the igneous granite rock-fluid system, but are included here, mainly to show the general trend of conductivity-temperature behavior of most rocks.

During the modeling period, more granite thermal conductivity data became available from the United States Geological Survey at Menlo Park. The saturated thermal conductivity for the granite was measured accurately at room temperature (~ 20°C) using a steady-state divided-bar apparatus (Sass, Lachenbruch, Munroe, Green, and Moses, Jr., 1971) for disk-shaped circular rock specimens. The average measured conductivity (3.1 W/mK) from the U.S. Geological Survey experiments and a postulated minimum conductivity of 2 W/mK corresponding to the maximum test temperature of 217°C were used to form a simple linear thermal conductivity correlation. The resulting equation has the form

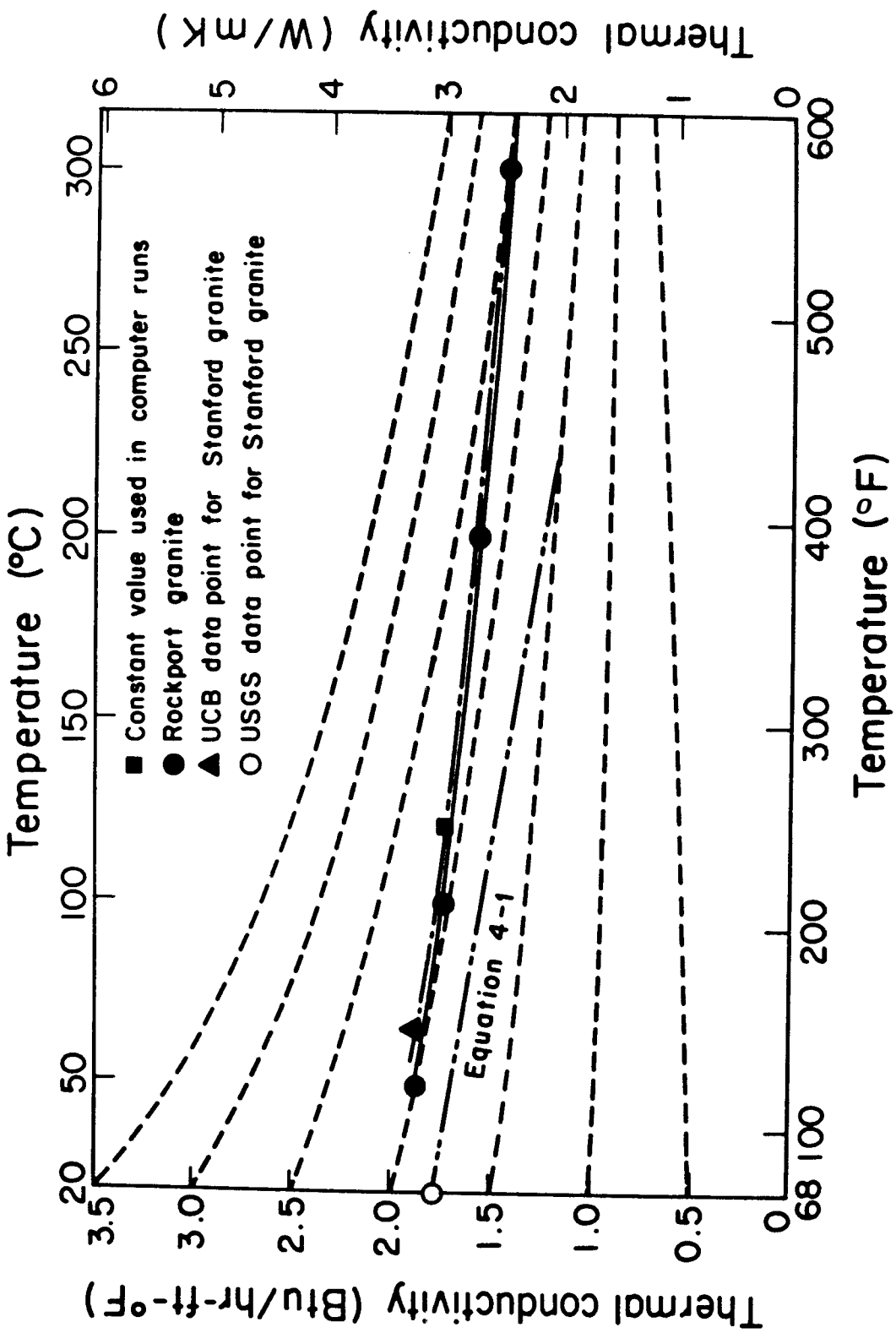

Fig. C-3: Effect of Temperature on Rock Conductivity

$$K = 3.21 - 0.00558\ T \qquad (4\text{-}1)$$

where K is in W/mK and T is in °C. This temperature dependent thermal conductivity correlation was subsequently used in modeling and was expected to eliminate discrepancies in predicted temperatures due to specifying too high or too low constant conductivity value both spatially and temporally.

The permeability of the fracture system was set to a large value of 10^{-11} m^2 (= 10 Darcy; see Appendix A). The exact value of this permeability is unknown, and is believed to be immaterial for the thermal sweep process.

4.2.3 Aluminum

The inlet flow-distribution aluminum baffle, illustrated in Figures 2-1 and 2-5 (see also Ramey, Kruger, Horne, Brigham, and Miller, 1982) is made of commercial aluminum plate. The thermophysical properties were obtained from a standard handbook as follows:

Thermal Conductivity = 201 W/mK

Specific Heat = 862 J/kgK

Density = 2700 kg/m^3

Porosity = 1 percent

Permeability = 0 m^2

These property values were kept constant in the modeling. The flow passage holes in the aluminum baffle, which facilitate uniform inlet sweep velocity and thermal conditions, were not modeled because of expected minor influence on baffle thermal conduction and thermal capacitance.

4.2.4 Steel and Insulation

The pressure vessel containing the rock blocks and the water consists of three major pieces: the top cap, the cylindrical shell and the bottom head as

illustrated in Figure 2-2. Standard handbook values were also used for the thermophysical properties of the two major steel structural components, namely the top and bottom heads and the shell, and the large flanges of the pressure vessel.

The thermal conductivity of the carbon-manganese-silicon steel ($1\% < Mn \leq 1.65\%$, $0.1 < Si \leq 0.6\%$) from which the heads and shell were made (see also Table 2-1) shows a maximum value at a temperature around 250°C, while its specific heat increased monotonically with temperature from 431 J/kgK to 534, J/kgK over a temperature range from 21°C to 260°C (Moen, 1978). An average thermal conductivity of 42.2 W/mK and specific heat of 485.7 J/kgK were used corresponding to the values at 121°C. The mass density of the steel was set at approximately 8138 kg/m^3.

The bottom head is bolted to the vessel shell at the carbon-silicon steel flanges. Average flange thermophysical properties were extracted from the Nuclear Systems Materials Handbook (1980). At the reference temperature of 121°C, the thermal conductivity = 49.97 W/mK, specific heat = 500.8 J/kgK, and mass density = 7690 kg/m3. The porosity and permeability of all steels were taken to be zero.

The steel properties listed above are considered reliable for the type of materials and the test temperature ranges. The properties also agree quite well with data provided by the vessel manufacturer (Kelly, 1983), which specified thermal conductivity of steel at 51.1 W/mK at 121°C.

The steel vessel is wrapped around almost completely by thermal insulation of varying thicknesses to cut heat losses as indicated in Figure 2-2. It was considered impractical in this study to model accurately the complex energy transport processes happening within and around the insulation, hence a separate cooldown test was performed to determine the insulation heat loss for

a typical test temperature differential ($T_{system} - T_{\infty}$) range as will be described in subsection 5.2. The global heat loss parameter obtained was then transformed into an equivalent thermal conductivity value for a constant temperature heat sink representing a combined thermal node for the insulation and the ambient air.

5. MODELING RESULTS

This section presents results of the extensive modeling effort performed for the Stanford Geothermal Reservoir Model experiments. The modeling approach and the various cases run using the LBL simulator along with the parameters varied are summarized in the subsection below. The predicted temperature transients are compared to experimental results for the various cases in the following subsections.

5.1 Summary of Cases Run

Four major experiments were conducted with the physical model, and they were all simulated with the LBL code MULKOM. The experiments included three production tests designed to cover the wide operation range of the experimental apparatus, and one cooldown test for determining the physical model heat loss characteristic.

Several computer runs have been made, starting with a rather coarse mesh and using approximate handbook material properties, to the final runs using a refined mesh configuration and more reliable data and improved chosen input parameters. Although preliminary trial simulations yielded favorable model/data comparisons as presented by Hunsbedt, Lam, Kruger, and Pruess (1982), achieving more accuracy demanded a large number of computer runs, sometimes involving trial and error procedures. However, only representative

cases which provide some insight into either the code and/or the physical system will be presented and discussed in this report.

Results of a sensitivity study will also be discussed in the last subsection summarizing an investigation of major controlling parameters in the rock/water heat transfer process and in the physical model system as a whole. The next three subsections will address the comparison and parametric study results.

5.2 Cooldown Experiment Modeling

The cooldown experiment 5-4 was designed to study the heat loss characteristics of the pressure vessel system for the temperature range expected in the system during the production runs and to establish a data base for quantifying the process.

The test was conducted with the pressure vessel fully loaded and filled with water. During the cooldown test, the vessel isolation valves located in the inlet and outlet lines were closed, thus maintaining a closed system. Temperature and pressure data were recorded continuously when the system was cooling down from its initial uniform temperature of 242°C. The cooldown process occurred mainly through thermal conduction across the vessel walls and the insulation blanket surfaces and in protruding steel structures, and by natural convection from insulation surfaces and any exposed steel vessel structural components.

This heat loss process was very slow as is evident in Figure 5-1. It took over one hundred hours for the vessel and its interior to cool to near room temperature. Figure 5-1 shows the recorded system interior temperature which is equal to the average for the rock-center, steel vessel, and water temperatures. The maximum variation in observed water and rock temperatures

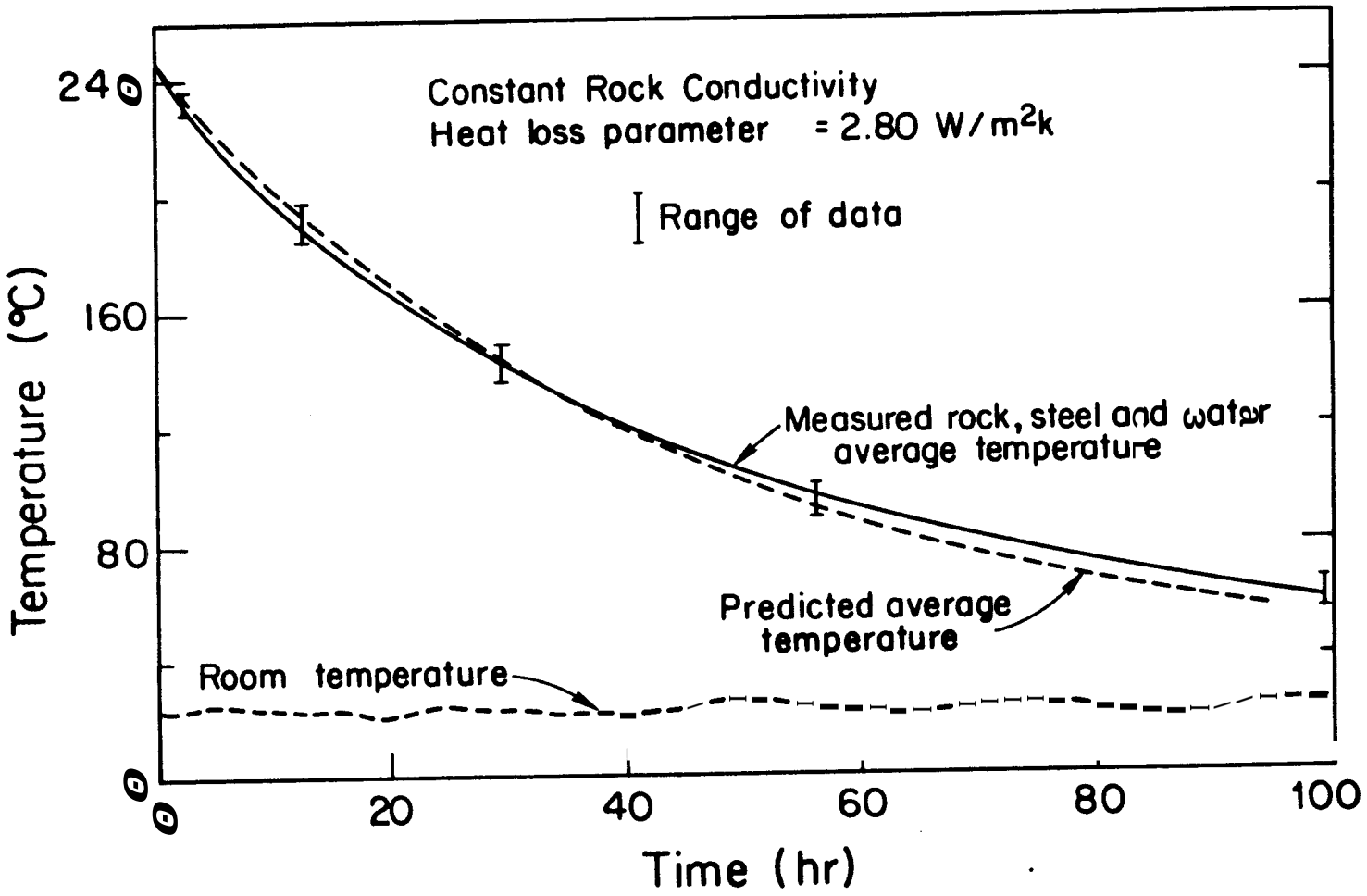

Fig 5-1: Comparison of Measured and Predicted Vessel System Temperatures for Cooldown Experiment 5-4 | constant rock conductivity)

was about ±5°C, which indicates that the system can be treated thermally as a lumped mass and a simple thermal model can be developed to simulate its transients.

In developing the lumped parameter model, it is desirable to divide the physical model system into three major mass elements, each having a different average specific heat. These three major mass elements consist of rock, steel, and water. The combined mass has an effective total surface area through which all energy losses (convection and conduction) is accounted for in a manner similar to the conventional definition used in convection heat transfer. The masses and average thermal capacities of the three elements are given in Table **5-1** (Hunsbedt, Kruger,,and London, 1975).

An energy balance for the system in a quasi-steady state results in the following equation:

$$(\nu A)_{syst}\ (T_{syst} - T_{\infty}) \stackrel{\approx}{=} - \sum_{i} M_i Cp_i \left(\frac{\Delta T}{\Delta \tau}\right)_{syst} \cdot \left(\frac{1}{3600}\right) \qquad (5\text{-}1)$$

where

ν_{syst} = system heat loss parameter, W/m^2K

A_{syst} = effective system heat transfer surface area, m^2

T_{syst} = system average temperature, °C

T_{∞} = ambient temperature, °C

$A\tau$ = time interval, hr

M_i = mass of component i, kg

Cp_i = specific heat of component i, J/kgK

The left hand side of the equation represents overall system thermal energy loss which is equated to the decrease in system total thermal capacitance.

Evaluation of temperature/time gradients at different times in Figure **5-1** provides the values on the left hand side of Equation 5–1 at various

$\Delta T = (T_{syst} - T_\infty)$, the heat loss parameters calculated with A_{syst} = 4.09 m2 are summarized in Table 5-2.

Table 5-1

MASSES AND AVERAGE SPECIFIC HEATS OF SYSTEM ELEMENTS

Element Description	Mass (kg)	Specific Heat J/kgK
Rock	1065	913
Steel	1792	500
Water	135.4	4233

Table 5-2

HEAT LOSS PARAMETER CALCULATED FROM COOLDOWN EXPERIMENT 5-4

τ (hr)	$\frac{\Delta T}{\Delta t}$ (°C/hr)	ΔT (°C)	ν (W/m^2K)
0	5.46	219	3.78
10	3.72	173	3.26
20	2.89	146	3.01
30	2.23	117	2.89
40	1.76	98	2.72
50	1.41	79	2.70
90	0.67	46	2.19
100	0.50	35	2.16

An alternative approach to estimate the ν value is by integrating the differential form of Equation (5-1) assuming T_∞ and $M_i Cp_i$ constant. This leads to the ν value equation as

$$\nu = -\left(\frac{\ln \frac{\Delta T}{\Delta T}}{\bar{A}_{syst}}\right) \left[\sum_i M_i Cp_i\right] \qquad (5\text{-}2)$$

Equation (5-2) gives an average ν of 3.33 W/m^2K when 146°C < AT < 219°C, and 2.42 W/m^2K when 35" < AT < 58°C. These numbers are in good agreement with those given in Table 5-2.

Table 5-2 suggests that ν decreases with decreasing AT and this ΔT dependence weakens with decreasing AT, and that a high-order polynomial fit may be used to correlate the $\nu/\Delta T$ data. However, it is important to realize that the cooldown experiment did not exactly duplicate the heat loss situations of the production experiments. For example, a substantial temperature difference existed between the rock matrix and the sweeping water in the production runs. This rock-to-water AT was absent in the cooldown run. In the production runs, the steel structures served as possible heat sources for both sweeping water and energy loss to the surrounding, while in the cooldown run, the entire vessel and interior became a heat source at near equilibrium temperature for energy loss to the surrounding.

Furthermore, the cold water sweep process could produce an advancing thermal front rising upwards in the vessel system. This front generated axial temperature non-uniformity in the vessel structures in addition to the temperature non-uniformity due to different axial insulation blanket thicknesses. It is apparent that the absence of such front-induced temperature non-uniformity in the cooldown test could lead to quite different heat loss distribution over the vessel system exterior boundary.

The limiting values of v given in Table 5-2 are 3.8 W/m2K at high system AT and 2.2 W/m2K for low system AT. The three production experiments 5-1, 5-2, and 5-3 have AT ranges from 194 to 28°C, 214 to 32°C, and 200 to 38°C, respectively. These ΔT's are basically bounded by the cooldown data. Applying the v values derived for a given AT should overpredict the heat loss quantity in the production runs slightly. However, for a constant median v value used in the cooldown simulation, the heat loss amount will be underpredicted initially and overpredicted at the later phase.

The LBL simulator was applied to the cooldown run using the heat loss parameters derived to evaluate which average value would result in the best match. Figure 5-1 shows the predicted and measured average system temperatures and the corresponding room temperature. The numerical model used consisted of 30 element layers with 4 shells per layer, rock thermal conductivity was set at 2.94 W/m^2K, the surrounding air temperature T_∞ = 23°C, and the conduction path length for each surrounding element over the vessel surface was constant. This model gave the best match at a constant heat loss parameter value equal to 2.8 W/m^2K which corresponds to a AT of 107°C.

Equally good agreement was obtained with a second MULKOM model having a linearly varying temperature dependent rock thermal conductivity as shown in Figure 5-2. This was expected since rock conductivity should not dominate in this near thermal equilibrium system experiment. In this model, 60 element layers were used with 4 to 11 shells per layer. The test data again indicate that v should be around 2.8 W/m^2K for this mesh configuration. In general, Figures 5-1 and 5-2 suggest that the predicted temperatures are not very sensitive to small variations in the heat loss parameter.

The cooldown test conducted established a data base for estimating the effects of heat loss from the physical model system. This heat loss accounted for a significant fraction of the physical system initial thermal capacitance.

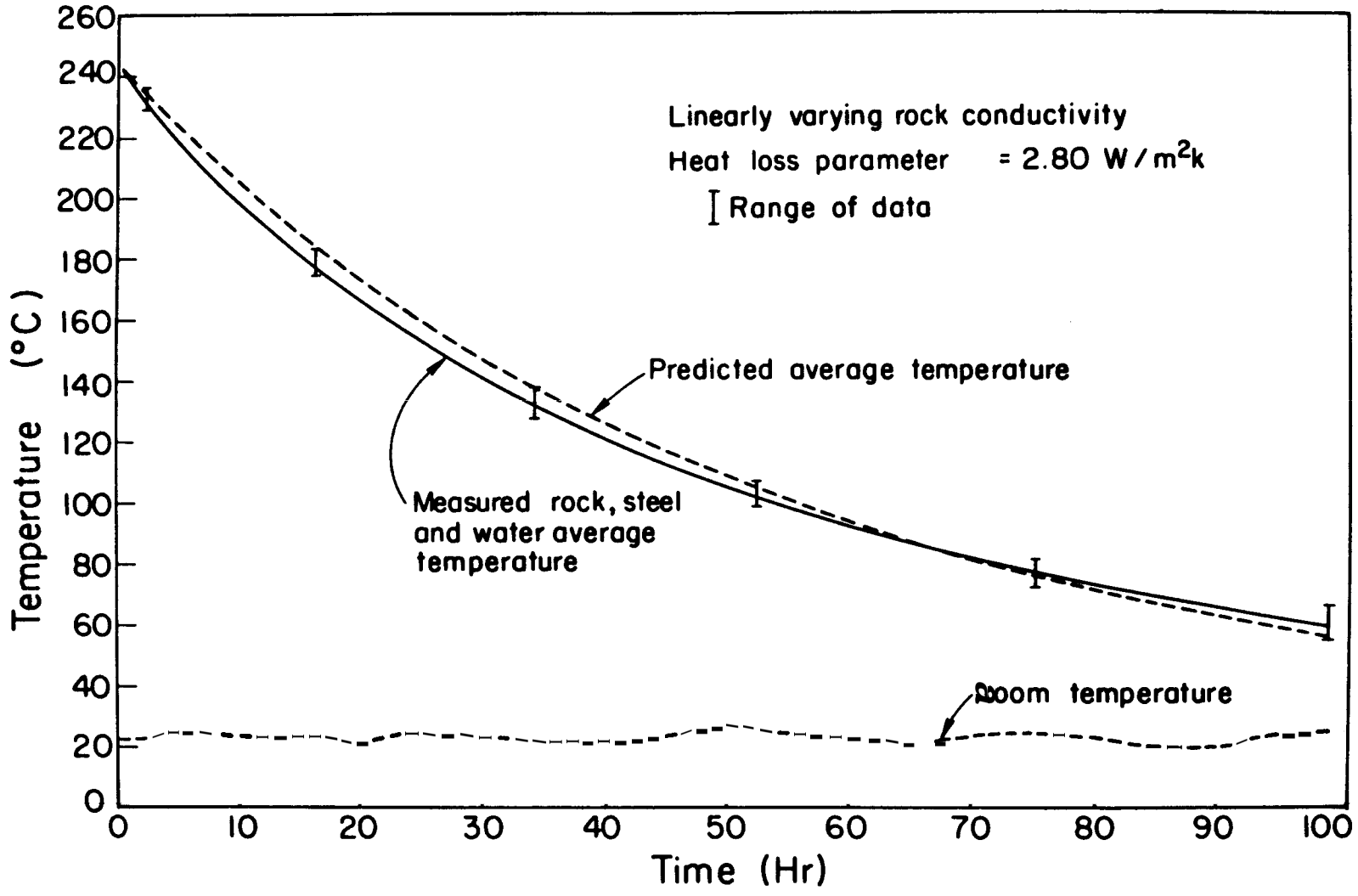

Fig. 5-2: Comparison of Measured and Predicted Vessel System Temperatures for Cooldown Experiment 5-4 (temperature-dependent rock conductivity)

5.3 Production Experiment Modeling

In rock heat extraction modeling, one of the most important parameters is the "number of heat transfer units" which represents the ratio of the time the recharge water is in contact with the rock to the average thermal response time of the rock blocks. The three heat extraction experiments with various fluid recharge rates and production times designed to cover a wide range of the number of heat transfer units parameter are discussed further here.

Experiment 5-2 is noted from Table 5-3 to have a flowrate about three times that of experiment 5-1, while the flow rate for experiment 5-3 was about one-half that of experiment 5-1. Table 5-3 lists the parameters for all experiments. Detailed evaluation of rock heat transfer processes, numerical modeling approach, and simulation results will be presented in the following subsections.

Table 5-3

EXPERIMENTAL DATA AND PARAMETERS

	Heat Extraction Experiment		
	5-1	5-2	5-3
Average Reservoir Pressure (MPa)	3.8	3.8	3.8
Initial Reservoir Temperature (°C)	239	220	220
Final Water Temperature at Top (°C)	156	125	141
Final Water Temperature at Bottom (°C)	19	20	28
Injection Water Temperature ("C)	15	15.6	18.3
Water Injection Rate (kg/hr)	68	227	31.4
Production Time (hr)	5	1.5	10.5
N_{tu} Parameter (dimensionless)	7	2	15

5.3.1 Heat Loss Characteristics

Mathematical modeling of the production experiments 5-1, 5-2, and 5-3 makes use of the heat loss data derived from the cooldown experiment 5-4. This surface heat loss term is considered relatively large compared to the amount of energy extracted from the rock matrix, especially for the long residence-time experiment, e.g, experiment 5-3.

In the 1.5-hr experiment, the steel vessel remained at a relatively high temperature throughout the production period, thus the average heat loss rate to the ambient was the highest because vessel surface heat flux primarily depends on the steel wall temperature, but the high heat flux was over a shorter time period. The 10.5-hr test: allowed more time for the rock, water, and steel components to approach near equilibrium temperature throughout the transients, and the average vessel temperature above that of the surrounding air was not as high as the fast sweep test. In this experiment, the vessel surface heat flux, in general, was lower although the total heat loss over the production period represented a much larger fraction of the thermal energy stored compared to the 1.5-hr experiment.

Table 5-4 shows the steel vessel temperature transients for experiment 5-2. Comparing to temperatures for the same experiment listed in Table **2-2**, it is apparent that the steel vessel had slightly lower temperatures than the adjacent water, especially early in the transient (e.g., TC#301 vs $\overline{BW}$), indicating that the rate of heat loss from the lower vessel walls was very high initially. Later in the transient, the vessel was at a slightly higher temperature near the bottom region. This temperature recovery is probably due to the high steel conductivity which allowed substantial axial conduction in the vessel walls. A similar trend was also observed in experiment 5-1.

Table 5-4

TIME-TEMPERATURE DATA FOR STANFORD GEOTHERMAL, RESERVOIR MODEL EXPERIMENT 5-2

	Thermocouple Number(1)				
Time (hr)	301	302	303	304	305
0.	209(2)	222	224	222	212
0.083	188	221	222	222	212
0.167	107	220	221	221	212
0.250	72	216	218	221	212
0.333	56	203	207	220	212
0.417	47	184	189	219	212
0.500	42	164	168	218	212
0.667	37	127	132	209	210
0.833	31	98	102	190	208
1.000	26	76	78	166	206
1.167	24	60	61	139	200
1.333	23	49	49	116	191
1.500	22	39	39	94	179

(1) Thermocouple labels refer to the physical model schematic in Figure 2-5. Thermocouple #306 did not function properly during the tests and so its measurements are not reported.
(2) Temperatures in °C

At the M-plane, the steel temperature was higher than that of the water at the same elevation until approximately 0.17 hr when the cold water front should have reached the M-plane elevation (see temperatures of TC#303 vs $\overline{MW}$). The faster temperature drop experienced by the steel wall compared to that of the water after this time can be explained by downward axial heat conduction in the steel. The pressure vessel acted as an energy source to the ambient

air and water throughout the test, and it also acted as an axial heat conduction path.

In the test modeling, the complex spatial and temporal varying temperature boundary conditions were handled by using the heat loss parameter v derived from experiment *5-4.* Constant average values of the ν parameterg were applied in the two cooldown simulations (subsection *5.2)* and in the modeling of all three production runs because of the approximate and global nature of the parameter. This approach can introduce mismatches in the actual, heat loss pattern; however, in the absence of more specific experimental data, this approach should greatly reduce the number of parameters needed to be varied, and still give a reasonable overall approximate heat loss boundary condition. A more refined determination of heat loss would require a more densely installed array of temperature sensors (thermocouples) in the vicinity of the system/surrounding interface, and a more detailed data analysis.

5.3.2 Inlet Region Modeling

In all three experiments, cold water at room temperature was injected continuously at a constant rate into the pressure vessel through the inlet line at the bottom. After hot water initially in the hot inlet line (near TC#109) entered the vessel, subsequent recharge cold water was slightly heated through convection by the hot piping and entrance steel structures so that the inlet region (TC#109) water temperature experienced a temperature history which declined almost exponentially with time to the cold tap water temperature. Downstream of this temperature node, a complex process of mixing of hot and cold water, and of thermal conduction/convection from the steel/aluminum walls took place in the inlet plenum region. Two different modeling approaches for the fluid entry temperature will be presented and discussed in more detail in this subsection.

In the first approach, the measured water temperature at the inlet valve location (T/C#109) was specified and appropriate modeling of the thermal mixing and convection included in the model for the inlet plenum region. In the second approach, the measured flow distribution baffle (IW-plane) water temperature was specified as the recharge temperature boundary condition, disregarding the very complicated thermal and mixing processes taking place in the inlet plenum region.

Figures 5-3 through 5-5 and Figure 5-8 show the measured inlet valve region water temperatures (T/C#109) and the measured flow baffle location water temperatures (IW-plane) for the three production runs. Also shown are the corresponding predicted temperatures from the numerical model. It is observed that direct code input of the measured recharge temperature boundary conditions (at TC#109 location) did not result in good temperature predictions at the TW-plane in all cases. The accurate IW-plane prediction for experiment 5-2 as illustrated in Figure 5-4 represents an exception. The good match in this case is probably due to correct modeling of the smaller amount of heat loss from the vessel bottom plenum associated with the fast sweep. These temperature prediction discrepancies at the IW-plane are caused by: (1) the incomplete understanding and modeling of the various energy transport modes taking place in the inlet plenum region and (2) the inexact geometry and material property input data.

A correct IW-plane temperature prediction is necessary for attaining good downstream predictions. In the second approach, the previous problem was eliminated by specifying the IW-plane measured enthalpy history as a direct code input boundary condition. This approach is justified because the portiod of the vessel system beneath the bottom rock block layer plays only a minor role in studying physical model reservoir performance. In addition, the LBL

simulator was not designed to analyze this rather complex inlet plenum problem.

Computed temperatures for experiment 5-2 using this approach is shown in Figure 5-9. It is seen that the resulting IW-plane temperatures become higher than their corresponding input values due to thermal interactions between the IW-plane temperature nodes with neighbor nodes. Consequently, additional runs were made by inputting artificially specified IW-plane enthalpy history obtained through systematic trial and error and engineering judgment. Predictions for experiments 5-1 and 5-3 with this input are presented in Figures 5-10 and 5-11, respectively. Very good matches were obtained at both IW- and B-planes, thus resolving the reservoir inlet region modeling problem,

5.3.3 Modeling Results With Constant Rock Thermophysical Properties

The three experiments were simulated using MULKOM input parameters similar to those used in the cooldown experiment simulation, except that a total of 60-element-layer computation mesh was used for all runs. The value of the heat loss parameter V applied were 2.8, 3.8, and 2.2 W/m^2K, respectively for experiments 5-1, 5-2, and 5-3. The maximum time steps used in each case were 125, 30, and 250 sec, respectively.

These input parameters resulted from an extensive parametric study to be discussed in subsection 5.4. Preliminary computations indicated that the heat loss parameter V of 2.8 W/m^2K used for the cooldown simulation was more appropriate for heat loss calculation in experiment 5-1. Experiment 5-2, having higher heat loss rate, was assigned the maximum V value of 3.8 W/m^2K; similarly experiment 5-3 was assigned the minimum value of 2.2 W/m^2K. Time steps chosen were in accordance to the water residence times, rapid sweep was simulated using smaller time steps. In general, the time steps used were small enough for good temporal resolution with acceptable computer time.

Figures *5-3* through *5-5* compare calculated temperature transients with the measured data. The overall agreement is good. The largest discrepancies usually occur at the bottom layer (B-plane) and are probably due to the coarse model discretization near the cold water recharge inlet where very steep temperature gradients can result. Temperatures in the middle M-plane agree better, with the simulation predicting somewhat higher temperatures. The best comparison is obtained near the vessel exit (T-plane) where any temperature changes always take place slowly. The measured inlet temperatures (TC#109) were specified as model temperature boundary condition (the first approach described in subsection 5.3.2), a good match at the inlet IW-plane was obtained only for the short-term experiment 5-2. Others show lower predicted temperatures at the IW-plane as discussed in the preceding subsection.

Figure *5-3* indicates a good match between measured and computed water temperatures at all axial locations (except the IW-plane). The agreement was less satisfactory in the B-plane at early times. Results for experiment 5-2 given in Figure *5-4* show a good match for the IW-plane, but the computed water temperature is generally higher than measured values in the other planes. Results for experiment *5-3* given in Figure *5-5* show a good match for both M- and T-planes, but the computed water temperature is lower than that measured in the B-plane. Energy loss to the surroundings played an important role in this long (10.5 hr) run. In addition, the computed rock-center temperatures, which are represented by the average innermost shell temperatures, for both B- and M-planes in all three runs are significantly lower than the corresponding measured values. This aspect will be discussed further in the next subsection.

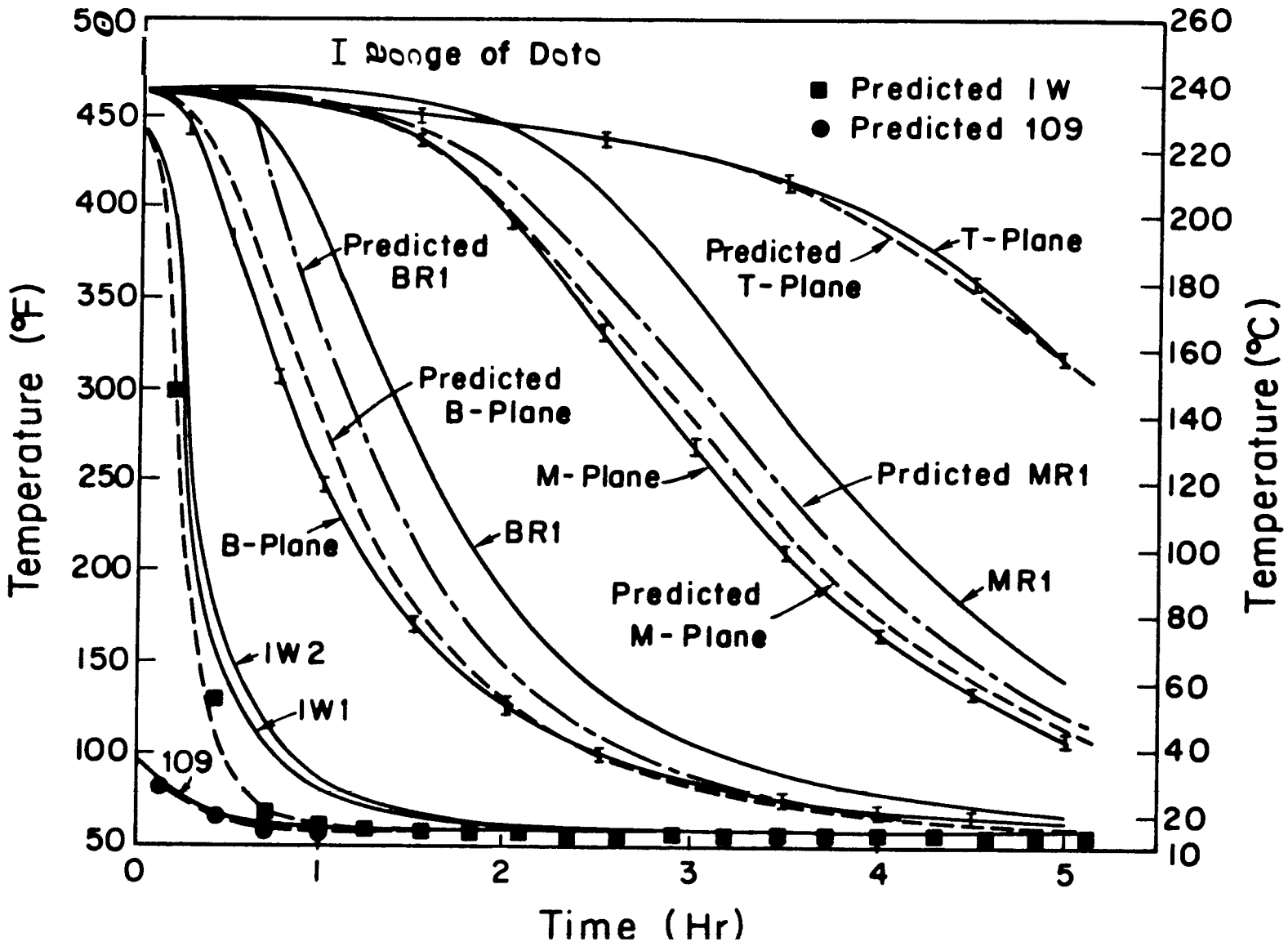

Fig. 5-3: Comparison of Measured and Predicted Water and Rock Temperatures for Heat Extraction Experiment 5-1 (constant rock conductivity)

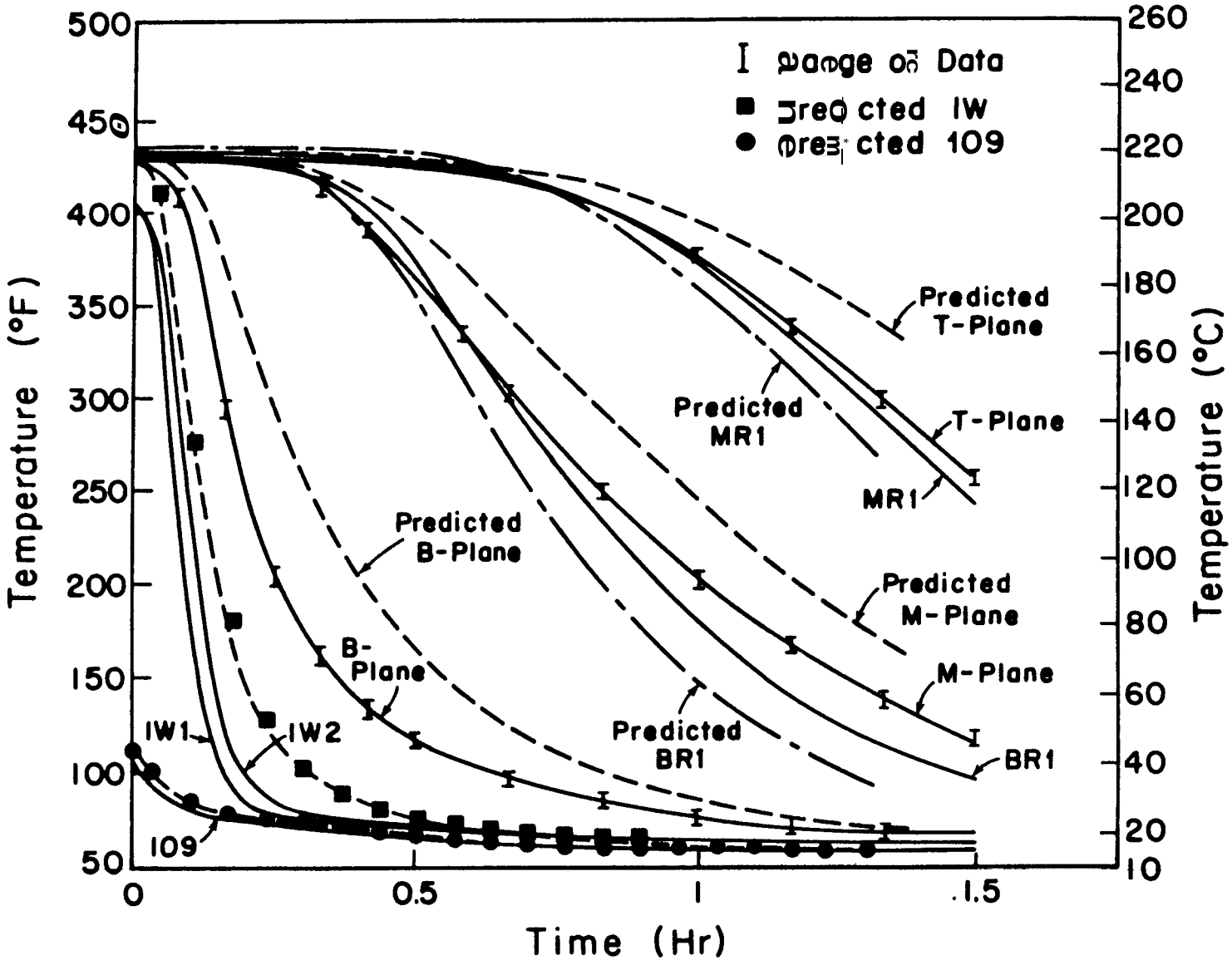

Fig. 5-6: Comparison of Measured and Predicted Water and Rock Temperatures for Heat Extraction Experiment 5-3 (constant rock conductivity)

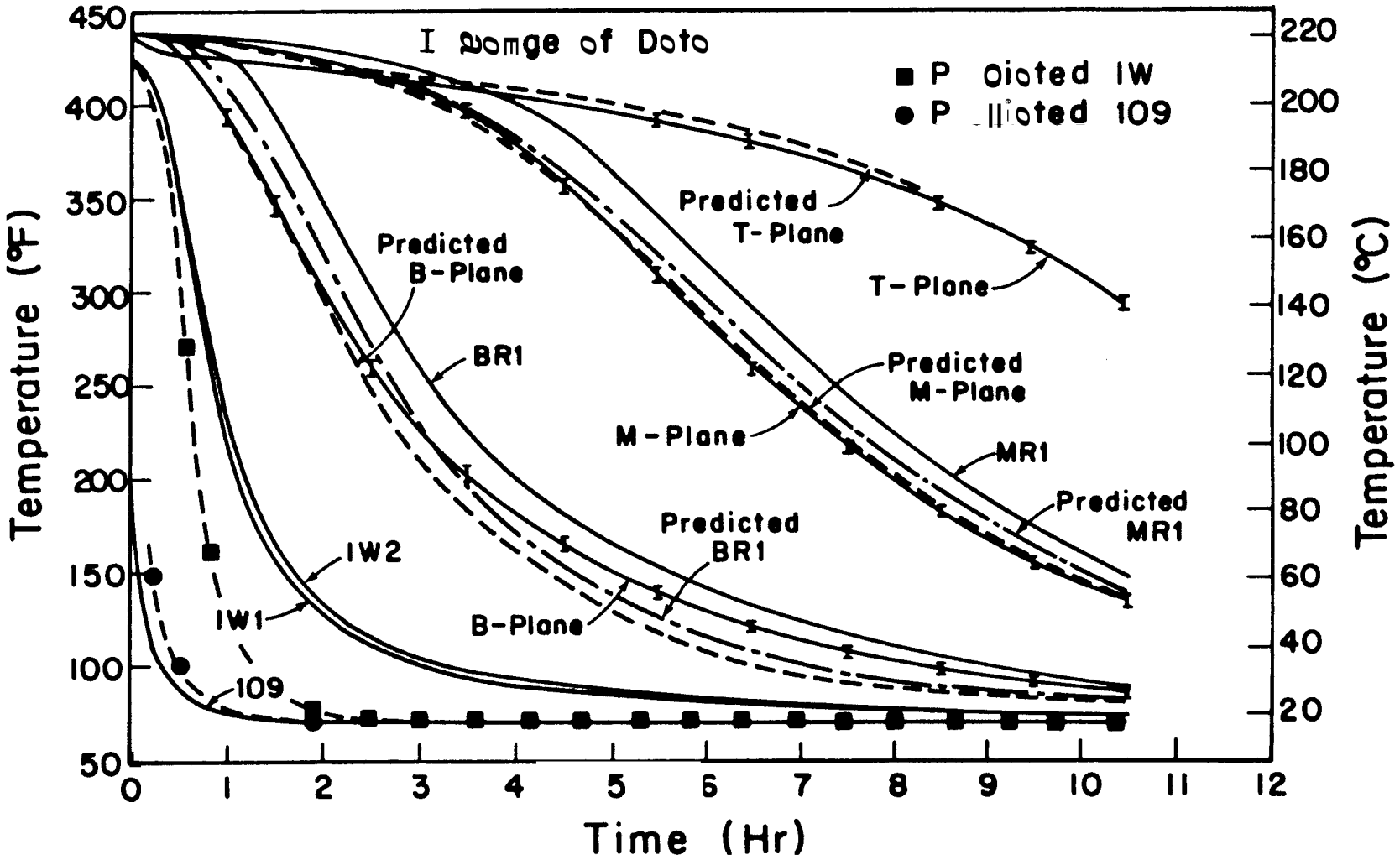

Fig. 5-5: Comparison of Measured and Predicted Rock Temperatures for Heat Extraction Experiment 5-3 (constant rock conductivity)

These comparisons led to the conclusion that besides the inlet region mismatch which could affect downstream predictions, some physical properties involved, and/or the modeling of the physical processes were inadequate. In particular, the previous results indicated that there could be too much heat transfer from the rock blocks to the water, possibly because the rock thermal conductivity value assigned might be too high. This aspect was investigated further.

5.3.4 Rock-Center to Water Temperature Difference Comparison

The computed and measured rock-center to average water temperature differences were compared for the B- and M-planes for the three experiments. The results for experiment 5-1 are given in Figure 5-6 for two different numerical model configurations; one with 4 shells and the other with 11 shells for each of the 60 layer elements. The computed rock-center to water temperature ($\Delta T_{r/w}$) was less than half of the observed value for the 4-shell model.

The discrepancy decreased when the number of shells per disk-layer element increased to 11. With 11 shells per layer, the volume of the innermost shell is 20.4 cm^3, i.e., equal to the volume of a sphere of radius 1.69 cm, the temperature of the innermost shell was expected to closely represent the rock center temperature, and be directly comparable to the temperature measured by the thermocouple located in the rock at this location.

Examination of Figure 5-6 shows that even with 11 shells per element layer (i.e., 10 shells of rock material), the $\Delta T_{r/w}$ computed are still below the observed. The reason for this is probably the relative large innermost shell (or block) size still may not represent the true rock center temperature since the computed value is an average temperature for this element. The other possibility is that the actual rock thermal conductivity was lower than the code input value, thus giving rise to a larger block energy extraction rate.

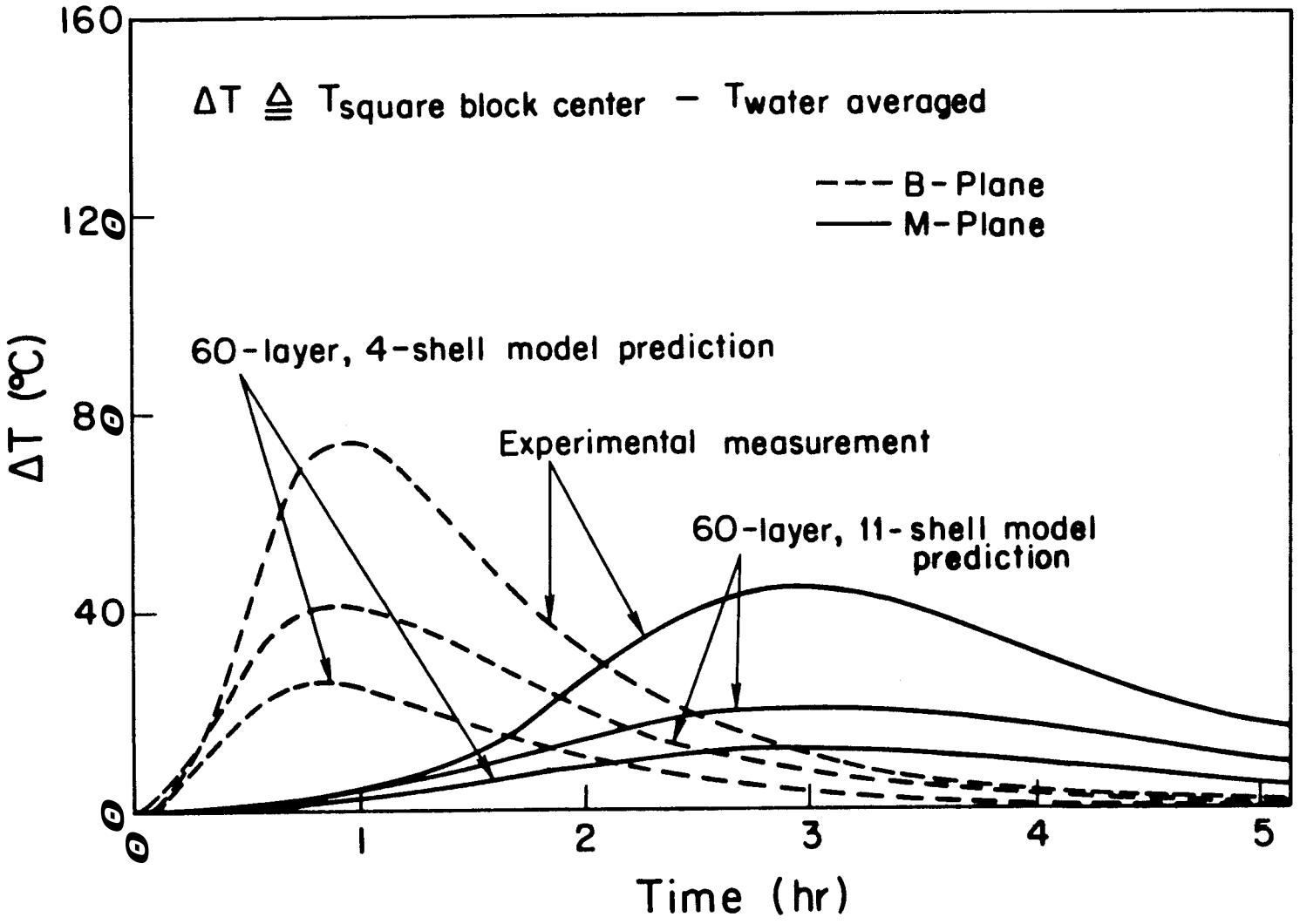

Fig. 5-6: Comparison of Measured and Predicted Rock-Center to Water Temperature Differences for Heat Extraction Experiment 5-1 (constant rock conductivity)

In these computer runs, the rock thermal conductivity value of 2.94 W/m^2K was based on extrapolation of one thermal conductivity data point measured at 65.5°C for the type of granite rock as explained in subsection 4.2.2. However, thermal stress induced microcracks may exist in the rock blocks as a result of the cold sweep; these microcracks can lower the thermal conductivity value. This effect and influences of rock water saturation level and elevated temperatures on thermal conductivity are being studied and will be addressed in separate reports. It is anticipated that the conductivity for a thermally-stressed rock is lower than for an unstressed rock of otherwise the same type and that this is the main reason for the less-than-satisfactory agreement between computed and measured block center temperature results.

The previous observation of lower predicted $\Delta T_{r/w}$ for the 4-shell model as compared to the measurements was more pronounced for the high-sweep-rate experiment 5-2, and of smaller magnitude for the long-residence-time experiment 5-3 ($\Delta T_{r/w}$ plots for these two experiments are not included in the report). Furthermore, the observed $\Delta T_{r/w}$ curve for experiment 5-3 skewed more toward early times, while the experiment 5-2 curve skewed less so in comparison with the almost bell-shaped experiment 5-1 measurement replotted on the same dimensionless time scale (normalized with respect to the corresponding flow residence time). This can be an indication of slightly different flow patterns established around the instrumented blocks in the three experiments.

5.3.5 Effects of Rock Thermal Conductivity

The influence of rock thermal conductivity on production experiment simulation is addressed in this subsection. The temperature dependence of conductivity is indicated in Figure 4-3. Using a fixed value of rock thermal conductivity could artificially enhance the predicted amount of energy extrac-

ted in the initial high temperature range, while at the same time, under-predict heat fluxes from the blocks later in the test. These two effects appear to counteract each other; the net result, however, could be smearing out of the actual steep rock temperature gradients. This effect was evaluated by using a linear temperature-dependent thermal conductivity relationship derived based on measurements and engineering judgment. Simulations for experiments *5-1* through *5-4* were then rerun with this conductivity characteristic and reevaluated.

As an example of the improvement in temperature predictions resulting from using the temperature-dependent conductivity, Figure *5-7* gives the temperature transients for a simulation of experiment *5-2.* In this simulation the measured inlet temperature history (TC#109) was also input as a temperature boundary condition. The model used *60* element layers with **11** shells per layer at the B-, M-, and T-planes *as* before. The water temperatures calculated are seen from Figure *5-7* to be higher than measured, however, significant improvements are obtained, particularly in the rock center temperature match with the new conductivity model.

The computed water temperature at the IW-plane is seen from Figure *5-7* to exceed measured values. This could cause the relatively higher water temperatures as compared to the observed values at other locations. This propagation of inlet temperature mismatch to upstream locations is believed to be a controlling factor that needed to be resolved. In the next subsection, the inlet temperature propagation effect will be resolved by adjusting the code input to reproduce the measured reservoir (rock loading and water in fractures) boundary temperature history.

Once this major influence is eliminated, it is believed that MULKOM and the numerical model should do a good job of predicting the water temperatures

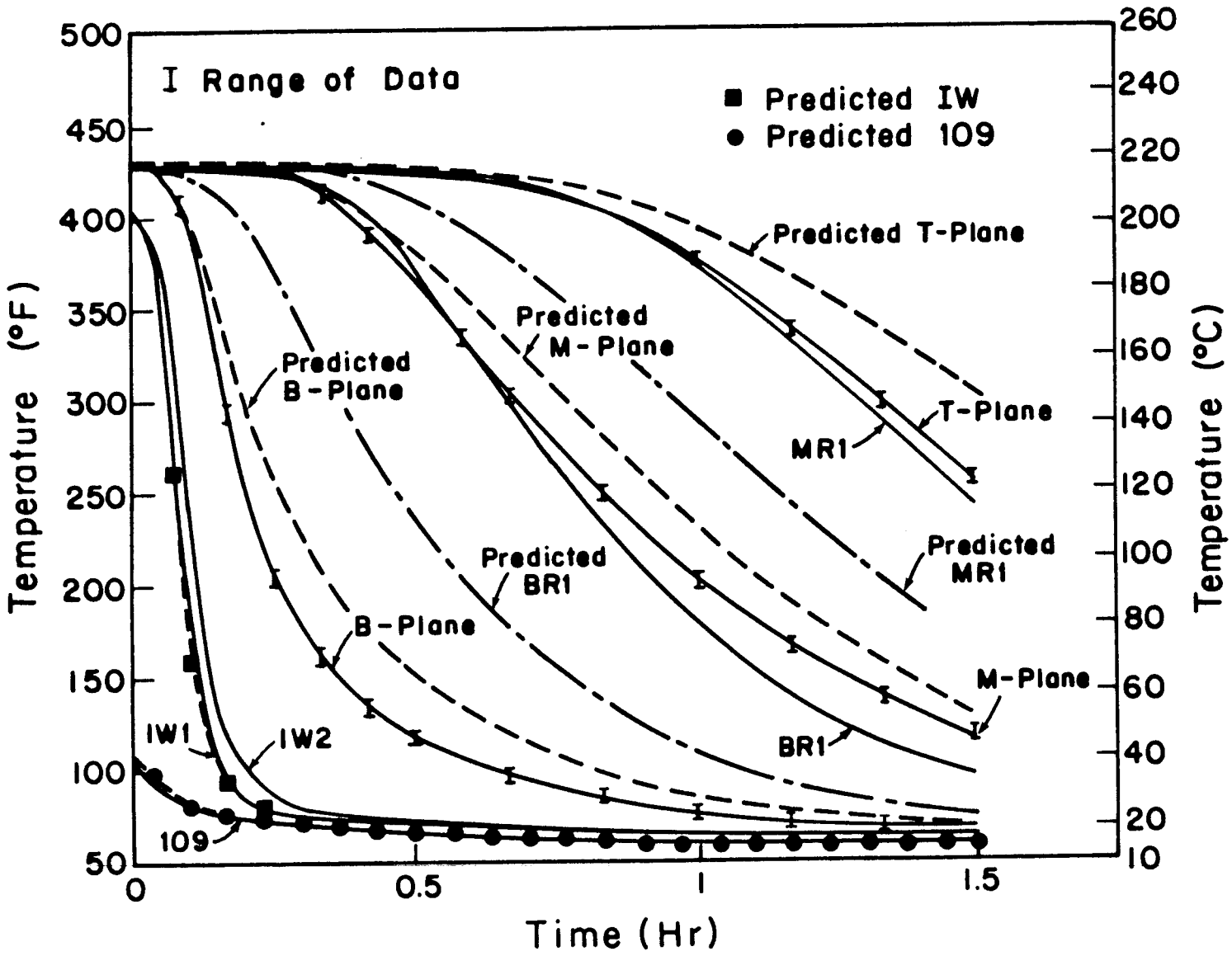

Fig. 5-7: Comparison of Measured and Predicted Water and Rock Temperatures for Heat Extraction Experiment 5-2 (temperature-dependent rock conductivity)

including the very steep temperature gradients occurring near the B-plane. The steep temperature gradients are demonstrated in the temperature-distance plots of experiment 5-1 given in Figure 5-8. This run was made with 60 element layers and measured inlet valve temperature boundary condition. It is clear that this computation mesh is sufficient to simulate sharp temperature slopes (~ 10°C/cm) near the flow baffle region.

5.3.6 Final Modeling Results

Additional modeling was made to model the series of experiments with greater accuracy by directly inputting flow enthalpy corresponding to the observed baffle plane temperature (IW-plane) as discussed in subsection 5.3.2. The additional computer runs for experiments 5-1 through 5-3 were done with the 60-layer, 11-shell (at the instrumented planes only) mesh, a constant wall conduction path length model (see Table 5-5 for its effects), and linearly varying thermal conductivity. Heat loss parameters were specified as before at 2.8 W/m^2K, 3.8 W/m^2K and 2.2 W/m^2K, respectively.

Figure 5-9 shows a typical result for experiment 5-2. Overall predictions do not improve appreciably over the constant conductivity predictions given in Figures 5-3 through 5-5 in which the inlet valve enthalpy was directly input. In general, the calculated water temperatures including the IW-plane temperature, are much higher than previous predictions and deviate even further from actual measured values. One possible explanation is that the temperature dependent conductivity, which assigns a lower rock conductivity value at the higher T-plane rock temperatures in comparison with the B-plane, causes more heat flux flowing into the water from the rock blocks in the lower portion (B-plane) of the vessel, thus leading to higher IW- and B-plane temperatures. Another reason is the mismatch propagation effect delineated before.

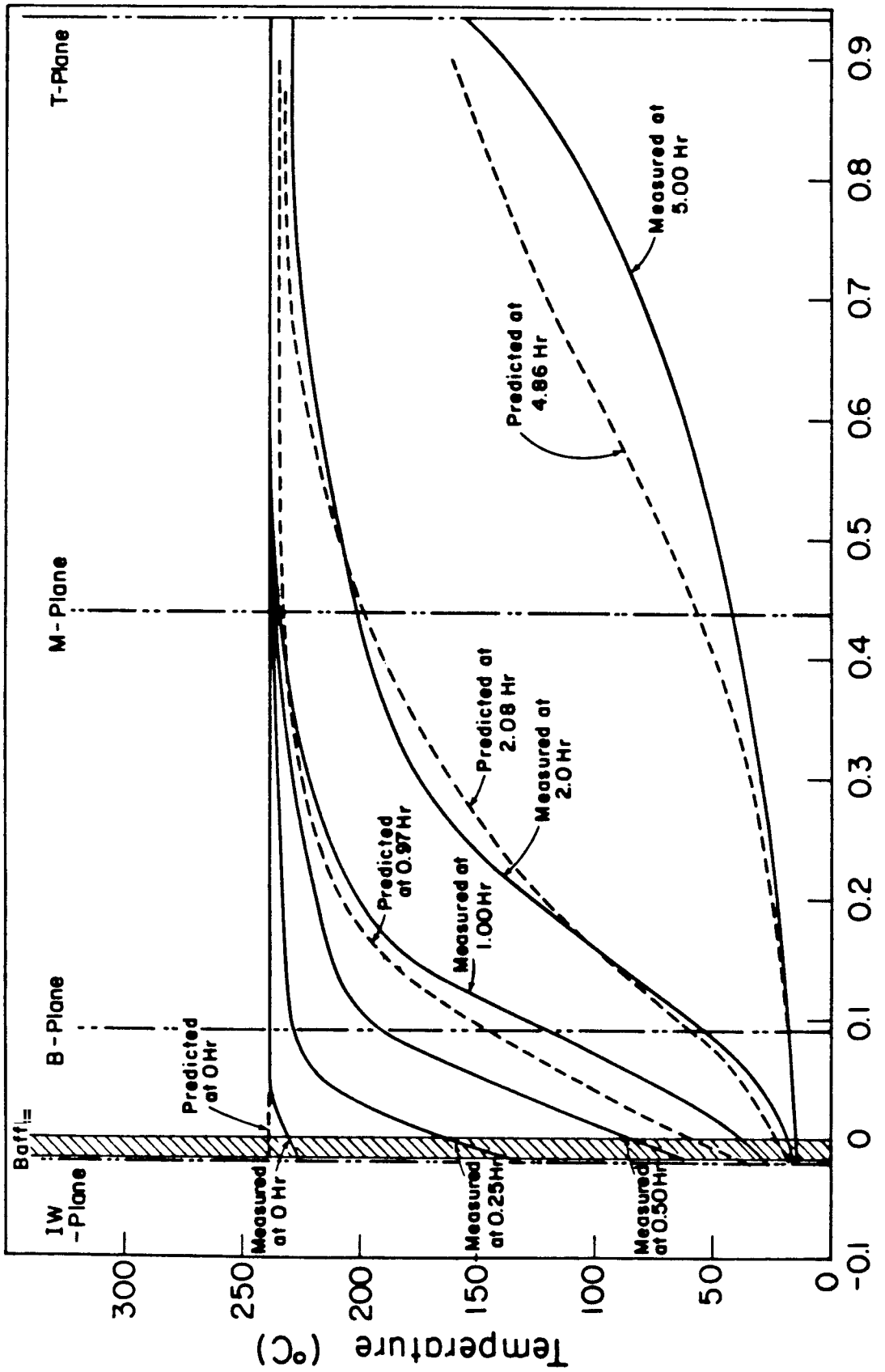

Fig. 5-8: Comparison of Measured and Predicted Water Temperature for Heat Extraction Experiment 5-1 (constant rock conductivity)

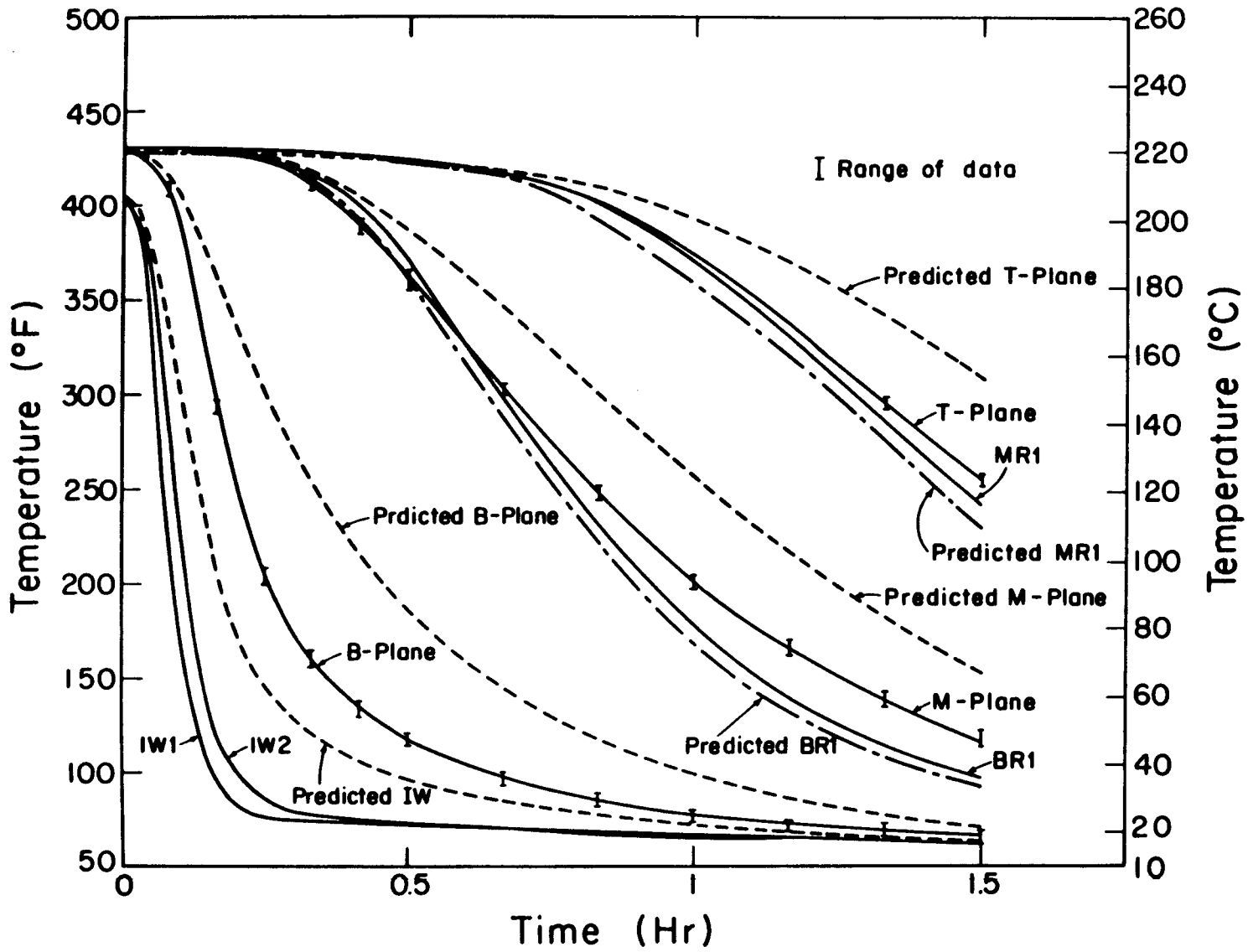

Fig. 5-9: Comparison of Measured and Predicted Water and Rock-center Temperatures for Heat Extraction Experiment 5-2 (temperature-dependent rock conductivity

A series of computer runs were subsequently made using temperature dependent rock thermal conductivity and IW-plane enthalpy input by trial and error to obtain better final modeling results. Final results are presented in Figures 5-10 and 5-11 for experiments 5-1 and 5-3, respectively.

In this final modeling effort, the LBL simulator was used in a mode that simulated the IW-plane temperature history as closely as possible, and at the same time, the code used the fine computation mesh and variable rock conductivity to obtain good resolution, accurate temperature gradients, and heat loss computation. Heat loss parameters were set at 2.8 W/m^2K and 2.2 W/m^2K, respectively, for the two runs. The resulting calculations yield results sufficiently close to the test data as indicated in Figures 5-10 and 5-11.

It is recognized in the previous simulations (Figure 5-9) that direct input of node enthalpies corresponding to the node measured temperatures at either the inlet valve or the flow baffle region could produce calculated temperatures at these nodes far higher than the expected measured value (see Figure 5-7 and Figure 5-9). This is caused by thermal diffusion from adjacent nodes which can result in temperature mismatch propogation downstream from the boundary nodes (T/C#109 or IW). In Figures 5-10 and 5-11, the IW-plane temperatures were duplicated closely through a trial and error procedure in which relatively lower enthalpies than corresponding measured values at this elevation were input.

The calculated IW-plane temperatures agree well in the final runs made except later in the transients when they stay below actual measurements because of the low boundary temperatures specified. Very good agreements are also obtained at the B-plane during the initial portion of the three experiments. M- and T-planes tend to have slightly higher predicted temperatures. The overall agreement is satisfactory and it is reasonable to anticipate that

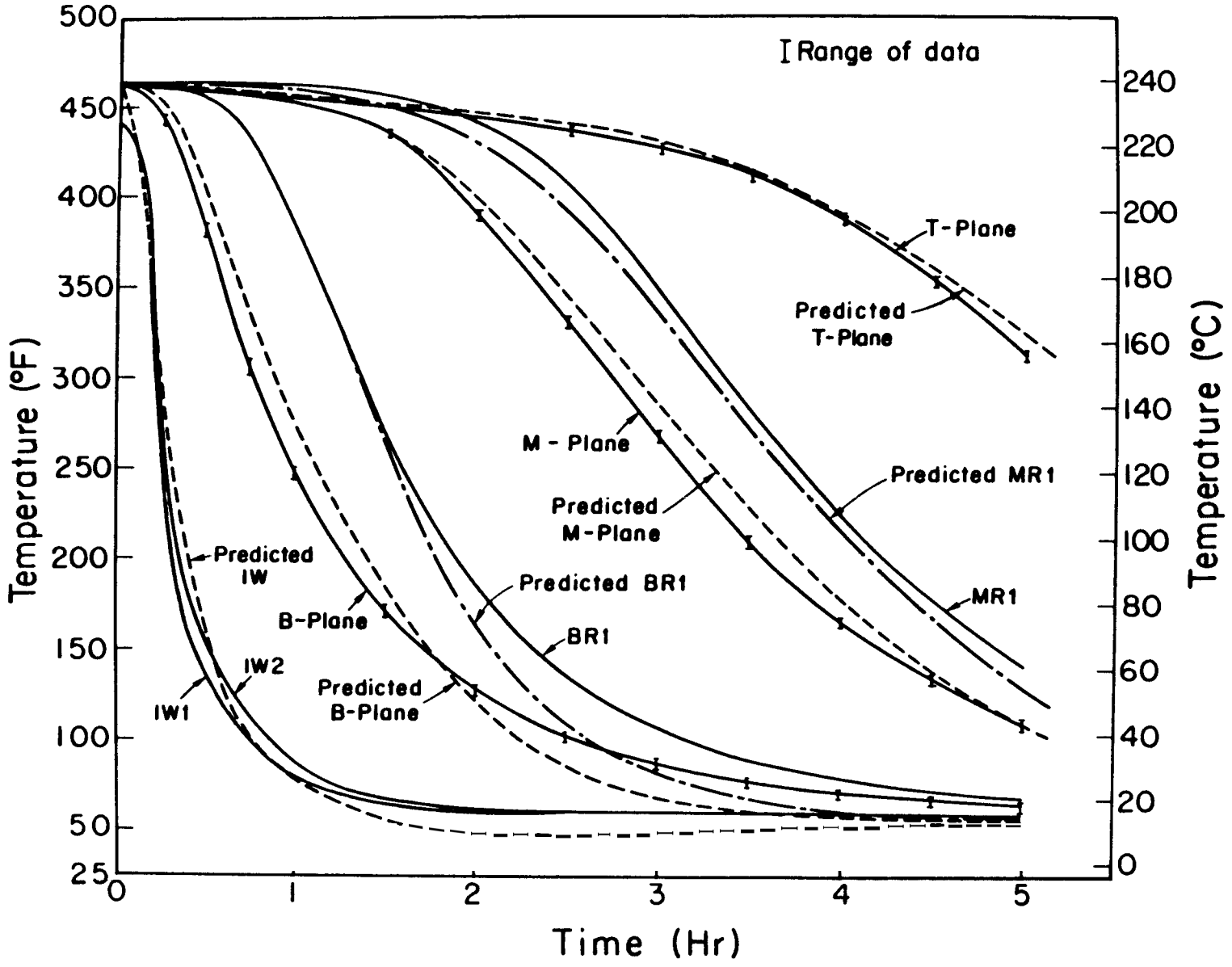

Fig. 5-10: Comparison of Measured and Predicted Water and Rock-center Temperatures for Heat Extraction Experiment 5-1 (temperature-dependent rock conductivity)

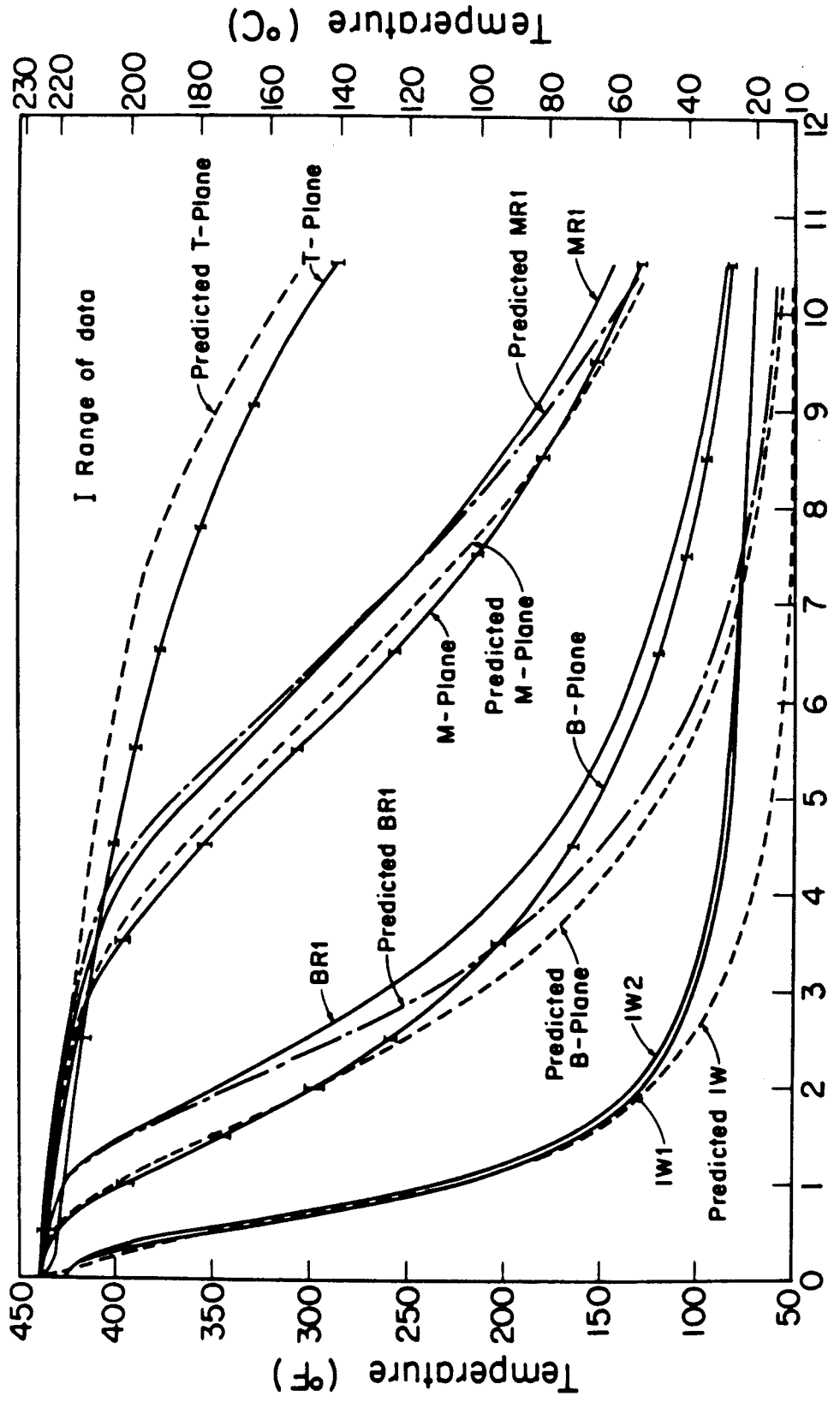

Fig. 5-11: Comparison of Measured and Predicted Water and Rock-center Temperatures for Heat Extraction Experiment 5-3 (temperature-dependent rock conductivity)

a better match at the IW-plane long-term behavior will produce an even better match for the B-plane long-term response. This will not affect the higher elevation predictions to any significant extent, i.e., the M- and T-plane temperatures are approximately immune to this temperature adjustment. Furthermore, the M- and T-plane overpredicted temperatures can be brought down by raising the corresponding heat loss parameters.

5.4 Parametric Evaluation Summary

A parametric study was performed to identify key physical and computational parameters, so that maximum accuracy could be obtained at reasonable computer cost and the major parameters could be evaluated and monitored more carefully. Over 40 computer runs have been made to identify the relative importance of various parameters, such as mesh size, wall thermal conduction path length, time step, heat loss parameter, vessel boundary condition, and rock thermal conductivity, which were believed to represent the parameters with the greatest uncertainty. Detailed results of many of these runs were presented in subsections 5.2 and 5.3. This subsection presents a concise summary of all cases run.

A reference case was selected to compare results from other cases. The reference case (for experiment 5-1) had 30 layers of rock disk elements with 4 shells per element, a rock thermal conductivity of 2.94 W/mK, a maximum time step of 250 sec, a uniform conduction path length along the vessel walls, a heat loss parameter $\nu = 2.80$ W/m^{2}K, and the measured inlet water temperature as input. This value of ν resulted in a good match with the system experimental cooldown curve as discussed in section 5.2. The results for this reference case (not given here) show that computed water temperatures were, in general, slightly higher than the corresponding measured temperatures through-

out the entire production period. Table 5-5 summarizes the major effects observed in a semi-quantitative manner as a function of important parameter changes for some of the computer runs for which detailed data comparisons were made.

Results of the parametric evaluation indicate that the two parameters which had significant influence on numerical results were: **(1)** system boundary conditions (including the heat loss parameter ν), and (2) material properties, especially rock thermal conductivity. Adjusting these two parameters produced acceptable results when a sufficiently refined mesh size and time step were used. It must be recognized that a rock matrix sweeping with fast flows would require more shells per element for correct temperature calculations especially near the temperature measurement planes. The evaluation also indicates that temperature dependent thermophysical properties should be used whenever available. In addition, correctly specified model boundary conditions have to be defined to attain good agreements. Finally, when the heat loss parameter ν varied from 2.20 W/m^2K (for $\Delta T \cong 46°C$) to **3.80** W/m^2K (for $AT \cong 219°C$), corresponding matrix and fluid temperature changes are not dramatic. This implies that system heat loss, though important, is not the most critical modeling parameter, and that the semi-quantitative approach adopted in subsection 5.2 should be adequate.

Besides identifying the important parameters and studying the sensitivity of the model to variations in these parameters, the parametric investigation also provided evidence that none of the data comparison studies performed contained unacceptable significant errors due to inexact phenomena modeling assumptions or incorrect model input information.

Table 5-5

SENSITIVITY STUDY **SUMMARY**

Run	Major Parameter Changed	Major Effects Observed
1	Reference case (Expt. 5-1)	Fair agreement with test data
2	60 layers, 4 shells/layer	Moderate change in water temp. T ~ 5°C, Lowered T-curve at small distance x, Raised T-curve at large x for time $\tau \gtrsim 1$ hr
3	Half time step (maximum $\Delta\tau$ = 125 sec)	Little change in T, T-curve lowered ~ 5°C
4	Finer grid for inside layers 11 shells/layer for all 30 layers	Insignificant change(1) in T, Block center T higher by ~ 1°C
5a	Higher heat loss parameter v = 3.80 W/m^{2}K	Insignificant change in T, Lowered T-curves by ~ 2°C at B- and M-planes for large τ
5b	Lower heat loss parameter v = 2.20 W/m^{2}K	Little change in T, T-curves raised ~ 5°C
6	Baffle thermal conductivity = 0	Insignificant effects
7a	Shorter characteristic conduction path length(2) near lower flange (30% of original length)	Little change, T-curves lowered by ~ 5°C
7b	Variable conduction path length axially (20%-50%)	Lowered T-curves by ~ 7°C for $\tau \gtrsim 1$ hr, increased heat loss
8	Finer gridding near B-, M-, and T-planes (11 shells/ layer)	Insignificant change in T, rock-center temp. prediction improved
9a	Smaller inlet plenum volume (81.8% of original volume below flow baffle)	Little change in T by ~ 3°C T-curve lowered for $\tau \gtrsim 2$ hr
9b	Smaller inlet plenum (66.8%)	Little change in T by ~ 3°C
10	Rock thermal conductivity k = 2.42 W/mK	Little effects
11	Combined 1, 2, 3, 7b & 9b (Experiment 5-1, Fig. 5-3)	Improved agreement with test data

12	Increase rock porosity to 1 percent	Little change, reservoir overall thermophysical properties changed accordingly
13	Linearly varying rock conductivity with temperature	Little change in T, predicted T-curve shapes follow data more closely
14	Computation model boundary condition	Matches at IW-plane significantly improved higher system elevation results. Directly input temperature at IW-plane has more influence than input measured temp. of T/C#109 at the vessel inlet
15	Combined 1, 2, 3, 5a, 5b, 8, 9b, 12, 13, and 14 (see Fig. 5-10)	Satisfactory agreement

(1) Insignificant changes or effects means T changes less than 8.5°C, the estimated combined measurement and numerical uncertainties.

(2) The characteristic conduction path length is defined as an effective length dimension used to model thermal conduction in an irregularly-shaped solid with a single lumped temperature node. This defined length facilitates the application of the 1-D MINC method to complex geometric systems.

6. DISCUSSION

This analysis has provided sufficient evidence that time and budget are the only constraints to better model/data match. The computation model is capable of simulating the physical model tests with acceptable resolution level over the range of anticipated conditions in the test series.

During the course of modeling, it has been demonstrated that the code is capable of: (1) following steep temperature gradients, (2) reproducing the test temperature histories, and (3) serving as a useful tool for data interpretation and temperature predictions within the range of parameters investigated. It should be emphasized, however, that a very substantial effort was

relatively complex system. Nevertheless, modeling of the thermal sweep process and the postulated reduction in granite rock thermal conductivity in cold water sweep flow was quite successful. The following subsections will improvements, and future work separately.

6.1 Possible Sources of Errors

An assessment of the quality of data obtained from the series of experiments was performed. Results of an earlier uncertainty evaluation for the physical model were presented by Hunsbedt, Kruger, London (1975). This subsection briefly reviews error sources and estimates error magnitudes for the present physical model tests and for the LBL reservoir simulator. Such an estimate is essential in assessing the significance of any small change in either the physical model or the simulator behavior.

The static errors in the prime measurements (e.g., temperature and water flow rate) are basically due to three sources: (a) instrument errors (including temperature sensitivity, zero shift, repeatability, hysteresis, nonlinearity, etc.), which can be evaluated by utilizing the manufacturers' specification sheets or calibration information; (b) data acquisition system characteristics (including instrument response, signal conditions, etc.); and (c) analog recording and chart reading errors.

Temperature measurement uncertainties were primarily determined by the thermocouple accuracies. Standard error limits for the thermocouple measurements, as published by the Instrument Society of America (ISA), can be con-

effects, nonlinearity, readout resolution, etc. Additional errors can result from slight variation in thermocouple positioning in the water or in the rock blocks. This can produce errors in temperature readouts that are not easily quantified.

Based on engineering .judgment and supported by recorder plots and cross comparisons with other thermocouples and thermometers installed in the laboratory room for checking the initial system temperature conditions, it is estimated that the uncertainty in water temperature measurement is about ±3°C. The uncertainty in the rock and metal temperatures is estimated to be larger (±6°C) mainly because of the additional uncertainties associated with sensor location and thermal contact resistance. The total uncertainty in a measured quantity (e.g., temperature) was obtained based on a "scaler error" formula used to combine independent errors of the measured quantity's independent variables for a single sample experiment (Kline and McClintock, 1953) whose measurement uncertainties do not have a statistical analog.

Mass flowrate measurement uncertainty mainly arises from weight scale resolution, nonlinearity, and hysteresis. However, additional errors exist because of the difficulty in maintaining a completely constant flow rate during the early part of the experiment. These uncertainties were factored into the total uncertainty for the mass produced which is estimated to be ± 5 lbm. Pressure measurements were made to assure sufficient margins exist in maintaining above-saturation system pressures. They are of secondary nature and therefore not considered in this uncertainty analysis.

There is no simple way to estimate the accuracy of the LBL reservoir simulator and the MINC method employed in our modeling studies. Partial validation of the MINC method (Lai, 1982) showed excellent agreement with some analytical results, thus indicating minimal numerical error for those condi-

tions. In general, uncertainties in input information will propagate to the calculated output nonlinearly; this, together with the basic code formulation assumptions, are the major potential error sources for the simulation. The complexity of the MULKOM model prohibits a straight forward yet rigorous complete output verification. However, some simpler procedures can be done to reduce any output errors. Firstly, a visual verification can be done to assure that proper prediction variables, are obtained. Then an order of magnitude judgment of the output and a comparison with existing similar analyses results should eliminate some obvious errors. Finally, a mass and energy conservation check can be performed on the vessel system (partially or globally) to make sure that no inconsistency exists in the run.

It is also possible to systematically analyze how each parameter uncertainty amplifies or attenuates in a specific input set up, but this has not been done. Nevertheless, it is assumed that the estimated uncertainty in the predicted temperatures is of the same order as the measurements, i.e., ±6°C. This uncertainty estimate was based on the premise that any input error would not magnify considerably at the output.

The philosophy adopted in the acceptance criterion for the model/data comparison is that the difference in predicted and measured values should be less than the square of the sum of each individual uncertainties (or standard deviations). Thus, for the comparison task, an acceptable temperature difference should be around $\pm (6^2 + 6^2)^{0.5} = \pm 8.5°C$. If the results do not match within this value, it can be concluded that input parameters or modeling assumptions relative to the details of the physical system configuration and the physical phenomena are not adequate.

6.2 Implications from Modeling Results

In the course of performing the model/data comparisons, a number of points arose that deserve more discussion. They will be considered separately in this subsection.

1. The heat extraction process can be highly dependent on the thermal conduction in the rock matrix. A high sweep velocity will remove rock energy mainly from the vicinity of rock/water interfaces while the rock center temperature does not change significantly. This heat-transfer-limited characteristic at fast sweep is demonstrated in Figure 6-1 where the maximum rock-center to water temperature difference ΔT_{max} is plotted as a function of production rate for the B- and M-planes. It is noted from Figure 6-1 that at a low flow rate, ΔT's at B- and M-planes are similar, but they deviate more from each other as the flow rate increases. The same observation can also be seen in the heat transfer parameter N_{tu} plotted versus production rate for the three production tests. This limitation on energy depletion rate is also a function of the block size, heat transfer surface area, thermal conductivity and diffusivity, and rock permeability if the rock is sufficiently porous. However, energy removal rate will become more flowrate and fluid temperature dependent where the water residence time is long. This is evidenced in changes in curve slopes from steep to moderate with increasing flow rates in Figure 6-1.

2. Review of the measured water temperature data shows that at high sweep rates as in experiment 5-2, temperature variations in a cross section normal to the flow direction become larger. For example, water temperatures measured at T/C BW3 and **BW6** or BW7 could be different by as much as 8°C which is considerably larger than for the other tests. This observation may indicate a change in flow patterns, such as transition from laminar to

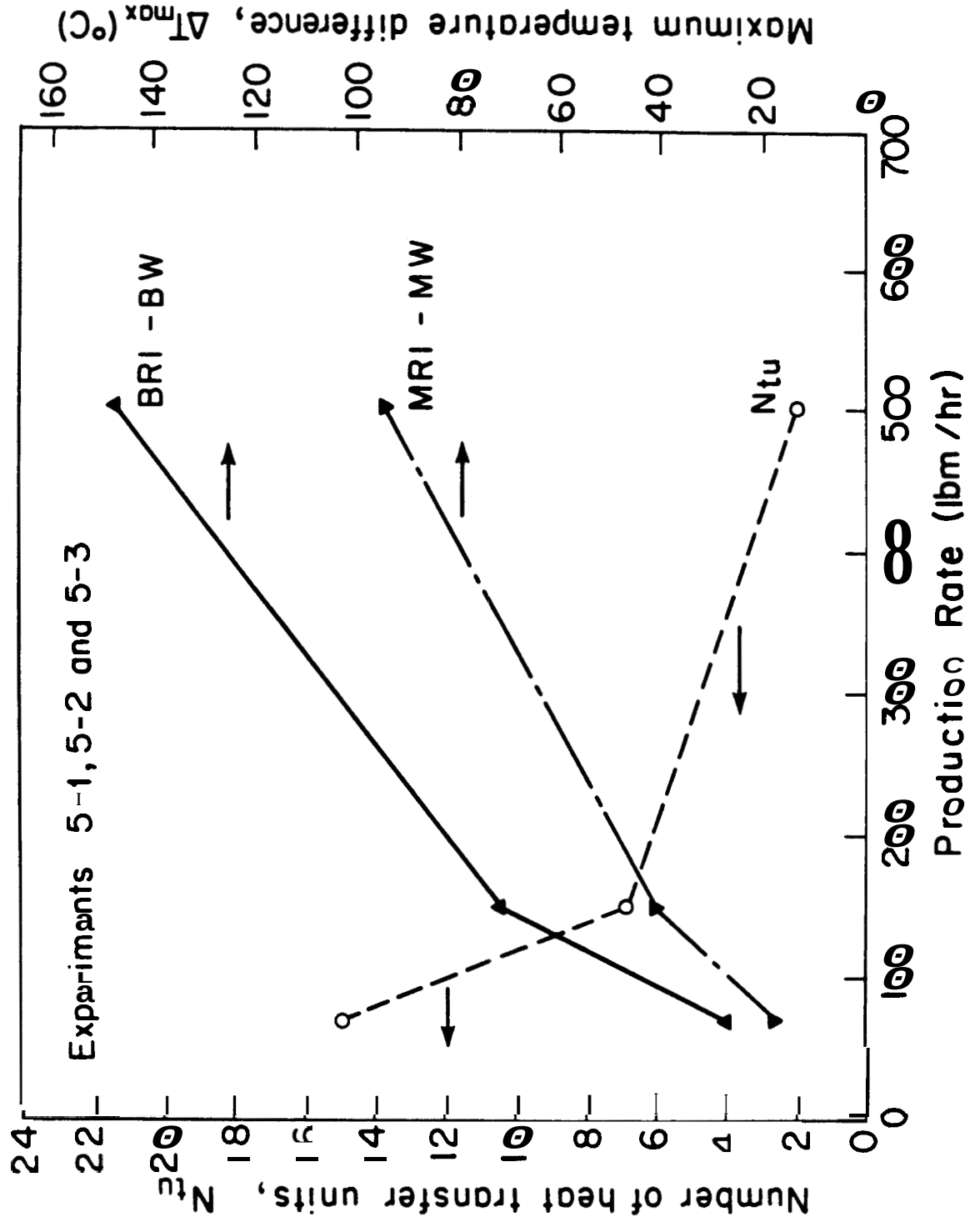

Fig. 6-1: Effect of Recharge Rate on Rock-center to Water Temperature Differences for Heat Extraction Experiments

turbulent flow locally, or the existence of plane cross flows and flow separations. This phenomenon may not occur in large-scale field exploitation, however, appropriate attention should be directed to it in situations where high production rates prevail in the fields.

3. It has been implied from the parametric study discussed in subsection 5.4 that the number of shell partitions for each element layer is not critical in computing the correct rock surface heat flux, provided that sufficiend shells are included for the particular block size and sweep rate (e.g., 4 shells minimum). This feature can help save computer cost by using a relatively coarse mesh for most of the rock matrix and a finer mesh at the physical model measurement planes.

4. One of the major difficulties encountered in interpreting physical, model temperature data comes from the presence of the steel mass and the insulation layer. Thus, the model lateral boundary condition cannot be properly controlled at the water/steel interface during the experiments and has to be simulated using analytical models similar to those used for the rock matrix. However, the irregular geometry of the pressure vessel configuratiod not only prevents the use of most mathematical analysis techniques, but also makes it difficult to model using a reservoir simulator like **MULKOM.** The result is a set of test data and a numerical model some uncertain parameters related to the physical system. This hampers both code prediction capabilities and the usefulness of expeimental data from the physical model.

5. The steel vessel mass contributes significantly to the initial system energy content and subsequent system temperature transients during tests. The steel thermal capacitance results in higher overall water temperatures as well, as rock temperatures relative to those that would result without the presencq of the pressure vessel. It also increases the thermal breakthough time. One

of the most important applications of the numerical model (calibrated) is to provide a means of studying physical. model performance in more realistic environments having adiabatic or constant-temperature or a combination of these boundary conditions. To show the influence of the vessel steel structures, a sample case was run in which the presence of the steel was removed artificially and the results are presented in Appendix B.

6.3 Possible Improvements to Experimental System and Simulator

Only the single phase flow computational capability of MULKOM has been exercised in the current model comparisons. Other important features such as simulating multiphase flows have not been studied. The LBL simulator is undergoing continuous development by LBL. Some relatively recent improvements include implementation of a pre-processor for the MINC method to facilitate the tedious mesh generation and save computation cost, and inclusion of a stochastic fracture distribution modeling capability. The list presented in the following represents some additional points worth consideration:

1. Develop routines for handling temperature or pressure dependent thermophysical properties for some crucial reservoir components such as rocks, especially in cases where phase change or thermal moving fronts exist in the reservoir, which can induce rapid changes in local temperature or pressure;

2. Add the option of interactive computer plots for selected output results.

MULKOM is capable of treating rather complex transient three-dimensional reservoir problems with variations of some material properties and realistic boundary conditions. However, application of the simulator, especially setting up the input and interpretation of output, requires some degree of user-familiarity with the code which is often costly and time donsuming.

Therefore, one possible improvement is to make MULKOM more user-friendly. Another concern is the inherent volumetric averaging built into the model; this may limit the accuracy of localized thermal transient predictions.

The experimental facility can be further improved by:

1. Increasing the number of sensors (both direct and indirect backups to sensors of primary nature) and instrumentation signal channels. More temperature sensors would be useful to continuously monitor steel vessel walls, insulation blanket surface and ambient air temperatures during experiments.

2. Improving the production flow control valve to provide better flow rate control. However, the adverse effects of boundary heat loss and vessel heat capacity remain a disadvantage of the large-scale high pressure, high temperature physical setup in some studies. Unfortunately, little can be done to correct this because of the usual high pressure environment required.

6.4 Recommendations for Future Studies

Since satisfactory model/data camparisons have been obtained for the current experiments, it is not recommended to continue the simulation effort. However, consideration should be given to analyze the two-phase-boiling experiment already performed in the physical model. The following outlines some general recommendations for future users of the Stanford *Geo*–thermal Reservoir Model and MULKOM to similar studies.

1. The test setup is quite suitable for investigating statistical energy recovery characteristics of a random irregular rock loading. Such an energy recovery process can then be analyzed with a lumped-parameter mathematical model in which some vaguely quantified parameters can possibly be averaged out. The facility is also quite suitable for providing an elevated temperature/pressure well-controlled environment for detailed study in

rock/water heat transfer processes and other related aspects such as thermal stressing of a small number of well-instrumented rock blocks. Any global reservoir performance type of analysis in the future should consider utilizing appropriately shaped block loading which is geometrically compatible with the pressure vessel to facilitate data interpretation, and pre- and post-test model analysis.

2. A large complex numerical simulator such as MULKOM is most useful id interpreting and designing laboratory study only after sufficient details and information for preparing its input become available. That is, the numerical model needs to be calibrated against the particular physical setup before making any pre- or post-test calculations.

3. In addition to the adiabatic case studied (Appendix B), a computed run can also be made for the physical model configuration using constant-temperature boundary conditions. These two cases should constitute a bounding envelope for more realistic field boundary conditions.

4. A data base has been established for simulating single-phase sweep production experiments. It is anticipated that, with minor modifications to the input parameters, MULKOM can be calibrated against two-phase test situations, and thus become a major tool in designing instrumentation locations and an efficient test matrix for future two-phase experiments.

7. REFERENCES

Anand, J., W. H. Somerton, and E. Gomaa, "Predicting Thermal Conductivities of Formations From Other Known Properties," Society of Petroleum Eng. J., pp. 267-273, October, 1973.

Carslaw, H. S. and J. C. Jaeger, Conduction of Heat in Solids, Oxford University Press, Oxford, England, Second Edition, 1959.

Duff, I. S., MA28 - A Set of FORTRAN Subroutines for Sparse Unsymmetric Linear Equations, AERE Harwell Report R-8730, July 1977.

Hunsbedt, A., S. T. Lam, and P. Kruger, User's Manual for the 1-D Linear Heat Sweep Model, Stanford Geothermal Program Technical Report No. 75, August, 1983.

Hunsbedt, A., S. T. Lam, P. Kruger, and K. Pruess, "Heat Extraction Modeling of the Stanford Hydrothermal Reservoir Model," Proceedings, Eighth Workshop on Geothermal Reservoir Engineering, SGP-TR-60, Stanford University, Stanford, CA, December, 1982.

Hunsbedt, A., R. Iregui, P. Kruger, and A. L. London, "Energy Recovery from Fracture-Stimulated Geothermal Reservoirs," Paper 79-HT-92, Proceedings, ASME/AiChE 18th National Heat Transfer Conference, San Diego, California, August, 1979.

Hunsbedt, A., P. Kruger, and A. L. London, A Laboratory Model of Stimulated Geothermal Reservoirs, Stanford Geothermal Program Technical Report No. 7, Report to National Science Foundation, Grant No. GI-34925, February, 1975a.

Hunsbedt, A., P. Kruger, and A. L. London, Laboratory Studies of Stimulated Geothermal Reservoirs, Stanford Geothermal Program Technical Report No. 11, Report to National Science Foundation, Grant No. NSF-03490, December, 1975b.

International Formulation Committee, A Formulation of the Thermodynamic Properties of Ordinary Water Substance, IFE Secretariat, Düsseldorf, Germany, 1967.

Iregui, R., A. Hunsbedt, P. Kruger, and A. L. London, Analysis of the Heat Transfer Limitations on the Energy Recovery from Geothermal Reservoir, Stanford Geothermal Program Technical Report No. 31, January, 1979.

Kelly, M., Missouri Boiler and Pressure Vessel, private communication, Feb. 1983.

Kline, S. J. and F. A. McClintock, "Uncertainties on Simple Sample Experiments," Mechanical Engineering, January, 1953.

Kuo, M. C. T., P. Kruger, and W. E. Brigham, Heat and Mass Transfer in Porous Rock Fragments, Stanford Geothermal Program Technical Report No.10, 1975.

Lai, C. H., personal communication, 1982.

Moen, R. A., Thermophysical Properties of Ferrous Structural Alloys, Hanford Engineering Development Laboratory Report, HEDL-TME 78-47,. April, 1978.

Nuclear Systems Materials Handbook, Rev. 5, HEDL-TID 26666,1980.

Pruess, K., Development of the General Purpose Simulator MULKOM, Annual Report 1982, Earth Sciences Division, Report LBL-15500, Lawrence Berkeley Laboratory, 1983a.

Pruess, K., GMINC - A Mesh Generator for Flow Simulations in Fractured Reservoirs, Lawrence Berkeley Laboratory Report LBL-15227, Berkeley, CA, March 1983b.

Pruess, K. and K. Karasaki, "Proximity Functions for Modeling Fluid and Heat Flow in Reservoirs with Stochastic Fracture Distributions," Proceedings, Eighth Workshop on Geothermal Reservoir Engineering, SGP-TR-60, Stanford University, Stanford, California, December, 1982.

Pruess, K. and T. N. Narasimhan, "A Practical Method for Modeling Fluid and Heat Flow in Fractured Porous Media," Proceedings Sixth SPE-Symposium on Reservoir Simulation (paper SPE-10509), New Orleans, February, 1982. (to appear in Soc. Pet Eng. J.)

Pruess, K. and R. C. Schroeder, SHAFT79 User's Manual, Lawrence Berkeley Laboratory Report LBL-10861, Berkeley, March, 1980.

Ramey, H. J. Jr., P. Kruger, R. N. Horne, W. E. Brigham, and F. C. Miller, Geothermal Reservoir Engineering Research at Stanford - Second Annual Report, Stanford Geothermal Program Technical Report No. 61, September, 1982.

Sass, J. H., A. H. Lachenbruch, R. J. Munroe, G. W. Green, and T. H. Moses, Jr., "Heat Flow in the Western United States," J. of Geophysical Research, 76, No. 26, 6376-6413, Sept. 10, 1971.

Somerton, W. M., private communication, 1982.

Appendix A

LISTING OF MULKOM INPUT FOR SIMULATION OF EXPERIMENT 5-2

(Illustrated in Figure 5-7)

This appendix contains the input deck listing for experiment 5-2 numerical model in which the inlet valve temperatures (T/C#109) are directly input as an unsteady temperature boundary condition. Detailed explanation of most input parameters can be found in the SHAFT79 User's Manual (Pruess and Schroeder, 1980) as the SHAFT79 input formats are virtually identical for those employed in MULKOM. This listing contains all principle features of a typical MULKOM simulation run input information. Input files for other physical model experiments simulations can be easily obtained with minor modifications to the input file listed in Table A-1.

Table A-1

MULKOM INPUT LISTING FOR EXPERIMENT 5-2
(Temperature-dependent Rock Thermal Conductivity)

```
*** STANFORD COLD SWEEP EXFEFIYENT ***        1.5 HOUR RUN          **.
ROCKS
VOID      2650.      .9999      10.0E-12  1C.CE-12  1C.0E-12     0.00F41000.
ROCK      2623.      .01         1.0E-14   1.0E-14   1.0E-14     0.00      913.
VOIDH     2650.      .6680     100.0E-12 100.CE-12 100.0E-12     0.00E4 1000.
WALL      8121.      .00         0.0E-15   C.CE-15   C.0E-15    42.20      486.
FLNGE     7630.      .00         0.0E-15   0.CE-15   0.0E-15    50.03      500.
AAFE      2700.      .01        10.0E-12  1C.CE-12  1C.0E-12    201.       862.
SURPC     2650.      .00         0.0E-15   C.CE-15   0.0E-15    2.80      10000.
SINK     12650.      .10        10.0E-12  10.CE-12  10.0E-12    0.0       10000.
     1.E-5

START
PARAM
    1 184   800000000000C102      A  1 .35      .05                    .000
                      -1.                    F 115     9.80665
1.          2.          4.          8.          1C.         30.
     1.E-4       1.E-2
                37.70E5  220.3
GENER
RV  1INJ                          14     MASS1   7.E5E-3   67.20E3
0.          300.        600.          900.
1203.       1500.       1800.         24CC.
3030.       3600.       4200.         48CC.
5430.       36000.
          7.89E-3     7.89E-3     7.89E-3     7.89E-3
          7.89E-3     7.89E-3     7.89E-3     7.89E-3
          7.89E-3     7.89E-3     7.89E-3
          7.89E-3     7.89E-3
           172.E3      117.E3      101.E3       96.5E3
           96.5E3       84. 0E3     79. 8E3     75.6E3
           71.4E3      71.4E3      71.4E3      67.2E3
           67.2E3      67. 2E3

ELEME                                                    ***  4  30UT STANA
F 1 1          VOID  .1777E-03
F A 1          QOCK  .1019E-03
F B 1          ROCK  .2548E-03
F C 1          ROCK  .4846E-03
r 1 2          JOID  .1777E-03
F A 2          ROCK  .1019E-03
F B 2          ROCK  .2548E-03
F C 2          RCCK  .4846E-03
r i 3          VOID  .1777E-03
F A 3          ROCK  .1019E-03
F B 3          ROCK  .2548E-03
F C 3          ROCK  .4846E-03
r i 4          VOID  .1777E-03
F t 4          ROCK  .1019E-03
f P 4          ROCK  .2548E-03
F C 4          ROCK  .4846E-03
F 1 7          VOID  .1777E-03
F A 7          ROCK  .1019E-03
F B 7          ROCK  .2548E-03
F C 7          ROCK  .4846E-03
f 1 8          VOID  .1777E-03
F A 8          ROCK  .1019E-03
F B 8          ROCK  .2549E-03
F C 8          ROCK  .4846E-03
F 1 9          VCI0  .1777C-03
f A 9          ROCK  .1019E-03
```

F B 9	ROCK	.2548E-03	F 127	VOID	.1777E-03
F C S	ROCK	.4846E-03	F C27	ROCK	.1019E-03
F 110	VOI 3	.1777E-03	F P27	ROCK	.2548E-03
F A10	POCK	.1019E-03	F C27	ROCK	.4846E-03
F "13	ROCK	.2548E-03	F 128	VOID	.1777E-03
F C10	ROCK	.4846E-03	f A28	ROCK	.1019E-03
F 111	VOID	.1777E-03	F B28	POCK	.2548E-03
F A11	ROCK	.1019E-03	F C28	ROCK	.4846E-03
F B11	SOCK	.2548E-03	F 129	VOTD	.1777E-03
F C11	ROCK	.4846E-03	F A29	ROCK	.1019E-03
F 112	VOID	.1777E-03	i B29	ROCK	.2548E-03
F A12	ROCK	.1019E-03	F C29	ROCK	.4846E-03
F B12	ROCK	.2548E-03	F 130	VOID	.1777E-03
F C12	ROCK	.4846E-03	F A30	ROCK	.1019E-03
F 113	VOID	.1777E-03	F B30	ROCK	.2548E-03
F A13	ROCK	.1019E-03	F C30	ROTK	.4846E-03
F B13	ROCK	.2548E-03	F 131	VOID	.1777E-03
F C13	ROCK	.4846E-03	F 431	ROCK	.1019E-03
F 114	VOID	.1777E-03	F 031	ROCK	.2548E-03
F C14	ROCK	.1019E-03	F t31	ROCK	.4846E-03
F B14	ROCK	.2548E-03	F 132	VOID	.1777E-03
F C14	ROCK	.4846E-03	F A32	RCCK	.1019E-03
F 115	JOID	.1777E-03	F B32	ROCK	.2548E-03
F A15	ROCK	.1019E-03	F '32	ROCK	.4846E-03
F B15	ROCK	.2548E-03	F 133	VOID	.1777E-03
F C15	ROCK	.4846E-03	F E33	ROCK	.1019E-03
F 116	VOID	.1777E-03	F P33	ROCK	.2548E-03
F C16	ROCK	.1019E-03	F t33	ROCK	.4846E-03
F B16	ROCK	.2548E-03	F 134	VOID	.1777E-03
F C16	ROCK	.4846E-03	F a34	ROCK	.1019E-03
F 117	VCI3	.1777E-03	F R34	ROCK	.2548E-03
F 417	ROCK	.1019E-03	F r34	ROCK	.4846E-03
F B17	ROCK	.2548E-03	F 135	VCID	.1777E-03
F C17	ROT.K	.4846E-03	F A35	ROCK	.1319E-03
F 118	VOID	.1777E-03	F B35	ROCK	.2548E-03
F A18	ROCK	.1019E-03	F c35	ROCK	.4846E-03
F B18	ROCK	.2548E-03	F 136	VOID	.1777E-03
f C18	ROCK	.4846E-03	f 436	ROCK	.1019E-03
F 119	VOID	.1777E-03	F R36	ROCK	.2548E-03
F A19	ROCK	.1019E-03	f t36	ROCK	.4846E-03
F C19	ROCK	.2548E-03	F 137	VOID	.1777E-03
F C19	ROCK	.4846E-03	F 637	ROCK	.1019E-03
F 120	VOID	.1777E-03	F e37	ROCK	.2548E-03
F a23	ROCK	.1019E-03	F c37	ROCK	.4846E-03
F R20	ROCK	.2548E-03	F 138	VOID	.1777E-03
F CZO	ROCK	.4846E-03	F A38	ROCK	.1019E-03
F 121	VOID	.1777E-03	F B38	ROCK	.2548E-03
F A21	ROCK	.1019E-03	f C38	ROCK	.4846E-03
F R21	ROCK	.2548E-03	F 139	JOID	.1777E-03
F C21	ROCK	.4846E-03	F 439	ROCK	.1019E-03
F 122	VOID	.1777E-03	F 839	ROCK	.2548E-03
F A22	ROCK	.1019E-03	F C19	ROCK	.4846E-03
F E 22	ROCK	.2548E-03	F 140	VOID	.1777E-03
F C22	ROCK	.4846E-03	f A40	ROCK	.1019E-03
F 123	VOID	.1777E-03	F 840	ROCK	.2548E-03
F 423	ROCK	.1019E-03	F C40	ROCK	.4846E-03
F B23	RCCK	.2548E-03	F 141	VOID	.1777E-03
F C23	ROCK	.4846E-03	F A41	ROCK	.1319f-03
F 124	VOID	.1777E-03	F B41	POCK	.2548E-03
F A24	ROCK	.1019E-03	F t41	ROCK	.4846E-03
F B24	ROCK	.2548E-03	F 142	VOID	.1777E-03
F C24	ROCK	.4846E-03	F C42	ROCK	.1019E-03

r B42	ROCK	.254AT-03	F 163			VCID	.1346[-03
F C42	ROCK	.4846[-03	r A60			ROCK	.7720[-04
r 143	VOID	.1777[-03	r B60			ROCK	.1930[-03
F A43	ROCK	.1019[-03	F C60			ROCK	.3672[-03
r B43	ROCK	.2548[-03	BV 1			VOIDH	5.83[-05
F r43	ROCK	.4846[-03	BV 2			VOIDH	5.71[-05
r 144	VOID	.1777[-03	BV 3			VOIDH	2.21[-04
r A44	ROCK	.1019[-03	BV 4			VOIDH	5.99[-04
r B44	ROCK	.2548[-03	BV 5			VOIDH	8.83E-04
r C44	ROCK	.4846[-03	BV 6			VOIDH	1.07[-03
F 145	VOID	.1777[-03	BF 1			BAFF	9.98[-04
r A45	ROCK	.1019[-03	BW 1			WALL	3.28[-05
F P45	RCCK	.2548[-03	BW 2			WALL	1.25[-04
F t45	ROCK	.4846[-03	BW 3			WALL	2.52[-04
F 146	VOID	.1777[-03	BW 4			WALL	2.11E-04
r A46	ROCK	.1019[-03	BW 5			WALL	1.81[-04
F B46	ROCK	.2548[-03	BW 6			WALL	1.61[-04
r C46	ROCK	.4846[-03	BW 7			WALL	1.51[-04
F 147	VOID	.1777[-03	WAL 1	1	1	WALL	1.22[-04
F C47	ROCK	.1019[-03	WAL 3	9	1	FLNGE	0.83[-03
F 847	RGCK	.2548[-03	WAL 13	37	1	WALL	1.26[-04
r C47	ROCK	.4846[-03	WAL 51	5	1	WALL	0.98[-04
r 148	VOID	.1777[-03	WAL 57	3	1	FLNGE	0.74[-03
F A48	ROCK	.1019[-03	BS			SURRO	1.000E50
F B48	RCCK	.2548[-03	TV			VOID	4.11[-04
F r45	ROCK	.4846[-03	TW			WALL	1.24[-03
r 149	VOID	.1777[-03	TS			SURRO	1.000E50
r A49	POCK	.1019[-03	DIS			SINK	1.000E50
r B49	ROCK	.2548[-03	SUR 1	59	1	SURRO	1.000E50
r C49	ROCK	.4846[-03	F 1 5			VOID	.1777[-03
r 150	VOID	.1777[-03	F A 5			ROCK	.1019[-03
F A50	ROCK	.1019[-03	r B 5			ROCK	.1019[-03
F B50	ROCK	.2548[-03	F C 5			ROCK	.1019E-03
r C50	ROCK	.4846[-03	r D 5			ROCK	.1019C-03
F 151	VOID	.1346E-03	F E 5			ROCK	.1019E-03
r A51	ROCK	.7720[-04	r F 5			ROCK	.1019[-03
F B51	ROCK	.1930[-03	F G 5			ROCK	.1019C-03
r C51	ROCK	.3672E-03	F H 5			ROCK	.7704[-04
r 152	VOID	.1346[-03	r I 5			ROCK	.3057E-04
F 452	ROCK	.7720[-04	F J 5			RCCK	.2038E-04
F B52	POCK	.1930[-03	r i b			VOID	.1777E-03
r C52	ROCK	.3672[-03	F 2 6			ROCK	.1019E-03
F 153	VOID	.1346[-03	F R 6			ROCK	.1019E-03
F 453	ROCK	.7720F-04	F C 6			ROCK	.1019[-03
F 053	ROCK	.1930[-03	F D 6			ROCK	.1019E-03
r C53	ROCK	.3672[-03	f C 6			ROCK	.1019[-03
r i54	VOID	.1346E-03	F F 6			ROCK	.1019C-03
F 454	POCK	.7720[-04	r G 6			ROCK	.1019[-03
r B54	ROCK	.1930[-03	r H 6			ROCK	.7704[-04
r C54	ROCK	.3672[-03	F I 6			ROCK	.3057[-04
r 157	VOID	.1346[-03	r J 6			ROCK	.2038[-04
r A57	ROCK	.7720[-04	r 125			VOID	.1777[-03
F B57	ROCK	.1930[-03	r A25			ROCK	.1019[-03
r C57	ROCK	.3672[-03	F P25			RCCK	.1019[-03
F 158	VOID	.1346[-03	F t25			POCK	.1019[-03
r A58	ROCK	.7720[-04	F C25			ROCK	.1019[-03
r P58	RGCK	.1930[-03	F C25			ROCK	.1019F-03
r C58	ROCK	.3672C-03	F F25			ROCK	.1019[-03
F 159	VOID	.1346[-03	F G25			ROCK	a1019[-03
F C59	POCK	.7720[-04	r H25			ROCK	.7704[-04
F B59	ROCK	.1930[-03	F I25			ROCK	.3057E-04
r C59	ROCK	.3672[-03	r J25			ROCK	.2038[-04

```
F 126          VOID  .1777E-03
F A26          ROCK  .1019E-03
F B26          ROCK  .1019E-03
F C26          ROCK  .1019E-03
F D26          ROCK  .1019E-03
F E26          ROCK  .1019E-03
F F26          ROCK  .1019E-03
F G26          ROCK  .1019E-03
F H26          ROCK  .7704E-04
F I26          ROCK  .3057E-04
F J26          ROCK  .2039E-04
F 155          VOID  .1346E-03
F A55          ROCK  .7720E-04
F P55          ROCK  .7720E-04
F C55          ROCK  .7720E-04
F D55          ROCK  .7720E-04
F E55          ROCK  .7720E-04
F F55          ROCK  .7720E-04
F t55          ROCK  .7720E-04
F H55          ROCK  .5836E-04
F 155          ROCK  .2316E-04
F J55          ROCK  .1544E-04
F 156          VOID  .1346E-03
F A56          ROCK  .7720E-04
F B56          ROCK  .7720E-04
F C56          ROCK  .7720E-04
f D56          ROCK  .7720E-04
F E56          ROCK  .7720E-04
F T56          ROCK  .7720E-04
F G56          ROCK  .7720E-04
F H56          ROCK  .5836E-04
F 156          ROCK  .2316E-04
F J56          ROCK  .1544E-04

CONNE
F 1 1F 1 2     1 .1340E-01 .1340E-01 .3802E-01-.0
F 1 2F 1 3     1 .1340E-01 .1340E-01 .3802E-01-.0
F 1 3F 1 4     1 .1340E-01 .1340E-01 .3802E-01-.0
F 1 4F 1 5     1 .1340E-01 .1340E-01 .3802E-01-.0
F 1 5F 1 6     1 .1340E-01 .1340E-01 .3802E-01-.0
F 1 6F 1 7     1 .1340E-01 .1340E-01 .3802E-01-.0
F 1 7F 1 8     1 .1340E-01 .1340E-01 .3802E-01-.0
F 1 8F 1 9     1 .1340E-01 .1340E-01 .3802E-01-.0
F 1 9F 110     1 .1340E-01 .1340E-01 .3802E-01-.0
F 110F 111     1 .1340E-01 .1340E-01 .3802E-01-.0
F 111F 112     1 .1340E-01 .1340E-01 .3802E-01-.0
F 112F 113     1 .1340E-01 .1340E-01 .3802E-01-.0
F 113F 114     1 .1340E-01 .1340E-01 .3802E-01-.0
F 114F 115     1 .1340E-01 .1340E-01 .3802E-01-.0
F 115F 116     1 .1340E-01 .1340E-01 .3802E-01-.0
F 116F 117     1 .1340E-01 .1340E-01 .3802E-01-.0
F 117F 118     1 .1340E-01 .1340E-01 .3802E-01-.0
F 118F 119     1 .1340E-01 .1340E-01 .3802E-01-.0
F 119F 120     1 .1340E-01 .1340E-01 .3802E-01-.0
F 120F 121     1 .1340E-01 .1340E-01 .3802E-01-.0
F 121F 122     1 .1340E-01 .1340E-01 .3802E-01-.0
F 122F 123     1 .1340E-01 .1340E-01 .3802E-01-.0
F 123F 124     1 .1340E-01 .1340E-01 .3802E-01-.0
F 124F 125     1 .1340E-01 .1340E-01 .3802E-01-.0
F 125F 126     1 .1340E-01 .1340E-01 .3802E-01-.0
F 126F 127     1 .1340E-01 .1340E-01 .3802E-01-.0
F 127F 128     1 .1340E-01 .1340E-01 .3802E-01-.0
```

```
F 128F 129          1 .1340E-01 .1340E-01 .3802E-01-.0
F 129F 130          1 .1340E-01 .1340E-01 .3802E-01-.0
F 130F 131          1 .1340E-01 .1340E-01 .3802E-01-.0
F 131F 132          1 .1340E-01 .1340E-01 .3802E-01-.0
F 132F 133          1 .1340E-01 .1340E-01 .3802E-01-.0
F 133F 134          1 .1340E-01 .1340E-01 .3802E-01-.0
F 134F 135          1 .1340E-01 .1340E-01 .3802E-01-.0
F 135F 136          1 .1340E-01 .1340E-01 .3802E-01-.0
F 136F 137          1 .1340E-01 .1340E-01 .3802E-01-.0
F 137F 138          1 .1340E-01 .1340E-01 .3802E-01-.0
F 138F 139          1 .1340E-01 .1340E-01 .3802E-01-.0
F 139F 140          1 .1340E-01 .1340E-01 .3802E-01-.0
F 140F 141          1 .1340E-01 .1340E-01 .3802E-01-.0
F 141F 142          1 .1340E-01 .1340E-01 .3802E-01-.0
F 142F 143          1 .1340E-01 .1340E-01 .3802E-01-.0
F 143F 144          1 .1340E-01 .1340E-01 .3802E-01-.0
F 144F 145          1 .1340E-01 .1340E-01 .3802E-01-.0
F 145F 146          1 .1340E-01 .1340E-01 .3802E-01-.0
F 146F 147          1 .1340E-01 .1340E-01 .3802E-01-.0
F 147F 148          1 .1340E-01 .1340E-01 .3802E-01-.0
F 148F 149          1 .1340E-01 .1340E-01 .3802E-01-.0
F 149F 150          1 .1340E-01 .1340E-01 .3802E-01-.0
F 150F 151          1 .1340E-01 .1016E-01 .3802E-01-.0
F 151F 152          1 .1016E-01 .1016E-01 .3802E-01-.0
F 152F 153          1 .1016E-01 .1016E-01 .3802E-01-.0
F 153F 154          1 .1016E-01 .1016E-01 .3802E-01-.0
F 154F 155          1 .1016E-01 .1016E-01 .3802E-01-.0
F 155F 156          1 .1016E-01 .1016E-01 .3802E-01-.0
F 156F 157          1 .1016E-01 .1016E-01 .3802E-01-.0
F 157F 158          1 .1016E-01 .1016E-01 .3802E-01-.0
F 158F 159          1 .1016E-01 .1016E-01 .3802E-01-.0
F 159F 160          1 .1016E-01 .1016E-01 .3802E-01-.0
F 1 1F A 1          10.         .1910E-02 .2784E-01
F A 1F B 1          1 .1910E-02 .5721E-02 .2552E-01
F B 1F C 1          1 .5721E-02 .1607E-01 .1916E-01
F 1 2F A 2          10.         .1910E-02 .2784E-01
F A 2F B 2          1 .1910E-02 .5721E-02 .2552E-01
F B 2F C 2          1 .5721E-02 .1607E-01 .1916E-01
F 1 3F A 3          10.         .1910E-02 .2784E-01
F A 3F B 3          1 .1910E-02 .5721E-02 .2552E-01
F B 3F C 3          1 .5721E-02 .1607E-01 .1916E-01
F 1 4F A 4          10.         .1910E-02 .2784E-01
F A 4F B 4          1 .1910E-02 .5721E-02 .2552E-01
F B 4F C 4          1 .5721E-02 .1607E-01 .1916E-01
F 1 7F A 7          10.         .1910E-02 .2784E-01
F A 7F B 7          1 .1910E-02 .5721E-02 .2552E-01
F B 7F C 7          1 .5721E-02 .1607E-01 .1916E-01
F 1 8F A 8          10.         .1910E-02 .2784E-01
F A 8F B 8          1 .1910E-02 .5721E-02 .2552E-01
F B 8F C 8          1 .5721E-02 .1607E-01 .1916E-01
F 1 9F A 9          10.         .1910E-02 .2784E-01
F A 9F B 9          1 .1910E-02 .5721E-02 .2552E-01
F B 9F C 9          1 .5721E-02 .1607E-01 .1916E-01
F 110F A10          10.         .1910E-02 .2784E-01
F C10F B10          1 .1910E-02 .5721E-02 .2552E-01
F B10F C10          1 .5721E-02 .1607E-01 .1916E-01
F 111F A11          10.         .1910E-02 .2784E-01
F A11F B11          1 .1910E-02 .5721E-02 .2552E-01
F B11F C11          1 .5721E-02 .1607E-01 .1916E-01
F 112F A12          10.         .1910E-02 .2784E-01
F A12F B12          1 .1910E-02 .5721E-02 .2552E-01
F B12F C12          1 .5721E-02 .1607E-01 .1916E-01
```

F 113F A13	10.	.1910E-02	.2784E-01	
F A13F B13	1 .1910E-02	.5721E-02	.2552E-01	
F B13F C13	1 .5721E-02	.1607E-01	.1916E-01	
F 114F A14	10.	.1910E-02	.2784E-01	
F A14F B14	1 .1910E-02	.5721E-02	.2552E-01	
F B14F C14	1 .5721E-02	.1607E-01	.1916E-01	
F 115F A15	10.	.1910E-02	.2784E-01	
F A15F R15	1 .1910E-02	.5721E-02	.2552E-01	
F B15F C15	1 .5721E-02	.1607E-01	.1916E-01	
F 116F A16	10.	.1910E-02	.2784E-01	
F A16F B16	1 .1910E-02	.5721E-02	.2552E-01	
F B16F C16	1 .5721E-02	.1607E-01	.1916E-01	
F 117F A17	10.	.1910E-02	.2784E-01	
F A17F B17	1 .1910E-02	.5721E-02	.2552E-01	
F B17F C17	1 .5721E-02	.1607E-01	.1916E-01	
F 118F Ala-	10.	.1910E-02	.2784E-01	
F A18F B18	1 .1910E-02	.5721E-02	.2552E-01	
F B18F C18	1 .5721E-02	.1607E-01	.1916E-01	
F 119F A19	10.	.1910E-02	.2784E-01	
F A19F B19	1 .1910E-02	.5721E-02	.2552E-01	
F B19F C19	1 .5721E-02	.1607E-01	.1916E-01	
F 120F A20	10.	.1910E-02	.2784E-01	
F A20F B20	1 .1910E-02	.5721E-02	.2552E-01	
F B20F C20	1 .5721E-02	.1607E-01	.1916E-01	
F 121F A21	10.	.1910E-02	.2784E-01	
F A21F B21	1 .1910E-02	.5721E-02	.2552E-01	
F B21F C21	1 .5721E-02	.1607E-01	.1916E-01	
F 122F A22	10.	.1910E-02	.2784E-01	
F A22F B22	1 .1910E-02	.5721E-02	.2552E-01	
F B22F C22	1 .5721E-02	.1607E-01	.1916E-01	
F 123F A23	10.	.1910E-02	.2784E-01	
F A23F B23	1 .1910E-02	05721E-02	.2552E-01	
F B23F C23	1 .5721E-02	.1607E-01	.1916E-01	
F 124F A24	10.	.1910E-02	.2784E-01	
F A24F 024	1 .1910E-02	.5721E-02	.2552E-01	
F B24F tZ4	1 .5721E-02	.1607E-01	.1916E-01	
F 127F A27	10.	.1910E-02	.2784E-01	
F A27F B27	1 .1910E-02	05721E-02	.2552E-01	
F B27F C27	1 .5721E-02	.1607E-01	.1916E-01	
F 128F A28	10.	.1910E-02	.2784E-01	
F A28F B28	1 .1910E-02	.5721E-02	.2552E-01	
F B28F C28	1 .5721E-02	.1607E-01	.1916E-01	
F 129F A?S	10.	.1910E-02	.2784E-01	
F A29F B29	1 .1910E-02	.5721E-02	.2552E-01	
F B29F C29	1 .5721E-02	.1607E-01	.1916E-01	
F 130F A30	10.	.1910E-02	.2784E-01	
F A30F B30	1 .1910E-02	.5721E-02	.2552E-01	
F B30F C30	1 .5721E-02	.1607E-01	.1916E-01	
F 131F A31	10.	.1910E-02	.2784E-01	
F A31F B31	1 .1910E-02	.5721E-02	.2552E-01	
F B31F C31	1 .5721E-02	.1607E-01	.1916E-01	
F 132F A32	10.	.1910E-02	.2784E-01	
F A32F B32	1 .1910E-02	.5721E-02	.2552E-01	
F B32F C32	1 .5721E-02	.1607E-01	.1916E-01	
F 133F A33	10.	.1910E-02	.2784E-01	
F A33F 833	1 .1910E-02	.5721E-02	.2552E-01	
F B33F C33	1 .5721E-02	.1607E-01	.1916E-01	
F 134F A34	13.	.1910E-02	.2784E-01	
F A34F B34	1 .1910E-02	.5721E-02	.2552E-01	
F B34F C34	1 .5721E-02	.1607E-01	.1916E-01	
F 135F A35	10.	.1910E-02	.2784E-01	
F A35F P35	1 .1910E-02	.5721E-02	.2552E-01	

F B35F C35	1.5721E-02	.1607E-01	.1916E-01
F 136F 436	10.	.1910E-02	.2784E-01
F A36F R36	1.1910E-02	.5721E-02	.2552E-01
F B36F C36	1.5721E-02	.1607E-01	.1916E-01
F 137F A37	10.	.1910E-02	.2784E-01
F A37F B37	1.1910E-02	.5721E-02	.2552E-01
F B37F C37	1.5721E-02	.1607E-01	.1916E-01
F 138F A38	13.	.1910E-02	.2784E-01
F A38F B38	1.1910E-02	.5721E-02	.2552E-01
F B38F C38	1.5721E-02	.1607E-01	.1916E-01
F 139F A39	10.	.1910E-02	.2784E-01
F A39F B39	1.1910E-02	.5721E-02	.2552E-01
F B39F C39	1.5721E-02	.1607E-01	.1916E-01
F 140F A40	10.	.1910E-02	.2784E-01
F 440F P43	1.1910E-02	.5721E-02	.2552E-01
F B40F C40	1.5721E-02	.1607E-01	.1916E-01
F 141F A41	10.	.1910E-02	.2784E-01
F 441F P41	1.1910E-02	.5721E-02	.2552E-01
F B41F t41	1.5721E-02	.1607E-01	.1916E-01
F 142F A42	13.	.1910E-02	.2784E-01
F A42F B42	1.1910E-02	.5721E-02	.2552E-01
F B42F C42	1.5721E-02	.1607E-01	.1916E-01
F 143F A43	10.	.1910E-02	.2784E-01
F A43F B43	1.1910E-02	.5721E-02	.2552E-01
F B43F r43	1.5721E-02	.1607E-01	.1916E-01
F 144F A44	10.	.1910E-02	.2784E-01
f A44F B44	1.1910E-02	.5721E-02	.2552E-01
F B44F r44	1.5721E-02	.1607E-01	.1916E-01
F 145F A45	10.	.1910E-02	.2784E-01
F A45F R45	1.1910E-02	.5721E-02	.2552E-01
F B45F f45	1.5721E-02	.1607E-01	.1916E-01
F 146F A46	10.	.1910E-02	.2784E-01
F A46F B46	1.1910E-02	.5721E-02	.2552E-01
F B46F r46	1.5721E-02	.1607E-01	.1916E-01
F 147F A47	10.	.1910E-02	.2784E-01
F A47F 847	1.1910E-02	.5721E-02	.2552E-01
F B47F C47	1.5721E-02	.1607E-01	.1916E-01
F 148F A48	10.	.1910E-02	.2784E-01
F A48F B48	1.1910E-02	.5721E-02	.2552E-01
F B48F C48	1.5721E-02	.1607E-01	.1916E-01
F 149F A49	10.	.1910E-02	.2784E-01
F A49F B49	1.1910E-02	.5721E-02	.2552E-01
F B49F r49	1.5721E-02	.1607E-01	.1916E-01
F 150F A50	10.	.1910E-02	.2784E-01
F A50F B50	1.1910E-02	.5721E-02	.2552E-01
F B50F C50	1.5721E-02	.1607E-01	.1916E-01
F 151F A51	10.	.1910E-02	.2109E-01
F A51F P51	1.1910E-02	.5721E-02	.1933E-01
F B51F C51	1.5721E-02	.1607E-01	.1451E-01
F 152F 452	13.	.1910E-02	.2109E-01
F A52F B52	1.1910E-02	.5721E-02	.1933E-01
F B52F C52	1.5721E-02	.1607E-01	.1451E-01
F 153F A53	10.	.1910E-02	.2109E-01
F A53F B53	1.1910E-02	.5721E-02	.1933E-01
F B53F C53	1.5721E-02	.1607E-01	.1451E-01
F 154F A54	10.	.1910E-02	.2109E-01
F A54F R54	1.1910E-02	.5721E-02	.1933E-01
F B54F C54	1.5721E-02	.1607E-01	.1451E-01
F 157F A57	10.	.1910E-02	.2109E-01
F A57F B57	1.1910E-02	.5721E-02	.1933E-01
F B57F C57	1.5721E-02	.1607E-01	.1451E-01
F 158F A58	10.	.1910E-02	.2109E-01

F A58F B58	1	.1910E-02	.5721E-02	.1933E-01
F B58F C58	1	.5721E-02	.1607E-01	.1451E-01
F 159F A59	10.		.1910E-02	.2109E-01
F A59F R59	1	.1910E-02	.5721E-02	.1933E-01
F B59F C59	1	.5721E-02	.1607E-01	.1451E-01
F 160F A60	13.		.1910E-02	.2109E-01
F 460F R60	1	.1910E-02	.5721E-02	.1933E-01
F B60F C60	1	.5721E-02	.1607E-01	.1451E-01
F 1 5F A 5	10.		.1927E-02	.2759E-01
F A 5F B 5	1	.1927E-02	.2116E-02	.2530E-01
F B 5F C 5	1	.2116E-02	.2358E-02	.2289E-01
F C 5F D 5	1	.2358E-02	.2687E-02	.2034E-01
F D 5F E 5	1	.2687E-02	.3162E-02	.1762E-01
F E 5F F 5	1	.3162E-02	.3934E-02	.1465E-01
F F 5F G 5	1	.3934E-02	.5495E-02	.1132E-01
F G 5F H 5	1	.5495E-02	.7421E-02	.7351E-02
F H 5F I 5	1	.7421E-02	.5781E-02	.3434E-02
F I 5F J 5	1	.5781E-02	.5121E-02	.1920E-02
F 1 6F A 6	10.		.1927E-02	.2759E-01
F A 6F B 6	1	.1927E-02	.2116E-02	.2530E-01
F B 6F C 6	1	.2116E-02	.2358E-02	.2289E-01
F C 6F D 6	1	.2358E-02	.2687E-02	.2034E-01
F D 6F E 6	1	.2687E-02	.3162E-02	.1762E-01
F E 6F F 6	1	.3162E-02	.3934E-02	.1465E-01
F F 6F G 6	1	.3934E-02	.5495E-02	.1132E-01
F G 6F H 6	1	.5495E-02	.7421E-02	.7351E-02
F H 6F I 6	1	.7421E-02	.5781E-02	.3434E-02
F I 6F J 6	1	.5781E-02	.5121E-02	.1920E-02
F 125F 425	10.		.1927E-02	.2759E-01
F A25F P25	1	.1927E-02	.2116E-02	.2530E-01
F B25F C25	1	.2116E-02	.2358E-02	.2289E-01
F C25F D25	1	.2358E-02	.2687E-02	.2034E-01
F D25F E25	1	.2687E-02	.3162E-02	.1762E-01
F E25F F25	1	.3162E-02	.3934E-02	.1465E-01
F F25F G25	1	.3934E-02	.5495E-02	.1132E-01
F G25F H25	1	.5495E-02	.7421E-02	.7351E-02
F H25F 125	1	.7421E-02	.5781E-02	.3434E-02
F I25F J25	1	.5781E-02	.5121E-02	.1920E-02
F 126F A26	10.		.1927E-02	.2759E-01
F A26F B26	1	.1927E-02	.2116E-02	.2530E-01
F B26F C26	1	.2116E-02	.2358E-02	.2289E-01
F C26F D26	1	.2358E-02	.2687E-02	.2034E-01
F D26F E26	1	.2687E-02	.3162E-02	.1762E-01
F E2CF F26	1	.3162E-02	.3934E-02	.1465E-01
F F26F G26	1	.3934E-02	.5495E-02	.1132E-01
F G26F H26	1	.5495E-02	.7421E-02	.7351E-02
F H26F I26	1	.7421E-02	.5781E-02	.3434E-02
F I26F J26	1	.5781E-02	.5121E-02	.1920E-02
F 155F 455	10.		.1808E-02	.2230E-01
F A55F B55	1	.1808E-02	.1987E-02	.2042E-01
F B55F r55	1	.1987E-02	.2219E-02	.1845E-01
F C55F D55	1	.2219E-02	.2532E-02	.1637E-01
F D55F E55	1	.2532E-02	.2986E-02	.1415E-01
F E55F F55	1	.2986E-02	.3722E-02	.1174E-01
F F55F G55	1	.3722E-02	.5201E-02	.9059E-02
F G55F H55	1	.5201E-02	.6886E-02	.5900E-02
F H55F I55	1	.6886E-02	.5617E-02	.2777E-02
F I55F J55	1	.5617E-02	.5940E-02	.1472E-02
F 156F A56	10.		.1808E-02	.2230E-01
F A56F B5(	1	.1808E-02	.1987E-02	.2042E-01
F B56F C5(	1	.1987E-02	.2219E-02	.1845E-01
F C56F D5(	1	.2219E-02	.2532E-02	.1637E-01

F	D56F	E56				1	.2532E-02	.2986E-02	.1415E-01
F	E56F	F56				1	.2986E-02	.3722E-02	.1174E-01
F	F56F	G56				1	.3722E-02	.5201E-02	.9059E-02
F	G56F	H56				1	.5201E-02	.6886E-02	.5900E-02
F	H56F	I56				1	.6886E-02	.5617E-02	.2777E-02
F	I56F	J56				1	.5617E-02	.5940E-02	.1472E-02
BV	1BV	2				1	1.13E-1	1.13E-1	2.53E-4
BV	1BW	1				1	0.	3.18E-3	4.59E-3
BV	2BV	3				1	1.13E-1	1.56E-2	2.53E-4
BV	2BW	2				1	0.	3.18E-3	4.50E-3
BV	3BV	4				1	1.56E-2	1.56E-2	1.37E-2
BV	3BW	3				1	0.	9.53E-3	2.95E-3
BV	4BV	5				1	1.56E-2	1.56E-2	2.43E-2
BV	4BW	4				1	0.	9.53E-3	5.38E-3
BV	5BV	6				1	1.56E-2	1.56E-2	3.19E-2
BV	5BW	5				1	0.	9.53E-3	6.56E-3
BV	6BF	1				1	1.56E-2	1.27E-2	3.80E-2
BV	6BW	6				1	0.	9.53E-3	7.23E-3
BF	1F 1	1				1	1.27E-2	2.68E-2	3.65E-2
BF	1BW	7				1	1.56E-1	9.53E-3	6.21E-3
BW	1BS					1	3.18E-3	1.C	5.74E-3
BW	2BS					1	3.10E-3	1.C	5.00E-3
BW	3BS					1	9.53E-3	1.C	3.98E-3
BW	4BS					I	9.53E-3	1.C	6.27E-3
BW	5BS					1	9.52E-3	1.C	7.20E-3
BW	6BS					1	9.53E-3	1.C	7.76E-3
BW	7BS					1	9.53E-3	1.C	e.02E-3
BW	1BW	2				1	1.13E-1	1.13E-1	5.00E-4
BW	2BW	3				1	1.13E-1	1.56E-2	6.58E-3
BW	3BW	4				I	1.56E-2	1.56E-2	7.38E-3
BW	4BW	5				1	1.56E-2	1.56E-2	6.25E-3
BW	5BW	6				1	1.56E-2	1.56E-2	5.44E-3
BW	6BW	7				1	1.56E-2	1.56E-2	4.96E-3
BW	7WAL	1				1	1.56E-2	1.27E-2	4.80E-3
WAL	1WAL	2				1	1.27E-2	1.27E-2	4.80E-3
WAL	2WAL	3				1	1.27E-2	1.25E-2	4.80E-3
d4L	3WAL	4	3	1	1	I	1.25E-2	1.25E-2	3.30E-3
d4L	7WAL	8				1	1.25E-2	1.25E-2	2.85E-3
WAL	8WAL	9	3	1	1	1	1.25E-2	1.25E-2	3.30E-3
U4L	12WAL	13				1	1.25E-2	1.34E-2	4.80E-3
WAL	13WAL	14	36	1	I	1	1.34E-2	1.34E-2	4.80E-3
WAL	50WAL	51				1	1.34E-2	1.C4E-2	4.80E-3
WAL	51WAL	52	6	1	1	1	1.04E-2	1.04E-2	5.50E-3
WAL	58WAL	59	1	1	1	1	1.04E-2	1.C4E-2	3.10E-2
WAL	60TW					1	7.05E-3	7.83E-2	2.00E-2
WAL	1SUR	1	1	1	1	1	9.53E-3	1.C	6.59E-3
WAL	3SUR	3	9	1	1	1	5.70E-2	1.C	6.38E-3
WAL	13SUR	13	37	1	1	1	9.53E-3	1.	6.59E-3
WAL	51SUR	51	5	1	1	I	9.53E-3	1.	5.25E-3
WAL	57SUR	57	3	1	1	1	5.73E-2	1.0	e.38E-3
F	1 1WAL	I	1	I	1	1	0	9.53E-3	6.21E-3
F	1 3WAL	3	9	1	1	1	0.	5.70E-2	6.21E-3
F	113WAL	13	37	1	1	1	a.	9.53E-3	6.55E-3
F	151WAL	51	5	1	1	1	0.	9.53E-3	5.06E-3
F	157WAL	57	3	1	1	1	0.	5.70E-2	5.06E-3
F	160TV					1	1.02E-2	9.23E-3	3.66E-2
TV	TW					1	9.23E-3	7.83E-2	3.82E-2
TW	TS					1	7.83E-2	1.C	2.72E-2
TV	DIS					1	9.23E-3	C.	1.00E-4

INCON
RS

```
                    1.E5 24.3
SUR 1    59     1
                    1.E5 24.30
TS
                    1.E5 24.30
PV  1
                    1.E5 41.

ENDCY
```

Appendix B

ANALYSIS OF THE PHYSICAL MODEL EXPERIMENT 5-2 UNDER SIMULATED ADIABATIC BOUNDARY CONDITION

This appendix presents predicted temperature transients of the physical model by the "calibrated" LBL simulator using an artifically imposed adiabatic system boundary condition on the reservoir conditions similar to experiment 5-2. The primary goal was to investigate the effects of the pressure vessel steel thermal capacitance on the observed rock and water temperatures and on the measured production characteristics. This computer model was considered to be more representative of a scaled field reservoir since the actual reservoir formation energy recharge from its surrounding is an exceedingly slow process which can be effectively modeled as an adiabatic control surfaoe process. This study also serves as an example of demonstrating the advantage of the simulator in complementing the experimental hardware simulation capability.

Figure B-1 shows analysis results for input parameters similar to those used for the run in Figure 5-9. The major difference is in the adiabatic boundary at the pressure vessel boundaries. This boundary condition was numerically created by setting all pertinent structural component thermal conductivities to zero. The apparent result from Figure B-1 is lawer computed rock-center and water temperatures. Comparisons of these results to the data presented in Figure **5-9** show temperature reductions at the end of the run (1.5 hour) as indicated in Table B-1.

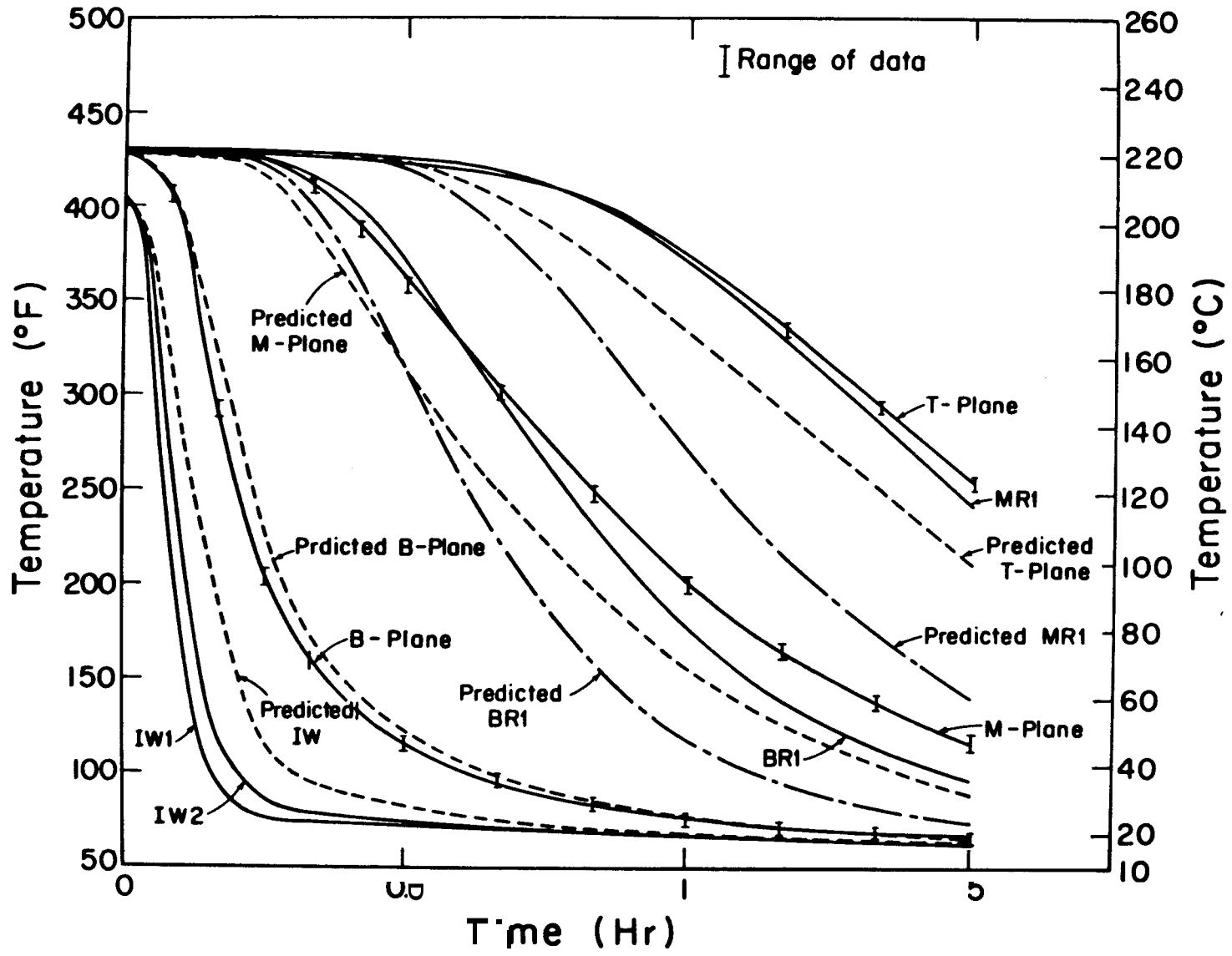

Fig. B-1: Comparison of Measured and Predicted Water and Rock-center Temperatures for Heat Extraction Experiment 5-2 (temperature-dependent rock conductivity and adiabatic boundary condition)

Table B-1

CHANGES IN PREDICTED TEMPERATURES FOR THE ADIABATIC-BOUNDARY-CONDITION RUN

Location	Lower in Predicted Water Temperature (°C)	Lower in Predicted Rock Center Temperature (°C)
B-Plane	*3.6*	*9.9*
M-Plane	*33.8*	*51.3*
T-Plane	*54.0*	*41.3* (not instrumented)
Outlet (T/C#110)	*58.3*	---

It is observed from Figure 6-1 that better model/data agreement is obtained at the B-plane than reported in Figure 5-9, indicating the presence of metal capacitance before did affect calculations at downstream regions: This run also provides a good example of demonstrating the code's capability in generating relatively sharp temperature gradient (e.g., at B-plane shown in Figure B-1). Furthermore, the "heat-transfer limited" nature of fractured reservoir sweep flow is also realized in this prediction.

Close examination of Figures 5-9 and B-1 gives a good estimate of the difference in calculated production energy by the two models based on the assumption of constant water specific heat and recharge rate throughout the 1.5-hour period. The decline in total thermal energy extraction was found to be about 11 percent. This decrease can be attributed to the steel heat source minus the boundary heat loss.

Studying the system temperatures confirms the above predictions and allows an estimate of the fraction of sensible heat stored initially and

finally in the steel. Using 0°C as the reference temperature, the initial steel thermal energy content is approximately equal to *587* MJ as compared to the total system thermal energy content of *1468* MJ. This gives an initial steel energy fraction of *40* percent. Similarly, the thermal energy stored id the rock is found to be approximately *44* percent of the total initial energy.

Estimation of the energy stored in the steel at *1.5* hr gives *28* percent while the energy stored in the rock increases to *58* percent. A simple energy balance can explain the redistribution of energy and show that the steel structures are the principal heat source for the heat loss, while the hot rock is the prime energy source for heating the sweeping water in production experiment 5-2. The predicted production temperature given in Figure B-1 can also be applied to check the energy distributions in more detail. This sample run represents one way the code can assist in understanding the physical model and interpreting experimental data.